The Astrophysical Journal, 754:83 (33pp), 2012 August 1 doi:10.1088/0004-637X/754/2/83

UV-CONTINUUM SLOPES AT $z \sim 4$–7 FROM THE HUDF09+ERS+CANDELS OBSERVATIONS: DISCOVERY OF A WELL-DEFINED UV COLOR–MAGNITUDE RELATIONSHIP FOR $z \geqslant 4$ STAR-FORMING GALAXIES*

R. J. Bouwens[1,2], G. D. Illingworth[2], P.A. Oesch[2,6], M. Franx[1], I. Labbé[1], M. Trenti[3], P. van Dokkum[4], C. M. Carollo[5], V. González[2], R. Smit[1], and D. Magee[2]
[1] Leiden Observatory, Leiden University, NL-2300 RA Leiden, The Netherlands
[2] UCO/Lick Observatory, University of California, Santa Cruz, CA 95064, USA
[3] Center for Astrophysics and Space Astronomy, University of Colorado, 389-UCB, Boulder, CO 80309, USA
[4] Department of Astronomy, Yale University, New Haven, CT 06520, USA
[5] Institute for Astronomy, ETH Zurich, 8092 Zurich, Switzerland
Received 2011 September 9; accepted 2012 May 28; published 2012 July 9

ABSTRACT

Ultra-deep Advanced Camera for Surveys (ACS) and WFC3/IR HUDF+HUDF09 data, along with the wide-area GOODS+ERS+CANDELS data over the CDF-S GOODS field, are used to measure UV colors, expressed as the UV-continuum slope β, of star-forming galaxies over a wide range of luminosity ($0.1L^*_{z=3}$ to $2L^*_{z=3}$) at high redshift ($z \sim 7$ to $z \sim 4$). β is measured using all ACS and WFC3/IR passbands uncontaminated by Lyα and spectral breaks. Extensive tests show that our β measurements are only subject to minimal biases. Using a different selection procedure, Dunlop et al. recently found large biases in their β measurements. To reconcile these different results, we simulated both approaches and found that β measurements for faint sources are subject to large biases if the same passbands are used both to select the sources and to measure β. High-redshift galaxies show a well-defined rest-frame UV color–magnitude (CM) relationship that becomes systematically bluer toward fainter UV luminosities. No evolution is seen in the slope of the UV CM relationship in the first 1.5 Gyr, though there is a small evolution in the zero point to redder colors from $z \sim 7$ to $z \sim 4$. This suggests that galaxies are evolving along a well-defined sequence in the $L_{\rm UV}$–color (β) plane (a "star-forming sequence"?). Dust appears to be the principal factor driving changes in the UV color β with luminosity. These new larger β samples lead to improved dust extinction estimates at $z \sim 4$–7 and confirm that the extinction is essentially zero at low luminosities and high redshifts. Inclusion of the new dust extinction results leads to (1) excellent agreement between the star formation rate (SFR) density at $z \sim 4$–8 and that inferred from the stellar mass density; and (2) to higher specific star formation rates (SSFRs) at $z \gtrsim 4$, suggesting that the SSFR may evolve modestly (by factors of $\sim$2) from $z \sim 4$–7 to $z \sim 2$.

Key words: galaxies: evolution – galaxies: high-redshift

Online-only material: color figures, machine-readable table

1. INTRODUCTION

One of the biggest frontiers in extragalactic cosmology is to characterize the early build-up and evolution of galaxies. It is important for our understanding of early gas accretion and star formation in the universe, estimating the rate of early metal injection into the intergalactic medium (IGM), and assessing the impact of galaxies on reionization. From the observations, we already have a good measure of how fast galaxies build up through Lyman-break selections and luminosity function (LF) studies reaching all the way to $z \sim 8$ (e.g., Bouwens et al. 2010b; McLure et al. 2010; Bunker et al. 2010; Yan et al. 2010). Galaxies show a remarkably uniform brightening in their LFs from $z \sim 8$ to $z \sim 4$ (e.g., Bouwens et al. 2011b) and plausibly from $z \sim 10$ (Bouwens et al. 2011a). There is even some evidence for very rapid evolution at $z \gtrsim 8$ (Bouwens et al. 2011a; Oesch et al. 2012a).

Despite general constraints on how the galaxy population builds up with cosmic time, much less is known about how individual galaxies grow. Qualitatively, we would expect galaxies to build up monotonically in mass, metallicity, and dust content as they form stars. Quantifying how this buildup occurs and with what star formation history is very challenging, however. The effects of dust, metal, and age on the colors are very similar and make it very difficult to disentangle one factor from the others. Nonetheless, there is enough information available, i.e., the UV-to-optical colors (Stark et al. 2009; González et al. 2010; Labbé et al. 2010b), UV colors (e.g., Bouwens et al. 2009; Hathi et al. 2008), and high-resolution spectra of high-redshift galaxies (e.g., Stark et al. 2010; Vanzella et al. 2009), that significant progress should be made in better characterizing galaxies throughout the buildup process.

An important piece of the puzzle in deciphering how galaxies build up is provided by the rest-frame UV spectrum and, in particular, the UV colors. The rest-frame UV color provides us with perhaps our best means for estimating the dust extinction and star formation rate (SFR) for faint $z > 3$ galaxies, given that other techniques for probing the SFR tend to only detect the most bolometrically luminous galaxies (e.g., Bouwens et al. 2009; Smit et al. 2012). The UV colors also show a systematic dependence on the UV luminosities of star-forming galaxies (e.g., Bouwens et al. 2009, 2010a) and are much more amenable to direct measurement than rest-frame UV–optical colors where mid-IR (IRAC) photometry is necessary.

A significant amount of effort has gone into establishing the UV-continuum slope distribution at high redshift $z > 2$ and determining its dependence upon redshift and luminosity. The earliest analyses were at $z \sim 2$–3 using either ground-based observations (Steidel et al. 1999; Adelberger & Steidel 2000)

* Based on observations made with the NASA/ESA *Hubble Space Telescope*, which is operated by the Association of Universities for Research in Astronomy, Inc., under NASA contract NAS 5-26555. These observations are associated with programs 11563 and 9797.
[6] Hubble Fellow.

or the deep WFPC2 observations over the HDF North (Meurer et al. 1999). Subsequent analyses pushed UV-continuum slope measurements to $z \sim 4$–6 using Subaru Suprime-Cam, *Hubble Space Telescope* (*HST*) Advanced Camera for Surveys (ACS), or *HST* NICMOS observations (Ouchi et al. 2004a; Papovich et al. 2004; Stanway et al. 2005; Bouwens et al. 2006; Hathi et al. 2008). Bouwens et al. (2009) extended these previous works by examining the UV slopes as a function of luminosity over the entire redshift range $z \sim 2$–6—establishing a coherent framework for understanding the observational results at that time.

The availability of both deep and wide WFC3/IR imaging has made it possible to substantially improve these early measurements of the UV-continuum slope. These imaging observations allow for accurate measurements of the UV-continuum slopes for large numbers of $z \sim 4$–7 galaxies. Already Bouwens et al. (2010a) made use of the early WFC3/IR observations to determine the UV-continuum slope distribution out to $z \sim 7$ (see also Oesch et al. 2010c; Bouwens et al. 2010b; Bunker et al. 2010; Finkelstein et al. 2010; Robertson et al. 2010; Dunlop et al. 2012; Wilkins et al. 2011). Bouwens et al. (2010a) found that very low luminosity $z \sim 7$–8 galaxies in the ultra-deep HUDF09 WFC3/IR field had UV-continuum slopes β as steep as -2.5 and plausibly consistent with -3, but with uncertainties of $\sim$0.2–0.3. Finkelstein et al. (2010) also reported on the colors of ultrafaint $z \sim 7$–8 galaxies in the HUDF finding similar steep β values, but with somewhat larger uncertainties.

Since the early WFC3/IR campaign over the HUDF (Bouwens et al. 2010b; Oesch et al. 2010c) from the HUDF09 program (GO 11563: PI: Illingworth), the amount of deep, wide-area WFC3/IR observations over well-known legacy fields has increased dramatically. At present, we have ultra-deep WFC3/IR observations over the two HUDF09/HUDF05 fields (Bouwens et al. 2011b; Oesch et al. 2007, 2010c), wide-area ($\sim$145 arcmin^2) data over the CDF-South GOODS field as a result of the Early Release Science (Windhorst et al. 2011) and CANDELS (Grogin et al. 2011; Koekemoer et al. 2011) programs, and even deeper WFC3/IR observations over the HUDF and HUDF05 fields (Bouwens et al. 2011b). These observations greatly improve the luminosity baseline, redshift range, and precision with which we can define the UV-continuum slope distribution for $z \sim 4$–7 galaxies.

In this paper, we take advantage of these new observations to establish the distribution of UV-continuum slopes β over a wide range in luminosity and redshift. These new observations allow us to determine with great precision how the UV-continuum slope β distribution depends upon luminosity, in four distinct redshift intervals. This new information puts us in a position to look for a possible star-forming sequence of galaxies at high redshift and to characterize its evolution with cosmic time. The evolution of such a sequence provides useful information for better understanding early galaxy buildup. For example, the slope of a β–luminosity relationship constrains how the dust and age of the galaxy population vary as a function of luminosity. Scatter in the β–luminosity relationship constrains the overall scatter in the stellar populations or dust extinction of individual galaxies. Finally, evolution in the slope and offset of the relation with cosmic time gives us clues as to possible changes in how galaxies evolve, either in age or dust extinction. Independent analyses of the UV-continuum slope β in $z \sim 5$–7 galaxies are provided by Dunlop et al. (2012) and Wilkins et al. (2011), but both are based on a much smaller, shallower set of observations. A somewhat complementary analysis to the one described here is provided by González et al. (2012) who quantify the changes in UV–optical colors as a function of luminosity and redshift.

We provide a brief overview of the paper here. We begin with a brief summary of the observational data (Section 2). In Section 3, we describe the manner in which we construct our high-redshift samples from the observational data, measure the UV-continuum slope β distribution, correct for measurement and selection biases, and present evidence for well-defined color–magnitude relation for galaxies in the rest-fame UV. In Section 4, we compare the present UV-continuum slope β determinations with previous determinations. In Section 5, we explore the implications of such a color–magnitude relation for galaxy growth—using the UV-continuum slopes β to infer a luminosity-dependent dust correction for galaxies. In Section 6, we use these extinction estimates to rederive the SFR density at $z \gtrsim 4$ and then compare these results with what one infers from the stellar mass density. Finally, in Section 7, we conclude and provide a summary of our primary results. The appendices include a detailed description of many quantitative results and simulations essential for accurate measurements of the UV-continuum slopes.

Throughout this work, we find it convenient to quote results in terms of the luminosity $L^*_{z=3}$ Steidel et al. (1999) derived at $z \sim 3$, i.e., $M_{1700,AB} = -21.07$, for consistency with previous work—though we note that the Steidel et al. (1999) LF results are now updated ($M_{1700,\rm AB} = -20.97 \pm 0.14$; Reddy & Steidel 2009) but still consistent with the previous determination. We present our dust extinction estimates as the ratio of the bolometric luminosity (IR + UV luminosity: $L_{\rm IR} + L_{\rm UV}$) to the UV luminosity ($L_{\rm UV}$), i.e., $L_{\rm IR}/L_{\rm UV} + 1$. We refer to the *HST* F435W, F606W, F775W, F814W, F850LP, F098M, F105W, F125W, and F160W bands as B_{435}, V_{606}, i_{775}, I_{814}, z_{850}, Y_{098}, Y_{105}, J_{125}, and H_{160}, respectively. Where necessary, we assume $\Omega_0 = 0.3$, $\Omega_\Lambda = 0.7$, and $H_0 = 70$ km s^{-1} Mpc^{-1}. We quote all SFRs and stellar masses assuming a Salpeter (1955) initial mass function (IMF). All magnitudes are in the AB system (Oke & Gunn 1983).

2. OBSERVATIONAL DATA

Here, we utilize two primary data sets to examine the UV-continuum slope β distribution of galaxies from $z \sim 7$ to $z \sim 4$: (1) the ultra-deep ACS+WFC3/IR observations over the three HUDF09 fields (Bouwens et al. 2010b; Bouwens et al. 2011b; Oesch et al. 2010c) and (2) the wide-area ACS+WFC3/IR observations taken over the CDF-South GOODS field as a result of Early Release Science and CANDELS programs (Windhorst et al. 2011; Giavalisco et al. 2004; Grogin et al. 2011; Koekemoer et al. 2011). A brief summary of the properties of these observations is provided in Table 1. Figure 1 shows the layout of these observations over the CDF-South GOODS area.

2.1. HUDF09 Observations

The first set of observations we utilize is from the HUDF09 program (GO11563: PI: Illingworth) and involves ultra-deep WFC3/IR observations over three fields that already have ultra-deep ACS observations. These fields include the HUDF (Beckwith et al. 2006) and two HUDF05 flanking fields (Oesch et al. 2007). These observations are primarily of use in establishing the distribution of UV-continuum slopes β for very faint $z \sim 4$–7 galaxies.

Table 1
A Summary of the Observational Data Used to Establish the Distribution of UV-continuum Slopes β from $z \sim 7$ to $z \sim 4$

Passband	Detection[a] Limits (5σ)	PSF FWHM (arcsec)	Areal Coverage (arcmin^2)
	HUDF09 (WFC3/IR HUDF)		
B_{435}	29.7	0.09	4.7
V_{606}	30.1	0.09	4.7
i_{775}	29.9	0.09	4.7
z_{850}	29.4	0.10	4.7
Y_{105}	29.6	0.15	4.7
J_{125}	29.9	0.16	4.7
H_{160}	29.9	0.17	4.7
	HUDF09-1 (WFC3/IR P12)		
V_{606}	29.0	0.09	4.7
i_{775}	29.0	0.09	4.7
z_{850}	29.0	0.10	4.7
Y_{105}	29.0	0.15	4.7
J_{125}	29.3	0.16	4.7
H_{160}	29.1	0.17	4.7
	HUDF09-2 (WFC3/IR P34)		
B_{435}[b]	28.8	0.09	3.3
V_{606}[b]	29.9	0.09	4.7
i_{775}[b]	29.3	0.09	4.7
I_{814}[b]	29.0	0.09	3.3
z_{850}[b]	29.2	0.10	4.7
Y_{105}	29.2	0.15	4.7
J_{125}	29.5	0.16	4.7
H_{160}	29.3	0.17	4.7
	ERS (CDF-S GOODS)		
B_{435}	28.2	0.09	39
V_{606}	28.5	0.09	39
i_{775}	28.0	0.09	39
I_{814}	28.0[c]	0.09	39
z_{850}	28.0	0.10	39
Y_{098}	27.9	0.15	39
J_{125}	28.4	0.16	39
H_{160}	28.1	0.17	39
	CDF-S CANDELS Deep		
B_{435}	28.2	0.09	66
V_{606}	28.5	0.09	66
i_{775}	28.0	0.09	66
I_{814}	28.8	0.09	66
z_{850}	28.0	0.10	66
Y_{105}	28.5	0.16	66
J_{125}	28.8	0.16	66
H_{160}	28.5	0.17	66
	CDF-S CANDELS Wide		
B_{435}	28.2	0.09	40
V_{606}	28.5	0.09	40
i_{775}	28.0	0.09	40
I_{814}	28.1[c]	0.09	40
z_{850}	28.0	0.10	40
Y_{105}	28.0	0.16	40
J_{125}	28.0	0.16	40
H_{160}	27.7	0.17	40

Notes. See Figure 1 for the layout of these data within the CDF-South.
[a] 5σ detection limits for our $z \sim 4$–7 ACS+WFC3/IR selections were measured in a 0.″35 diameter aperture.
[b] Our reductions of the ACS data over the HUDF09-2 field include both those observations taken as part of the HUDF05 (82 orbits) and HUDF09 (111 orbits) programs (see Figure 1 from Bouwens et al. 2011b). The latter observations add ~0.15–0.4 mag to the total optical depths.
[c] The depth of the F814W observations vary considerably over the ERS and CDF-South CANDELS Wide field, from very deep coverage (~28.8 mag) in some regions to essentially no coverage over a small fraction of the area. Typical depths are ~28.0 AB mag (5σ).

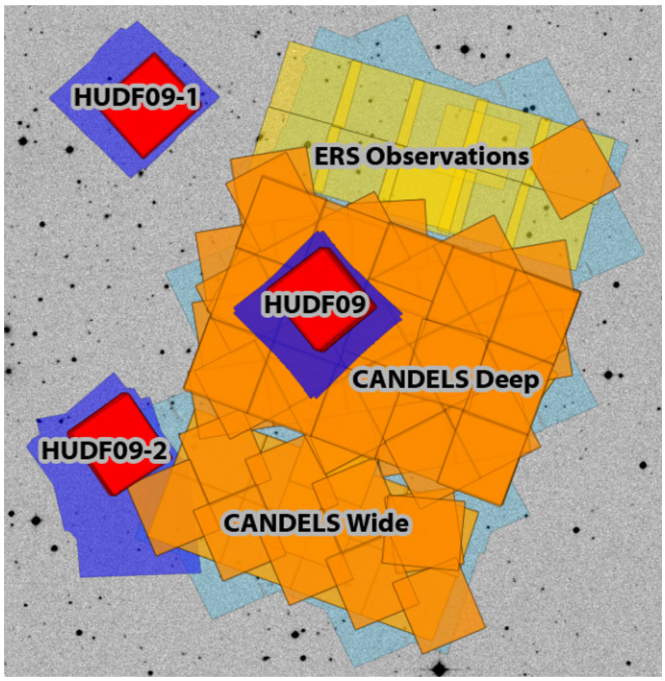

Figure 1. Deep WFC3/IR data over the extended CDF-South GOODS field that can be used to be establish the UV-continuum slope β distribution for star-forming galaxies at $z \geqslant 4$. Ultra-deep WFC3/IR observations are available over the three HUDF09 fields HUDF09, HUDF09-1, and HUDF09-2 (red-shaded regions) while moderately deep WFC3/IR observations are available over the ~145 arcmin^2 ERS (yellow regions) and CANDELS (orange regions) areas. The blue and dark blue regions show the position of the deep GOODS ACS and ultra-deep HUDF+HUDF05 ACS observations, respectively. A convenient summary of the observational properties of each of these fields is provided in Table 1.
(A color version of this figure is available in the online journal.)

At present, the full two years of WFC3/IR observations (all 192 orbits from the GO11563 program) have been obtained over the three HUDF09 fields. The WFC3/IR observations over the HUDF include some 111 orbits of observations—while the HUDF09-1 and HUDF09-2 fields include 33 orbits and 48 orbits of observations, respectively. Our reductions of the WFC3/IR observations over these fields are already described in Bouwens et al. (2011b) and are conducted using standard procedures. Particularly important to this process was ensuring that the geometric distortion and velocity aberration were treated properly so that the registration between bands and with the ACS observations was very accurate ($\lesssim$0.″01). Accurate registration is absolutely essential not only for maximizing the accuracy of our color measurements, but also for minimizing the effect that misregistration might have on scatter in these same color measurements. The depths of our WFC3/IR observations reach to $\gtrsim$29 AB mag at 5σ and are presented in detail in Table 1. The FWHM of the point spread function (PSF) in the WFC3/IR observations is ~0.″16.

Our reductions of the ACS observations over the HUDF09-2 area include all available data—including the 82 orbits that were taken during the execution of the original HUDF05 program and an additional 111 orbits that were taken in parallel with the HUDF09 WFC3/IR observations over the HUDF. The total number of orbits per filter over the HUDF09-2 are 10 orbits F435W, 32 orbits F606W, 46 orbits F775W, 16 orbits F814W, and 89 orbits F850LP. The total integration time is $\gtrsim$50% of that available for the HUDF, allowing us to reach within $\lesssim$0.4 mag of the HUDF. This provides us with sufficiently high

signal-to-noise (S/N) levels required to keep contamination in $z \gtrsim 6$ selections to a minimum. A more detailed description of this data set is provided by Bouwens et al. (2011b).

2.2. ERS/CANDELS Observations

Wide-area WFC3/IR observations allow us to establish the UV-continuum slope β distribution for the rarer, higher luminosity sources. These observations are available over the CDF-South GOODS field from the Early Release Science (Windhorst et al. 2011) and CANDELS (Grogin et al. 2011; Koekemoer et al. 2011) programs.

The WFC3/IR observations from the ERS program are distributed over the northern part of the CDF South GOODS field (Windhorst et al. 2011; Figure 1). These observations consist of 60 orbits of F098M, F125W, and F160W observations distributed over 10 distinct $2\farcm1 \times 2\farcm3$ pointings, with two orbits F098M, two orbits F125W, and two orbits F160W per pointing. The WFC3/IR observations extend over ∼43 arcmin^2 in total, although only ∼39 arcmin^2 of those observations overlap with the ACS GOODS data and can be used here.

WFC3/IR observations from the CANDELS program are distributed over the southern two-thirds of the CDF-South GOODS field (106 arcmin^2), with the deepest section planned for the central ∼66 arcmin^2 portion. Three orbits of F105W, four orbits of F125W, and four orbits of the F160W observations are available over the central sections of the CDF-South (representing all 10 SN search epochs to 2012 February 18) while only one orbit of the F105W, F125W, and F160W observations are available over the southern portion. The layout of the CANDELS and ERS observations with the CDF-South GOODS field is shown in Figure 1.

Our reductions of the WFC3/IR observations over the CDF-South are performed in exactly the same manner as the HUDF09 observations (see Bouwens et al. (2011b) for a detailed description). As in our HUDF09 reductions, a $0\farcm06$ pixel size was used. For the ACS observations over the CDF-South, we used the Bouwens et al. (2007) reductions for the F435W, F606W, F775W, and F850LP bands. These reductions are comparable to the GOODS v2.0 reduction (Giavalisco et al. 2004) but take advantage of the substantial supernova (SN) follow-up observations over the CDF-South (Riess et al. 2007) which add ∼0.1–0.3 mag of depth to the z_{850} band.

We also reduced the new ACS I_{814}-band observations over the CDF-South GOODS fields from the CANDELS+ERS programs to take advantage of the superb depth available with these data at ∼8000 Å (typically 13 orbits over the CANDELS-DEEP region or 0.8 mag deeper than the GOODS i_{775}-band exposures). The F814W observations are valuable for controlling for contamination in our $z \sim 7$ selections and for minimizing the uncertainties in our β determinations at $z \sim 4$. We included all F814W observations from the ERS+CANDELS programs over the CDF-South. After using public codes (e.g., Anderson & Bedin 2010) to correct the raw frames for charge transfer efficiency defects and row-by-row banding artifacts, we performed the alignment, cosmic-ray rejection, and drizzling with the ACS GTO apsis pipeline (Blakeslee et al. 2003).

3. RESULTS

In this section, we describe the procedure we use to establish the distribution of UV-continuum slopes β versus UV luminosity for $z \sim 4$–7 galaxies. We begin with a description of the technique we use for generating the source catalogs needed for sample selection and UV-continuum slope measurements (Section 3.1). We then describe our procedure for selecting our high-redshift samples (Section 3.2) and for deriving the UV-continuum slope β for individual sources (Section 3.3). In Section 3.4, we detail the methods we use to correct the observed distribution of UV-continuum slopes β for selection and measurement biases. In Section 3.5, we combine our UV-continuum slope β determinations in the ultra-deep + wide-area data sets to establish UV-continuum slope β over a wide-range in redshift and luminosity. We then conclude with a discussion of the correlation we find between the UV-slope β and the UV luminosity (Section 3.6).

3.1. Source Catalogs

The procedure for source detection and photometry is discussed in many of our previous papers (e.g., Bouwens et al. 2007); we summarize the key steps here. We generate catalogs for our samples using the SExtractor (Bertin & Arnouts 1996) software run in double image mode, with the detection image taken to be the square root of χ^2 image (Szalay et al. 1999; similar to a co-added image of the WFC3/IR observations) and the measurement image to be a PSF-matched image from our ACS+WFC3/IR image sets (see below).

We select each of our high-redshift samples (i.e., $z \sim 4$, $z \sim 5$, $z \sim 6$, and $z \sim 7$) from separately generated source catalogs. This allows us to take advantage of the fact that $z \sim 4$–6 samples can be selected entirely (or almost entirely) based on the ACS data (involving generally smaller apertures and therefore reducing the uncertainties in our color measurements) while $z \sim 7$ selections require PSF matching to the WFC3/IR data.[7] For our $z \sim 4$–6 catalogs, the first step is to match PSFs by smoothing the shorter wavelength images to the resolution of the ACS z_{850}-band image. The square root of χ^2 images we use for the SExtractor detection images are constructed from the $V_{606}i_{775}z_{850}$, $i_{775}z_{850}$, and z_{850} images for our $z \sim 4$, $z \sim 5$, and $z \sim 6$ selections, respectively. For our $z \sim 7$ catalogs, all the observations are PSF matched to the WFC3/IR H_{160} band. The square root of χ^2 images are constructed from the available WFC3/IR imaging observations, e.g., $Y_{105}J_{125}H_{160}$ for our HUDF09 fields, $Y_{098}J_{125}H_{160}$ images for the ERS observations, and $J_{125}H_{160}$ for the CANDELS observations.

Colors are measured within small scalable apertures using a Kron (1980) factor of 1.2. These small-aperture color measurements are then corrected to total magnitudes in two steps. First, a correction is made for the light in a larger scalable aperture, with Kron factor equal to 2.5. This correction is made from the square root of χ^2 image to optimize the S/N. Second, a correction is made for light outside this large scalable aperture—using the encircled energies measured for point sources (typically a ∼0.1–0.15 mag correction).

Photometry was done using the latest WFC3/IR zero-point calibrations (2012 March 6) which differ by ∼0.01–0.02 mag from the earlier zero points. In addition, a correction to the photometry (i.e., $E(B-V) = 0.009$) was performed to account for foreground dust extinction from our own galaxy. This correction was based on the Schlegel et al. (1998) dust map.

[7] For our $z \sim 6$ selections, we make use of the available WFC3/IR data. In addition to satisfying an $(i_{775} - z_{850})_{AB} > 1.3$ criterion, sources in our $z \sim 6$ selection must also satisfy a $(z_{850} - J_{125}) < 0.9$ color criterion (Section 3.2).

3.2. Sample Selection

To select star-forming galaxies at high redshift, we will use the well-established Lyman-break galaxy (LBG) technique. This technique takes advantage of the unique spectral characteristics of high-redshift star-forming galaxies, which show a very blue spectrum overall but a sharp cutoff blueward of Lyα. It has been shown to be very robust through extensive spectroscopic follow-up (Steidel et al. 1996; Steidel et al. 2003; Bunker et al. 2003; Dow-Hygelund et al. 2007; Popesso et al. 2009; Vanzella et al. 2009; Stark et al. 2010).

We will base our high-redshift samples on selection criteria from previous work on $z \geqslant 4$ galaxies. For our $z \sim 4$ B_{435} and $z \sim 5$ V_{606} dropout samples, we will apply almost the same criteria as Bouwens et al. (2007), namely,

$$(B_{435} - V_{606} > 1.1) \wedge (B_{435} - V_{606} > (V_{606} - z_{850}) + 1.1) \wedge (V_{606} - z_{850} < 1.6)$$

for our B-dropout sample and

$$[(V_{606} - i_{775} > 0.9(i_{775} - z_{850}) + 1.5) \vee (V_{606} - i_{775} > 2))] \wedge (V_{606} - i_{775} > 1.2) \wedge (i_{775} - z_{850} < 0.8)$$

for our V_{606}-dropout selection (but note that we use a $i_{775} - z_{850} < 0.8$ color selection instead of the $i_{775} - z_{850} < 1.2$ selection used by Bouwens et al. 2007 to minimize contamination). For our $z \sim 6$ i_{775}-dropout selection, we expanded the criteria used in Bouwens et al. (2007) to take advantage of the deep near-IR observations from WFC3/IR to set limits on the color redward of the break. Our $z \sim 6$ i_{775}-dropout criterion is

$$(i_{775} - z_{850} > 1.3) \wedge (z_{850} - J_{125} < 0.9).$$

Finally, our $z \sim 7$ z_{850}-dropout criterion is

$$(z_{850} - Y_{105} > 0.7) \wedge (Y_{105} - J_{125} < 0.8) \wedge (z_{850} - Y_{105} > 1.4(Y_{105} - J_{125}) + 0.42),$$

or

$$(z_{850} - J_{125} > 0.9) \wedge (z_{850} - J_{125} > 0.8 + 1.1(J_{125} - H_{160})) \wedge (z_{850} - J_{125} > 0.4 + 1.1(Y_{098} - J_{125})),$$

depending upon whether our search field is from the HUDF09/CANDELS data sets or the ERS data set, respectively. The above selection criteria closely match those used in our previous study of the UV-continuum slope β at $z \sim 7$ (Bouwens et al. 2010a). These criteria are slightly more inclusive than those considered by Bouwens et al. (2011b), but this is to allow us to maximize the size of our samples and to extend our selection to the highest redshift possible without suffering significant contamination from Lyα emission or IGM absorption. In cases of a non-detection in the dropout band, we set the flux in the dropout band to be equal to the 1σ upper limit. To take advantage of the deep I_{814}-band observations over the CDF-South to keep contamination in our $z \sim 7$ samples to a minimum, we required all $z \sim 7$ z_{850}-dropouts in our selection to have $I_{814} - J_{125}$ colors greater than 2.0 or to be undetected in the I_{814} band (at $< 1.5\sigma$). No attempt is made to select or measure UV-continuum slopes for star-forming galaxies at $z \sim 8$ due to the fact that the $J_{125} - H_{160}$ color (the only available color providing high S/N information on the rest-frame UV SED at $z \sim 8$) is affected by Lyman-series absorption and Lyα emission at $z > 8.1$ (but, see Taniguchi et al. 2010).

Figure 2 provides a convenient illustration of the approximate range in UV-continuum slopes β and redshifts selected by the above two-color criteria.

We utilize several additional selection criteria in defining our final samples. Sources are required to have SExtractor stellarity parameters less than 0.8 (i.e., they show evidence of being extended) to ensure our samples are free of contamination from active galactic nuclei (AGNs) or low-mass stars. Given that >97% of bright sources in Lyman-break selections show clear evidence of having extended profiles (i.e., are not pointlike), this criterion has almost no effect on the overall composition of our samples.

We also require that sources be undetected in all bands blueward of the dropout bands. Sources are rejected if they are detected at $>2\sigma$ in a single band, $>1.5\sigma$ in two bands, or have a $\chi^2_{\rm opt} > 3$ in the optical bands. We take $\chi^2_{\rm opt} = \Sigma_i {\rm SGN}(f_i)(f_i/\sigma_i)^2$ where f_i is the flux in band i in our smaller scalable apertures, σ_i is the uncertainty in this flux, and SGN(f_i) is equal to 1 if $f_i > 0$ and -1 if $f_i < 0$ (Bouwens et al. 2011b). As Bouwens et al. (2011b) illustrate, a $\chi^2_{\rm opt}$ criterion can be particularly useful for minimizing contamination in high redshift samples (see also Oesch et al. 2012a, 2012b).

Table 2 summarizes the properties of the $z \sim 4$, $z \sim 5$, $z \sim 6$, and $z \sim 7$ samples we derive from the HUDF09+ERS+CANDELS observations. In total, 308, 137, 70, and 57 $z \sim 4$, $z \sim 5$, $z \sim 6$, and $z \sim 7$ galaxies are found in the HUDF09 fields and 1514, 277, 101, and 44 $z \sim 4$, $z \sim 5$, $z \sim 6$, and $z \sim 7$ galaxies are found in the ERS+CANDELS fields. The approximate redshift distributions for our $z \sim 4$, $z \sim 5$, $z \sim 6$, and $z \sim 7$ selections are shown more explicitly in Figure 3. These redshift distributions are as calculated in Bouwens et al. (2007) and Bouwens et al. (2011b).

Table 2
Lyman-break Samples Used to Measure the Distribution of UV-continuum Slopes β as a Function of Redshift and UV Luminosity

Sample[a]	Field	Luminosity Range[b]	No. of Sources
$z \sim 4$	HUDF09	$-23 < M_{\rm UV,AB} < -16$	308
	ERS/CANDELS	$-23 < M_{\rm UV,AB} < -18$	1524
$z \sim 5$	HUDF09	$-23 < M_{\rm UV,AB} < -17$	137
	ERS/CANDELS	$-23 < M_{\rm UV,AB} < -18.5$	277
$z \sim 6$	HUDF09	$-23 < M_{\rm UV,AB} < -17$	70
	ERS/CANDELS	$-23 < M_{\rm UV,AB} < -19$	101
$z \sim 7$	HUDF09	$-22 < M_{\rm UV,AB} < -17$	57[c,d]
	ERS/CANDELS	$-22 < M_{\rm UV,AB} < -19$	44

Notes.
[a] The mean redshift we estimate for these samples is 3.8, 4.9, 5.9, and 7.0, respectively (Figure 3).
[b] The faint magnitude limit is set by the 5σ depth of the WFC3/IR near-IR observations over our search fields. See Section 3.2.
[c] These samples include sources from the Bouwens et al. (2011b) HUDF09 $z \sim 7$ samples and the lowest redshift galaxies in the Bouwens et al. (2011b) HUDF09 $z \sim 8$ selection.
[d] To keep contamination in our faint $z \sim 7$ selection to a minimum, we only include faint $J_{125,\rm AB} > 28$ sources from the HUDF09 fields with the deepest optical data. We therefore only consider sources from the HUDF (HUDF09) and the $\sim$3 arcmin^2 ($\sim$70%) area in the HUDF09-2 field with deep optical coverage from the HUDF09 program (see Figure 1 from Bouwens et al. 2011b).

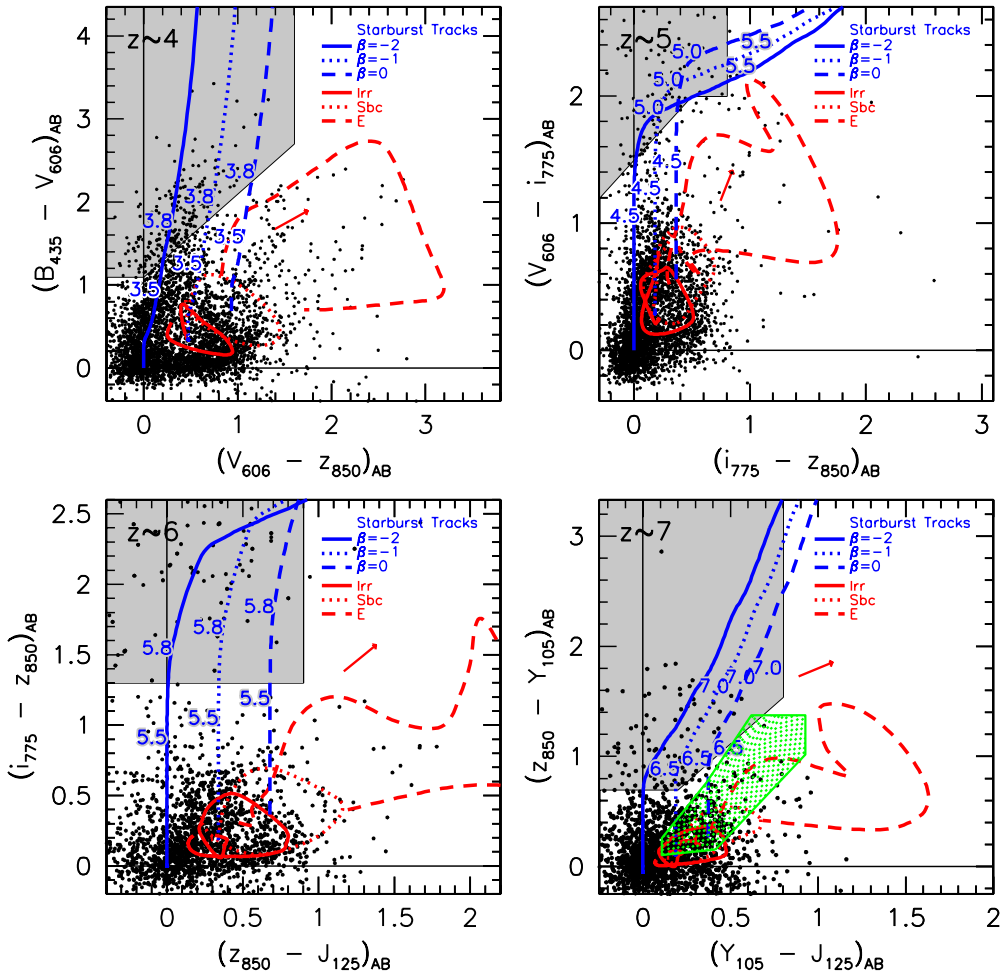

Figure 2. Two-color Lyman-break selection criteria used to select our $z \sim 4$, $z \sim 5$, $z \sim 6$, and $z \sim 7$ galaxy samples. These samples are used to derive the UV-continuum slope β distribution as a function of redshift and luminosity (see Section 3.2). The blue lines show the expected colors vs. redshift for star-forming galaxies with a range of UV-continuum slopes β, while the red lines show the colors expected for low-redshift interlopers. The green hatched region in the $z \sim 7$ panel shows the position of low-mass stars in $z_{850} - Y_{105}/Y_{105} - J_{125}$ space. The black dots show the colors of sources found in our HUDF catalog and provide some indication of the approximation distribution of sources in color–color space. The two-color selection windows we use to identify high-redshift galaxies are indicated in gray. These selection windows allow for the identification of galaxies over a wide range of UV-continuum slopes $\beta \sim -3$ to 0.5. The red arrows show the Calzetti et al. (2000) reddening vectors. In addition to the two color selection criteria shown here, we also utilize a few other criteria in establishing our final samples. For example, we enforce a very stringent optical non-detection criteria, especially for our $z \sim 7$ samples where we require the optical $\chi^2_{\rm opt}$ be below a certain threshold (Section 3.2).
(A color version of this figure is available in the online journal.)

3.3. *Estimating the* UV*-continuum Slope*

Establishing the UV-continuum slope β for a source (where β is defined such that $f_\lambda \propto \lambda^\beta$) requires that we have at least two flux measurements of a source in the UV continuum not significantly affected by Lyα or IGM absorption (unless both the redshift and Lyα flux are already known). In practice, this means that we should not make use of the flux information in the band immediately redward of the break since it is frequently contaminated by Lyα emission or absorption from the IGM. Assuming we have wavelength coverage in the $B_{435}V_{606}i_{775}z_{850}Y_{105}J_{125}H_{160}$ bands, we can obtain good estimates of the UV-continuum slope β for high-redshift sources from $z \sim 4$ to at least $z \sim 7.5$.

There are a few different approaches we could adopt in using the available flux measurements in the UV continuum to estimate these slopes. One approach is to derive the UV-continuum slopes from a fit to all available flux measurements in the rest-frame UV. An alternate approach is to derive a slope from the flux measurements at both ends of a fixed rest-frame wavelength range (e.g., as utilized by Bouwens et al. 2009).

Each approach has its advantages. The first approach uses the full flux information available on each source and also takes advantage of a much more extended wavelength baseline. This results in much smaller uncertainties in our β determinations, particularly at $z \sim 4$ and $z \sim 5$, where fluxes in four separate bandpasses are available. The simulations we perform in Appendix B.3 suggest factors of $\sim$1.5 improvement in the uncertainties on β at $z \sim 4$ and $z \sim 5$. On the other hand, the second approach has the advantage that all UV-continuum slope β determinations are made using a similar wavelength baseline at all redshifts. As a result, even if the spectral energy distribution (SED) of galaxies in the rest-frame UV is not a perfect power law (e.g., from the well-known bump in dust extinction law at 2175 Å; Stecher 1965), we would expect β determinations made at one redshift to show no systematic offset relative to those made at another, allowing for more robust measurements of evolution across cosmic time.

After some testing, we adopted the approach that utilizes all the available flux information to determine the UV-continuum slopes β. Figure 4 provides an example of such a determination for a $z \sim 4$ galaxy in our HUDF sample and an example of

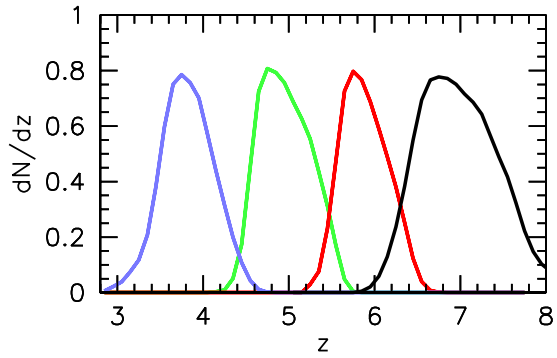

Figure 3. Predicted redshift distribution for our $z\sim4$, $z\sim5$, $z\sim6$, and $z\sim7$ Lyman-break samples from the HUDF. The mean redshifts for these samples are 3.8, 5.0, 5.9, 7.0, respectively. The three lower redshift selections are essentially the same as those presented in Bouwens et al. (2007; though the present selection window for $z\sim6$ galaxies cuts off at $z\gtrsim6.2$) while the $z\sim7$ selection is similar to that presented in Bouwens et al. (2011b) but extends to slightly higher redshifts (Section 3.2). This maximizes the size of our $z\sim7$ samples while extending our selection to the highest redshift possible without sources suffering significant contamination from Lyα emission or IGM absorption. The redshift distribution for our Lyman-break samples from our other search fields are similar to those shown here.

(A color version of this figure is available in the online journal.)

Table 3
Wavebands Used to Derive the UV Continuum Slope for Individual Galaxies in Our $z\sim4$, $z\sim5$, $z\sim6$, and $z\sim7$ Samples[a]

Sample	Filters used to Derive β	Mean Rest-frame Wavelength[b]
	HUDF09 Observations	
$z\sim4$	$i_{775}z_{850}Y_{105}J_{125}$	2041 Å
$z\sim5$	$z_{850}Y_{105}J_{125}H_{160}$	1997 Å
$z\sim6$	$Y_{105}J_{125}H_{160}$	1846 Å
$z\sim7$	$J_{125}H_{160}$	1731 Å
	ERS Observations	
$z\sim4$	$i_{775}I_{814}z_{850}Y_{098}J_{125}$	2041 Å
$z\sim5$	$z_{850}Y_{098}J_{125}H_{160}$	1997 Å
$z\sim6$	$Y_{098}J_{125}H_{160}$	1784 Å
$z\sim7$	$J_{125}H_{160}$	1731 Å
	CDF-S CANDELS Observations	
$z\sim4$	$i_{775}I_{814}z_{850}Y_{105}J_{125}$	2041 Å
$z\sim5$	$z_{850}Y_{105}J_{125}H_{160}$	1997 Å
$z\sim6$	$Y_{105}J_{125}H_{160}$	1846 Å
$z\sim7$	$J_{125}H_{160}$	1731 Å

Notes.
[a] These filters probe the UV-continuum light of sources without contamination from Lyα emission or the position of the Lyman break (being sufficiently redward of the 1216 Å). See Section 3.3.
[b] Geometric mean.

such a determination for a $z\sim6$ galaxy. The passbands we will consider in deriving the slopes include the $i_{775}z_{850}Y_{105}J_{125}$ bands for $z\sim4$ galaxies, the $z_{850}Y_{105}J_{125}H_{160}$ bands for $z\sim5$ galaxies, the $Y_{105}J_{125}H_{160}$ bands for $z\sim6$ galaxies, and the $J_{125}H_{160}$ bands for $z\sim7$ galaxies. We include the I_{814} band in these fits for $z\sim4$ galaxies over the ERS/CANDELS fields. We replace the Y_{105} band with the Y_{098} band in these fits for galaxies over the ERS field. In selecting these passbands, we explicitly excluded passbands which could be contaminated by Lyα emission, the Lyman-continuum break, or flux redward of the Balmer break. These choices are motivated by our expected redshift distributions for these samples (Figure 3). Table 3 includes a list of all the bands we use to perform these fits. The

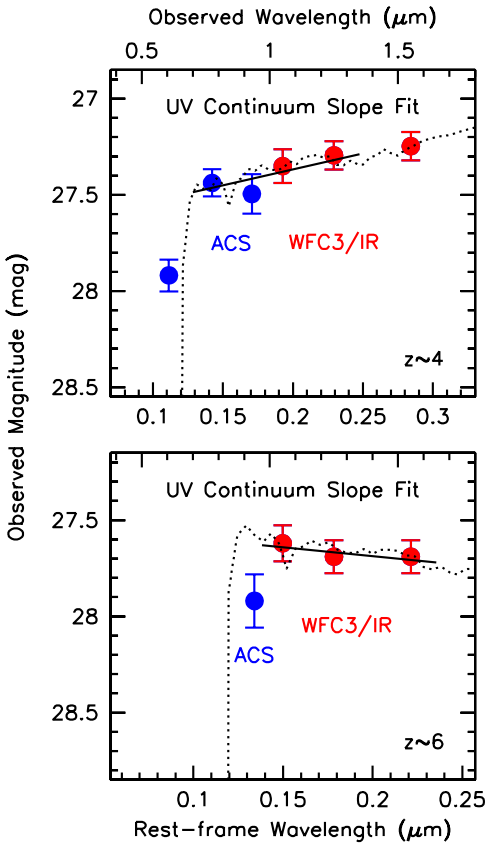

Figure 4. Upper panel: illustration of how we estimate the UV-continuum slope for a $z\sim4$ galaxy candidate (see Section 3.3). The blue and red points show the observed magnitudes for the galaxy in the ACS and WFC3/IR observations, respectively. The H_{160} band is not used for determining the UV-continuum slope β for our $z\sim4$ samples, since the H_{160}-band magnitudes for galaxies at the low-redshift end [$z\sim3.0$–3.5] of our $z\sim4$ samples will include a contribution from light redward of the Balmer break. The black line shows the UV-continuum slope we estimate for the source fitting to the i_{775}, z_{850}, Y_{105}, and J_{125} band photometry. The dotted black line is a plausible SED from a stellar population model which fits the observed photometry and is shown here to show where the major spectral features occur (but we emphasize that these SED fits are not used to establish the UV-continuum slopes). Using the full wavelength baseline provided by both the ACS and WFC3/IR observations (Table 3), we are able to establish the UV-continuum slopes β much more accurately than using the ACS observations alone. Lower panel: an illustration of how we estimate the UV-continuum slope β for a $z\sim6$ galaxy. The UV-continuum slopes β for $z\sim6$ galaxies are derived using the full flux information in the Y_{098}/Y_{105}, J_{125}, and H_{160} bands (Table 3).

(A color version of this figure is available in the online journal.)

mean rest-frame wavelengths for our derived UV-continuum slopes β at $z\sim4$, $z\sim5$, $z\sim6$, and $z\sim7$ are 2041 Å, 1997 Å, 1846 Å, and 1731 Å, respectively.

In determining the UV-continuum slopes β from the flux information just discussed, we find the UV-continuum slope β that minimizes the value of χ^2:

$$\chi^2 = \Sigma_i \left(\frac{f_i - f_0 \lambda^\beta}{\sigma_i} \right)^2, \quad (1)$$

where f_i and σ_i are the observed fluxes and uncertainties, respectively, β is the best-fit UV-continuum slope, and f_0 is the best-fit normalization factor. The fluxes $f_i \pm \sigma_i$ in the above fits are from photometry of the full ACS+WFC3/IR data set PSF matched to the WFC3/IR H_{160} band, using typical Kron-style apertures.

This photometry is therefore distinct from that used to select our $z\sim4$, $z\sim5$, and $z\sim6$ samples, since sources in our $z\sim4$, $z\sim5$, and $z\sim6$ Lyman-break samples were selected based on catalogs where the PSF matching was done to the ACS z_{850} band. This approach offers two clear advantages. (1) By selecting sources based on catalogs where the PSF matching is done to the z_{850} band, therefore making our photometric apertures smaller, we utilize much higher S/N photometry for the selection process, improving the robustness of our $z\sim4$, 5, and 6 selections. (2) By using different photometry (and smaller apertures) to select sources than we use to estimate β (typically involving larger apertures), we ensure that our β measurements are not subject to exactly the same noise as affects source selection (because the photometric apertures are different and will have somewhat different noise characteristics). This makes our $z\sim4$–6 β measurements less susceptible (by ∼50%) to the biases that arise from a coupling of errors in our β measurements with similar errors in our photometric selection ("photometric error coupling bias"; Appendix B.1.2). For our $z\sim7$ Lyman-break sample, however, the photometry used to estimate β is the same as what we use to select the sources. See Section 3.1 for a description of the photometry.

In Appendix A, we show that the present approach produces similar results to that based on UV colors spanning the wavelength range 1600 Å to 2200 Å (but with much smaller errors). For typical sources, the derived β's agree to within $\delta\beta\sim0.1$ which is about as well as we can determine β using UV colors (where possible systematics in β estimates are on the order of ∼0.1). The present UV-continuum slope β estimates should therefore be directly comparable with others in the literature (Bouwens et al. 2006, 2009, 2010a; Meurer et al. 1999; Ouchi et al. 2004a; Stanway et al. 2005; Finkelstein et al. 2010) where the wavelength baseline 1600 Å to 2200 Å was typical for β determinations.

In deriving β's for sources in our samples from the available photometry, we tested for significant deviations from a pure power-law shape. This is important for ensuring that the model we use to characterize the UV-continuum SEDs of sources is meaningful. For the average source, we found that the observed photometry and the best-fit power-law SED differed by less than ∼0.02 mag. Such deviations are not large enough to have a sizeable impact on our β determinations, shifting the observed β determinations by $\lesssim$0.1. Such changes are well within the uncertainties we quote on our β determinations (Section 3.5).

3.4. Possible Selection and Measurement Biases

To establish the actual distribution of UV-continuum slopes β from the observations, we must account for the effect that object selection and measurement have on the observed distribution. These effects can cause the observed distribution to look very different from what it is in reality. Examples of such effects include (1) our LBG selection criteria preferentially including those galaxies in our samples with the bluest UV-continuum slopes and (2) photometric noise increasing the spread in the measured UV-continuum slopes β.

To correct for these selection and measurement biases, we follow a very similar procedure to what we used in our first major study of the UV-continuum slope β distribution at high redshift (Bouwens et al. 2009). We create mock catalogs of galaxies, generate artificial images for each source in our catalogs, add these sources to the real observations, and then reselect the sources and measure their properties in the same way as with the real observations. We then determine the approximate biases

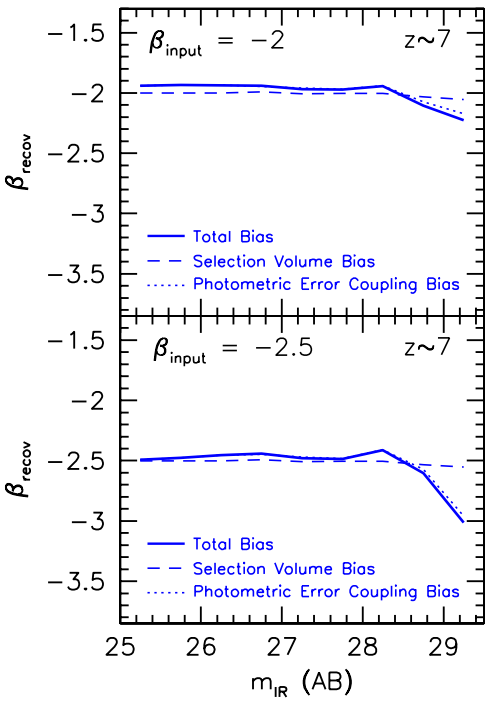

Figure 5. UV-continuum slopes β expected to be recovered in HUDF09-depth $z\sim7$ selections assuming specific input values for the UV-continuum slope β (Section 3.4; Appendix B). The results are shown as a function of IR magnitude and based on simulations with $>10^5$ galaxies. The expected biases in the recovered UV-continuum slopes β that result from β-dependent selection effects (blue dotted lines: Figure 21 and Appendix B.1.1) and from any coupling of the photometric errors in the measurement process to source selection (dashed blue lines: Appendix B.1.2) are presented separately. The solid blue line shows the β's we recover including both effects. The results of similar simulations for $z\sim4$, $z\sim5$, and $z\sim6$ selections are shown in Figure 22 in Appendix B. Overall, the UV-continuum slopes β we recover are very similar to the input slopes ($\Delta\beta\lesssim0.15$). One possible exception would the faintest luminosity bin in our $z\sim7$ sample, but we emphasize that even in this regime our corrected β measurements appear to be accurate, given their excellent agreement with other largely bias-free estimates we make (see Section 4.8). This strongly suggests that biases in our derived UV-continuum slope β distributions are very small overall.

(A color version of this figure is available in the online journal.)

that we would expect in the mean UV-continuum slope and 1σ scatter due to source selection or photometric scatter. We compute these biases as a function of magnitude for each of our data sets. To ensure that we are able to determine the relevant biases to high precision, we repeat these experiments for $>10^5$ artificial galaxies.

Appendix B provides a detailed discussion of the simulations we use to estimate the likely biases in the UV-continuum slope β distribution and establish the needed corrections.

Figure 5 shows the results of these simulations for $z\sim7$ selections. The effect of biases related to the LBG selection itself (Figure 21) and due to a possible coupling between the selection and measurement processes ("photometric error coupling bias") is shown explicitly. It is immediately clear from this figure that we can successfully recover the input values of the UV-continuum slopes β and do not expect especially large biases in the derived slopes. We include similar panels for our $z\sim4$, $z\sim5$, and $z\sim6$ selections in Figure 22 of Appendix B.

An important check to perform in assessing the overall quality of our UV-continuum slope determinations here is to compare the results from our deep data with the results from our wide data. Such a check is provided in Figure 25

of Appendix B, and it seems clear that the results from the HUDF09 and ERS+CANDELS data sets are in good agreement ($\Delta\beta \lesssim 0.1$–0.2) over the luminosity range where they overlap and have good statistics. This suggests that the UV-continuum slope β distributions we recover are accurate and free of any sizeable biases.

3.5. Establishing the β Distribution over a Wide Luminosity Baseline

We can utilize the UV-continuum slopes β measured for individual sources (Section 3.3) to establish the distribution of UV-continuum slopes β as a function of luminosity for each of our $z \sim 4$–7 LBG samples.

To establish this distribution while properly accounting for the relevant selection and measurement biases, we analyze the UV-continuum slope distribution for each data set and Lyman-break sample separately. We determine the mean UV-continuum slope and 1σ scatter. We correct the mean and scatter for the relevant biases (Appendix B and Section 3.4). Typical corrections in the mean UV-continuum slope β are $\lesssim$0.1 in general; the corrections do, however, reach values of $\Delta\beta \sim 0.1$ near the selection limit of our shallow and deep probes.

When determining the mean and scatter for each distribution, we use the biweight mean $C_{\rm BI}$

$$C_{\rm BI} = M + \frac{\sum_{|u_i|<1}(x_i - M)\left(1-u_i^2\right)^2}{\sum_{|u_i|<1}\left(1-u_i^2\right)^2}$$

and biweight scale $S_{\rm BI}$

$$S_{\rm BI} = n^{1/2}\frac{\left[\sum_{|u_i|<1}(x_i - M)^2\left(1-u_i^2\right)^4\right]^{1/2}}{\left|\sum_{|u_i|<1}\left(1-u_i^2\right)\left(1-5u_i^2\right)\right|},$$

where $u_i = (x_i - M)/(c\,{\rm MAD})$, ${\rm MAD} = {\rm median}(|x_i - M|)$, M is the median of the x_i's, x_i is the data, n is the number of sources summed over, and c is the "tuning constant" (Beers et al. 1990). c is taken to be equal to 6 in computing the biweight mean and 9 in computing the biweight scale. Use of robust statistics like the biweight mean and scale is valuable, given that a small fraction of the sources in our samples may be contaminated by light from nearby sources or may lie outside the target redshift range. Biweight mean determinations of β are similar to median determinations of β (median difference $\Delta\beta \sim 0.01$ with $\sim$0.04 scatter), but somewhat bluer ($\Delta\beta \sim 0.1$) than mean determinations (due to the β distribution having a somewhat extended tail toward red β's and the biweight mean de-weighting the tail).

For the absolute magnitude of each galaxy in the UV, we use the mean absolute magnitude of that source in all the *HST* bands that contribute to its UV-continuum slope determinations (Table 3). By using the geometric mean for this luminosity, we aim to avoid giving too much weight to the bluer or redder bands in defining this luminosity and hence artificially creating a correlation between the derived UV-continuum slope β and UV luminosity.

Figure 6 shows the UV-continuum slope β distribution versus the magnitude for our $z \sim 4$, $z \sim 5$, $z \sim 6$, and $z \sim 7$ samples. Scatter in the β distribution is relatively modest for our $z \sim 4$ and $z \sim 5$ samples, but is larger for our $z \sim 6$ and $z \sim 7$ samples. This is the result of the fact that our $z \sim 4$–5 samples use a larger number of passbands and larger wavelength baseline to measure the UV-continuum slope β.

Table 4
The Biweight Mean UV-continuum Slope β and 1σ Scatter of Galaxies, as a Function of UV Luminosity[a, b]

$\langle M_{\rm UV,AB}\rangle$	UV-continuum Slope β	
	Mean[c]	1σ Scatter[d]
	$z \sim 4$	
−21.50	$-1.75 \pm 0.04 \pm 0.10$	0.38
−20.50	$-1.88 \pm 0.02 \pm 0.10$	0.33
−19.50	$-2.01 \pm 0.02 \pm 0.10$	0.27
−18.50	$-2.16 \pm 0.03 \pm 0.10$	...[e]
−17.50	$-2.24 \pm 0.06 \pm 0.10$	...[e]
−16.50	$-2.20 \pm 0.07 \pm 0.10$	...[e]
	$z \sim 5$	
−21.50	$-1.64 \pm 0.08 \pm 0.10$	0.25
−20.50	$-1.93 \pm 0.05 \pm 0.10$	0.34
−19.50	$-2.14 \pm 0.04 \pm 0.10$	0.39
−18.50	$-2.17 \pm 0.06 \pm 0.10$	...[e]
−17.50	$-2.35 \pm 0.11 \pm 0.10$	...[e]
	$z \sim 6$	
−21.50	$-1.78 \pm 0.11 \pm 0.14$	...[e]
−20.50	$-2.08 \pm 0.08 \pm 0.14$	...[e]
−19.50	$-2.30 \pm 0.13 \pm 0.14$	...[e]
−18.50	$-2.30 \pm 0.11 \pm 0.14$	...[e]
−17.50	$-2.54 \pm 0.17 \pm 0.14$	...[e]
	$z \sim 7$	
−21.25	$-1.89 \pm 0.10 \pm 0.28$	...[e]
−20.25	$-2.25 \pm 0.13 \pm 0.28$	...[e]
−19.25	$-2.15 \pm 0.12 \pm 0.28$	...[e]
−18.25	$-2.68 \pm 0.19 \pm 0.28$	...[e]

Notes.
[a] The biweight mean UV-continuum slopes β presented here are also shown in Figure 6.
[b] The slopes presented here have been corrected for selection effects and measurement errors (see Section 3.4 and Appendix B). The tabulated UV luminosities are the geometric mean of the measured luminosities in the bands used to establish the UV slope (see Table 3).
[c] Both random and systematic errors are quoted (presented first and second, respectively). In Section 3.5, we provide a brief motivation for our estimates of the approximate systematic error in the biweight mean UV-continuum slope β.
[d] The 1σ scatter presented here has been corrected for photometric scatter using the simulations described in Appendix B and therefore should reflect the intrinsic 1σ scatter in the UV-continuum slope β distribution. Typical uncertainties are $\sim$0.1.
[e] It is challenging to establish the intrinsic 1σ scatter in the β distribution in this magnitude interval to $\lesssim$0.1 accuracy in σ_β either because of a large photometric scatter in the individual β measurements or because of a limited number of sources.

In Table 4, we present our corrected determinations of the biweight mean UV-continuum slope and 1σ scatter as a function of UV luminosity, for our $z \sim 4$, $z \sim 5$, $z \sim 6$, and $z \sim 7$ samples. We also include an estimate of the uncertainties in the biweight mean UV-continuum slopes that result from the measurement uncertainties, intrinsic scatter in the β distribution, and small number statistics.

For the systematic error on our UV-continuum slope measurements, we conservatively adopt values of 0.10–0.28. The dominant component of this error comes from uncertainties in our photometry. Allowing for small errors in the photometric zero points, aperture corrections, and PSF matching, we estimate a maximum error of 0.05 mag in our flux

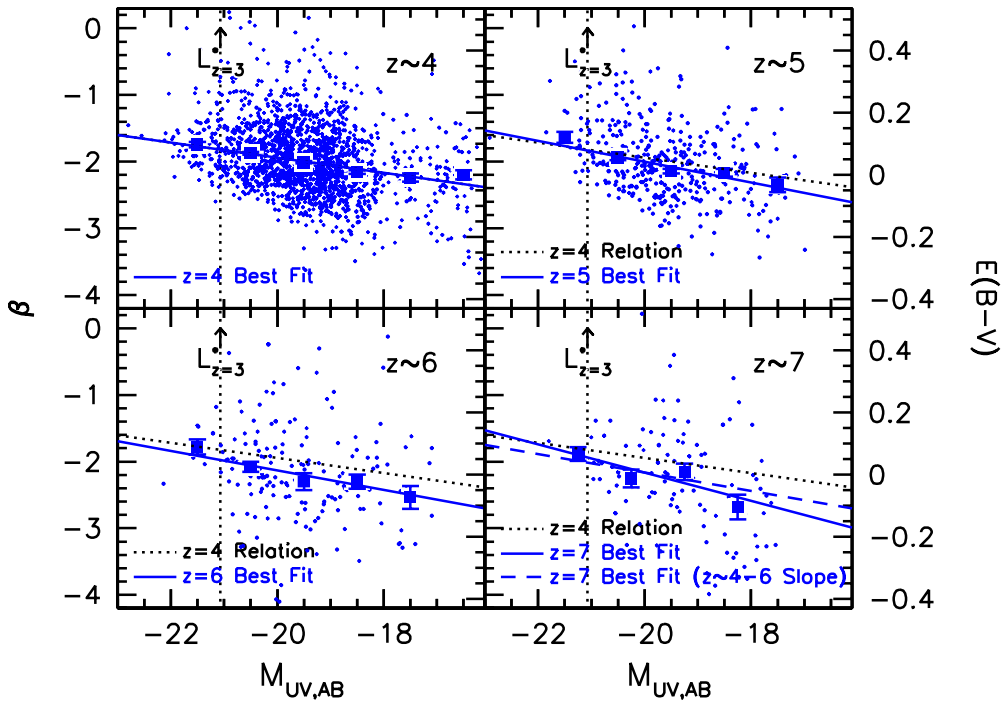

Figure 6. Determinations of the UV-continuum slope β distribution vs. UV luminosity for star-forming galaxies at $z\sim4$ (upper left), $z\sim5$ (upper right), $z\sim6$ (lower left), and $z\sim7$ (lower right). The blue points show the UV-continuum slope β determinations for individual sources in our samples. The large blue squares show the biweight mean UV-continuum slope β determinations in each magnitude interval and error on the mean. We take the absolute magnitude of each galaxy in the UV to be equal to the mean absolute magnitude of that source in all the *HST* bands that contribute to its UV-continuum slope determinations (Table 3). The blue solid line in each panel shows the best-fit relationship (see Table 5 and Figure 7 for the best-fit parameters). The $z\sim7$ panel also includes a fit to the binned determinations but keeping the slope of the line fixed to the average $d\beta/dM_{\rm UV}$ found for our $z\sim4$, $z\sim5$, and $z\sim6$ samples (dashed line). The dotted black line in the $z\sim5$, $z\sim6$, and $z\sim7$ panels shows the best-fit relationship at $z\sim4$ and is included for comparison. The vertical dotted line indicates the absolute UV magnitude for $L^*_{z=3}$ galaxies. For our $z\sim4$ and $z\sim5$ samples, the observed dispersion in UV-continuum slopes β about the mean relation (blue line) is relatively small (see also Table 4 and Figure 18). The intercept to the UV-continuum slope β vs. luminosity relationship appears to become slightly bluer toward higher redshift. However, the slope of the UV-continuum slope β vs. luminosity does not show any significant evolution as a function of redshift (see also Figure 7).

(A color version of this figure is available in the online journal.)

measurements. This translates into possible systematic errors of 0.10, 0.10, 0.14, and 0.28 in the β measurements at $z\sim4$, $z\sim5$, $z\sim6$, and $z\sim7$.

We also allow for small systematic errors in our UV-continuum slope β measurements as a result of differences in the wavelength baseline we use to derive β (Table 3). These differences would have an effect on the β's we derive from the available photometry, if the UV SEDs differed substantially from a pure power-law form (i.e., f_λ^β). The tests we perform in Appendix A suggest that the relevant systematic errors are small $\Delta\beta\lesssim0.13$. Similar β's are found from fits using the full UV continuum (Section 3.3 and Figure 4) as are found using a smaller wavelength range.

3.6. Dependence of β on Luminosity

We observe a clear trend in the UV-continuum slope β as a function of UV luminosity in all four LBG samples, such that the UV-continuum slope β becomes progressively bluer at fainter luminosities (Figures 6 and 25). Such trends in β had already been identified by Bouwens et al. (2009) in their analyses of $z\sim2.5$ and $z\sim4$ galaxy samples (see also Meurer et al. 1999; Labbé et al. 2007; Figure 8 of Overzier et al. 2008) and by Bouwens et al. (2010a) in their analyses of $z\sim5$–7 galaxies (see also Wilkins et al. 2011). The observed luminosity dependence of β is thought to be due to a change in the dust content and perhaps the age of galaxies as a function of luminosity (Labbé et al. 2007; Bouwens et al. 2009). It is likely to be a manifestation of the well-established mass–metallicity relationship seen at a wide variety of redshifts (e.g., Tremonti et al. 2004; Erb et al. 2006a; Maiolino et al. 2008).

The UV-continuum slope β shows an approximately linear relationship on the magnitudes $M_{\rm UV}$ of the sources (Figure 6), and therefore it makes sense for us to model this relationship using a first-order polynomial and determine the best-fit slopes $d\beta/dM_{\rm UV}$ and intercepts $\beta_{M_{\rm UV}=-19.5}$.

In fitting a line to our UV-continuum slopes, we use a finer binning (i.e., 0.5 mag) than shown in Figure 6 to minimize the impact of the binning scheme on the best-fit slopes and intercept. The results of our fits to the biweight means are shown as blue lines in Figure 6, and it is clear that the mean β's are well fit by the lines.[8] The fits exhibit a similar dependence on the UV magnitude $M_{\rm UV}$ at each redshift. The intercept to the lines is also similar at all redshifts but appears to evolve monotonically with cosmic time. The best-fit parameters—slope and intercept—we derive for these lines are presented in Table 5 and Figure 7. These determinations are in excellent agreement with previous work, as we discuss in Section 4.

4. COMPARISON TO PREVIOUS RESULTS

In the present section, we compare the present observational results on the UV-continuum slope β with those previously

[8] There may nonetheless be weak evidence in the results from our $z\sim4$ and $z\sim5$ samples that the dependence of β on luminosity is weaker faintward of -18 mag (see Figure 6).

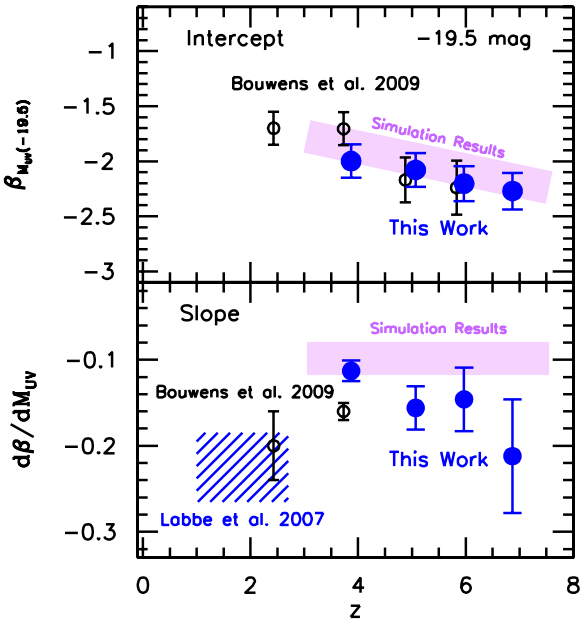

Figure 7. Slope and intercept of the UV-continuum slope–luminosity relationship as a function of redshift (Section 3.6; see also Table 5). Upper panel: intercept of the UV-continuum slope–luminosity relationship, as a function of redshift (large blue circles). Previous determinations of the intercept to the β-luminosity relationship are also shown (open black circles: Bouwens et al. 2009). The shaded lavender region represents the predictions from the cosmological hydrodynamical simulations of Finlator et al. (2011; Section 5.1). We use −19.5 AB mag as the intercept, because of the substantial UV-continuum slope measurements there at all redshifts. An apparent reddening of the UV-continuum slope β at −19.5 AB mag ($0.25L^*_{z=3}$) with cosmic time is observed, from $z\sim7$ to $z\sim2.5$. Lower panel: slope of the UV-continuum slope–luminosity relationship, as a function of redshift (large blue circles). Previous determinations of this dependence on luminosity at $z\sim1$–3 (blue shaded region; Labbé et al. 2007) and at $z\sim2.5$ and $z\sim4$ (open black circles; Bouwens et al. 2009) are also shown. The shaded lavender region is as in the upper panel. A very similar dependence of β on UV luminosity is observed over the entire redshift range $z\sim7$ to $z\sim1$.

(A color version of this figure is available in the online journal.)

Table 5
Best-fit Slopes and Intercepts to the UV-continuum Slope β to UV Luminosity Relationship

Dropout Sample	Mean Redshift	$\beta_{M_{\rm UV}=-19.5}$	$d\beta/dM_{\rm UV}$
B_{435}	3.8	$-2.00\pm0.02\pm0.10$	-0.11 ± 0.01[a]
V_{606}	5.0	$-2.08\pm0.03\pm0.10$	-0.16 ± 0.03[a]
i_{775}	5.9	$-2.20\pm0.05\pm0.14$	-0.15 ± 0.04[a]
z_{850}	7.0	$-2.27\pm0.07\pm0.28$	-0.21 ± 0.07
U_{300}[b]	2.5	$-1.70\pm0.07\pm0.15$	-0.20 ± 0.04

Notes. Section 3.6, see also Figure 7.
[a] While the $d\beta/dM_{\rm UV}$ slopes for our $z\sim4$, 5, and 6 samples are quite similar overall, these slopes show even better agreement if we consider the correlations over the same luminosity range, i.e., excluding β determinations faintward of −17 AB mag. In this case, we find a $d\beta/dM_{\rm UV}$ slope of -0.13 ± 0.02 for our $z\sim4$ sample.
[b] From Bouwens et al. (2009).

obtained in the literature (Figure 8). The goal is to assess the robustness of the present observational results and to give some perspective on which trends are gaining widespread observational support.

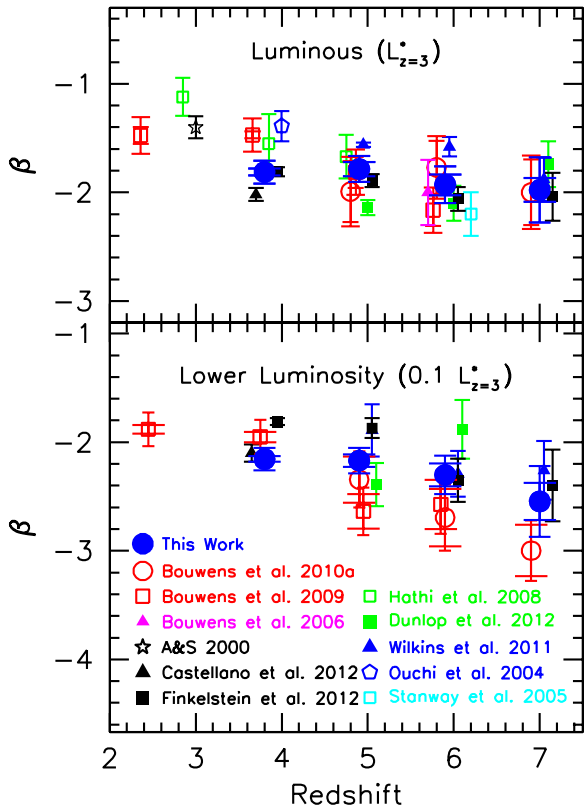

Figure 8. Comparison of the biweight mean UV-continuum slopes β found here (solid blue circles) for luminous (L^*/−21 AB mag; top panel) and lower luminosity ($0.1L^*_{z=3}$/−18.5 AB mag; bottom panel) galaxies with values in the literature. Generally we only compare with the mean UV-continuum slope determinations from the literature since a biweight mean slope is not specified. However, as described in Figure 7, the biweight mean values for β tend to be somewhat bluer ($\Delta\beta\sim0.1$) than the mean values. Included in this figure are UV-continuum slope determinations from Bouwens et al. (2010a; red open circles), Bouwens et al. (2009; red open squares), Bouwens et al. (2006; magenta triangle), Adelberger & Steidel (2000; open black star), Ouchi et al. (2004a; open blue pentagon), Stanway et al. (2005; open cyan square), Hathi et al. (2008; open green squares), Dunlop et al. (2012; solid green squares), Wilkins et al. (2011; blue triangles), Castellano et al. (2012; solid black triangles), and Finkelstein et al. (2012; solid black squares). In general, we find good agreement with our previous UV-continuum slope determinations (Bouwens et al. 2009, 2010a) although the current results are a little redder at lower luminosities. There is a moderate amount of scatter in the observational results at lower luminosities (see Section 4).

(A color version of this figure is available in the online journal.)

4.1. Comparison with Bouwens et al. 2009 ($z\sim3$–6)

Before the WFC3/IR camera on *HST* became operational, Bouwens et al. (2009) made use of the ACS+NICMOS observations to quantify the distribution of UV-continuum slopes β for star-forming galaxies over range in redshift ($z\sim2.5$–6) and luminosities. Bouwens et al. (2009) derive β directly from the UV colors (e.g., as in Appendix A). How do the present UV-continuum slope determinations compare with those from Bouwens et al. (2009)? Both old and new results are shown in Figure 8. Comparing the UV-continuum slope measurements made on the identical sources in the two data sets (old ACS+NICMOS data versus the new WFC3/IR observations), we find reasonable agreement, with mean offsets $\beta_{\rm WFC3/IR}-\beta_{\rm ACS+NICMOS}$ of only −0.10, 0.04, 0.09 in the derived β's at $z\sim4$, $z\sim5$, and $z\sim6$, respectively. The biweight mean UV-continuum slopes β found here are also in good agreement with the slopes derived by Bouwens et al. (2009). At $z\sim4$ and

$z \sim 5$, the present biweight mean β's are just $\sim$0.26 bluer and $\sim$0.16 redder than the values found in Bouwens et al. (2009); the present biweight mean β's at $z \sim 6$ show no average shift at all relative to the values found by Bouwens et al. (2009). $\Delta\beta \sim 0.1$ of the differences result from our use of the more robust biweight means to express the central β's, so the agreement is quite good overall.

4.2. Comparison with Bouwens et al. 2010a ($z \sim 5$–7)

Bouwens et al. (2010a) took advantage of the first-year WFC3/IR observations over the HUDF and the ERS WFC3/IR observations to quantify the UV-continuum slope β distribution to higher redshifts ($z \sim 7$) and lower luminosities. How do the present determinations of the UV-continuum slope β compare with Bouwens et al. (2010a)? At high luminosities, we find excellent agreement, with both studies preferring mean UV-continuum slopes β of -2 (see Figure 8). At lower luminosities, however, we now find somewhat redder values of the UV-continuum slope β, i.e., $\Delta\beta \sim 0.2$–0.4 than found by Bouwens et al. (2010a). The observed differences in the mean UV-continuum slope β seem to have resulted from both the small number of sources in previous samples and uncertainties in the photometry of faint sources in the early HUDF09 data. We remark that the current WFC3/IR observations of the HUDF from the HUDF09 WFC3/IR program are approximately twice as deep as what Bouwens et al. (2010a) used.

4.3. Comparison with the Literature: Does β Correlate with Redshift?

In the present analysis, we find that the UV-continuum slope β shows a correlation with the redshift of galaxies, with higher redshift galaxies being bluer. This evolution is evident both in Figure 6 (compare the solid lines in the $z \sim 5$, $z \sim 6$, $z \sim 7$ panels with the dotted lines) and in Figure 7.

How does the correlation we find compare with other studies? A brief summary of the evidence for this redshift dependence is provided in Figure 8, and there is a clear trend from bluer UV-continuum slopes β at $z \sim 6$–7 to redder slopes at $z \sim 2$–4. Essentially all studies of the UV-continuum slope over the range $z \sim 3$–7 (Lehnert & Bremer 2003; Stanway et al. 2005; Bouwens et al. 2006, 2009, 2010a; Wilkins et al. 2011; Finkelstein et al. 2012) find evidence for this evolution of β with redshift. The only exception to this is the recent study of Dunlop et al. (2012) who find no dependence (but Dunlop et al. 2012 do note that a comparison of their results with those at $z \sim 3$ does argue for evolution); we discuss the Dunlop et al. (2012) results in Section 4.5.

4.4. Comparison with the Literature: Does β Correlate with UV Luminosity?

As we discuss in Section 3.6, we find that the UV-continuum slope β shows a clear correlation with the rest-frame UV luminosity of galaxies, with lower luminosity galaxies being bluer at all redshifts. A good illustration of this correlation is provided in Figure 6. The best-fit relationship (solid blue line) shows almost exactly the same dependence for each high-redshift sample. The uniformity of the slope and modest variation as a function of redshift is also clearly illustrated in Figure 7. The uniformity extends even to our $z \sim 4$ samples. While β in these samples appear to show a somewhat weaker dependence on luminosity than our other samples, a slightly steeper dependence is found, i.e., $d\beta/dM_{\rm UV} = -0.13 \pm 0.02$, if we use the same luminosity baseline as our $z \sim 5$ and $z \sim 6$ samples (excluding sources faintward of -17 AB mag).

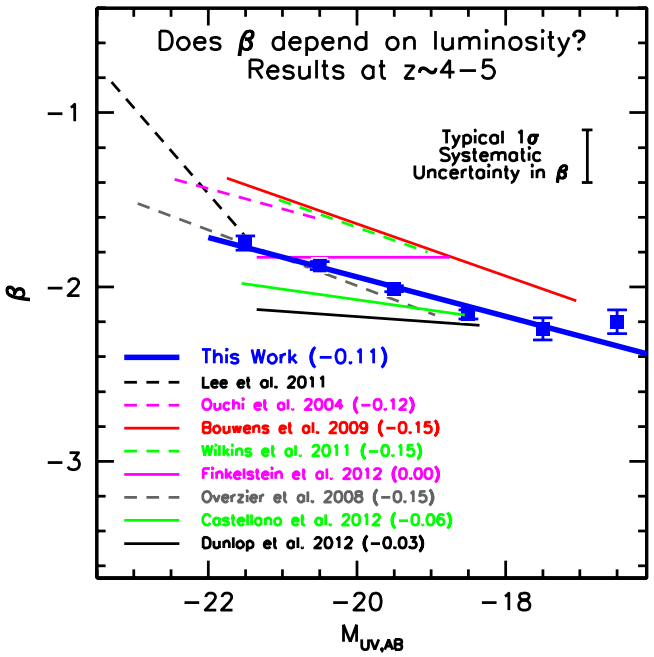

Figure 9. Dependence of the UV-continuum slope β on UV luminosity $M_{\rm UV}$ at $z \sim 4$–5, as determined by different analyses in the literature. The lines show the observed β–$M_{\rm UV}$ relations from Lee et al. (2011; dashed black), Bouwens et al. (2009; solid red), Wilkins et al. (2011; dashed green), Ouchi et al. (2004a; dashed magenta), Finkelstein et al. (2012; solid magenta), Overzier et al. (2008; dashed gray), Castellano et al. (2012; solid green), Dunlop et al. (2012; solid black), and the present work (blue). The blue squares are the β determinations at $z \sim 4$ from the present work. Error bars are 1σ. Also included in this figure in parentheses is the slope of the β–$M_{\rm UV}$ relationship $d\beta/dM_{\rm UV}$ determined in different analyses. In several cases (e.g., Ouchi et al. 2004a; Wilkins et al. 2011) shown here, we derived the plotted relations and $d\beta/dM_{\rm UV}$ slopes from the individual β determinations in those papers. The error bar in the lower left illustrates the approximate systematic uncertainties in previous β measurements. Similar luminosity dependencies are found at $z \sim 1$–3 by Labbé et al. (2007) and Bouwens et al. (2009; see Figure 7). A large number of independent analyses have found evidence for a similar correlation between UV luminosity and β (see Section 4.4). Brighter galaxies are consistently found to be redder in their β's and fainter galaxies are found to be bluer.

(A color version of this figure is available in the online journal.)

In general, the correlation we find agrees very well with most previous studies. Figure 9 shows different β determinations as a function of luminosity at $z \sim 4$–5 (Ouchi et al. 2004a; Overzier et al. 2008; Bouwens et al. 2009; Lee et al. 2011; Wilkins et al. 2011; Dunlop et al. 2012).[9] Despite some dispersion in the precise values of the β measurements and some small variance in the best-fit slopes $d\beta/dM_{\rm UV}$, nearly all published determinations of the UV-continuum slope β at $z \sim 4$–5 find bluer values for β at lower luminosities, with the same luminosity dependence. Two recent analyses that found minimal or no correlation of β with luminosity are those of Dunlop et al. (2012) at $z \sim 5$–7 and Finkelstein et al. (2012) at $z \sim 4$–5. We discuss the Dunlop et al. (2012) results in Section 4.5 and the Finkelstein et al. (2012) results in Section 4.7.

[9] The slopes we derive from Labbé et al. (2007) are based upon their results at 1700 Å and 3600 Å in their Figure 3. Previously, Bouwens et al. (2009) had estimated a slope of ~ -0.25 in the UV-continuum slope versus $M_{\rm UV}$ relationship at $z \sim 1$–2.7 from the Labbé et al. (2007) results based on a shorter 1700 Å and 2200 Å wavelength baseline (see Figure 7). The reason we use a more extended wavelength baseline to estimate β than Bouwens et al. (2009) had used is to allow for a fair comparison with the present β results (which use an extended wavelength baseline to estimate β; see Section 3.3).

Similar correlations with luminosity are found in the UV-continuum slope results at $z \sim 2$–3 (Labbé et al. 2007; Bouwens et al. 2009; Sawicki 2012) and in the UV–optical colors (Papovich et al. 2001; Labbé et al. 2007; González et al. 2012). Again, two analyses did not find a correlation of β with luminosity, and those are the Adelberger & Steidel (2000) and Reddy et al. (2008) analyses at $z \sim 2$–3. In these cases, not only was the luminosity baseline too short to provide much leverage for quantifying this correlation, but also the luminosity range probed was around L^* which is where the dispersion in dust properties relative to UV luminosity is at a maximum (e.g., Figure 13 of Reddy et al. 2010). However, when one adds the Adelberger & Steidel (2000) samples to the faint ($\sim$26–27 mag) $z \sim 2.5$ samples observed by Bouwens et al. (2009), a strong correlation is present (Figure 3 of Bouwens et al. 2009; see also Figure 5 of Sawicki 2012). Taken together these results indicate that there is also a clear trend with luminosity at $z \sim 2$–3.

4.5. Comparison with Dunlop et al. 2012 ($z \sim 5$–7)

Dunlop et al. (2012) use the WFC3/IR observations over the HUDF09 and ERS observations to quantify the UV-continuum slope distribution at $z \sim 5$–7. They select sources using a photometric redshift procedure and then measure their UV-continuum slopes β from the UV colors. In both respects, their procedure differs from that followed here (Sections 3.2 and 3.3). Overall, the individual UV-continuum slope β measurements of Dunlop et al. (2012) are in reasonable agreement with the present results (see Figure 8). The mean β they derive for bright $z \sim 5$ galaxies is $\Delta\beta \sim 0.3$ bluer and the mean β they derive for faint $z \sim 6$ galaxies is $\Delta\beta \sim 0.4$ redder. Given the quoted uncertainties on the measurements, the differences are not particularly significant.

The main differences arise when we look at the trends in the UV-continuum slope β with redshift and luminosity. Dunlop et al. (2012) find a mean UV-continuum slope β of galaxies equal to ~ -2.1, with no significant dependence on luminosity or redshift. This is in contrast to the strong correlation we find of β with both luminosity (Figures 6 and 7) and redshift (Figure 7). Their results are also inconsistent with the trends reported in the literature (Sections 4.3– 4.4; Figures 7 and 9).

We have attempted to understand the source of this difference both by a qualitative assessment of some issues that we know are important for obtaining reliable results and by a quantitative assessment using simulations (see Appendix D and Section 4.6). First, we remark that Dunlop et al. (2012) make no attempt to correct their mean β's for the fact that galaxies with bluer UV-continuum slopes β are easier to select than galaxies with redder UV-continuum slopes β. This effectively biases their UV-continuum slopes β to bluer values. It is a fairly straightforward process to correct for this issue (e.g., we describe such a correction in Appendix B.1.1 and Figure 5 where we show its effect).[10] Second, Dunlop et al. (2012) use an overlapping set of information both to select sources and to measure the UV-continuum slopes β. This biases their results (see Appendix D), though the magnitude of this bias is mitigated by their consideration of only the brightest sources.

Third, one further limitation of the Dunlop et al. (2012) analysis is their exclusion of the lowest luminosity sources. This significantly reduces the leverage they have to quantify trends in the mean UV-continuum slope as a function of luminosity. Dunlop et al. (2012) exclude faint sources because their simulations suggested that β could not be measured in an unbiased way. However, as we show in Appendices B and D, we are able to obtain reliable measurements (see also Section 4.6). Not only can we recover the mean UV-continuum slope for our samples to very faint magnitudes with excellent accuracy, but we can recover these slopes for samples selected using a photometric redshift procedure, if the information used for source selection is clearly separated from that used to measure β (see Figure 10).

[10] See also Figure 5 of Wilkins et al. (2011).

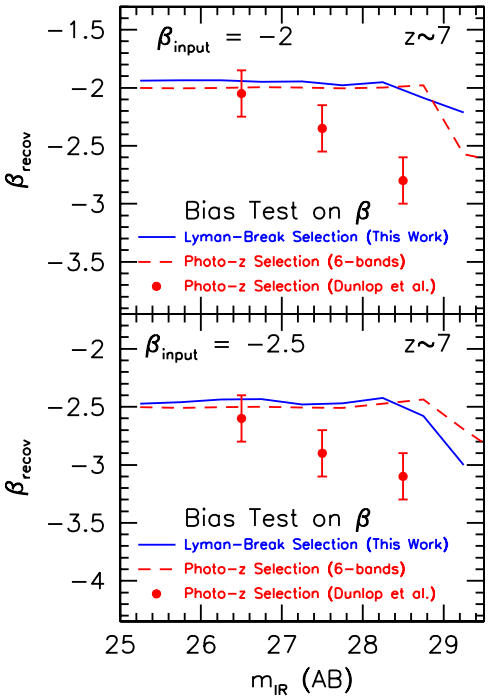

Figure 10. Comparison of the recovered UV-continuum slopes β vs. near-IR magnitude for a $z \sim 7$ galaxy population with input UV-continuum slopes β of -2.0 and -2.5 (see Appendix B for details). Shown are the results from the present Lyman-break selection (solid blue lines), from a six-band photometric redshift selection (dashed red lines), and from the Dunlop et al. (2012; D11) "robust" photometric redshift selections (solid red circles: from their Figure 8). The reason our measured UV-continuum slope measurements β are not significantly biased toward fainter magnitudes is that we select samples using a different part of the rest-frame UV SED (bluest two band passes redward of the break) than we use to measure the UV-continuum slope (second bluest bandpass and redder; see Figure 4). The situation is similar if one uses a six-band photometric redshift selection (Appendix D). By contrast, Dunlop et al. (2012) use overlapping information both to select their sources and to measure the UV-continuum slopes. Therefore, while photometric scatter in the bands we use for selection has little effect on our UV-continuum slope measurements, these steps are tightly coupled in the photometric redshift approach utilized by Dunlop et al. (2012). This results in the strong biases shown in this figure. While Dunlop et al. (2012) try to minimize the magnitude of these biases by restricting their analysis to the highest S/N sources, the same inherent biases in their β estimates will remain, but at a lower level. (see Section 4.6, and Appendices B.1.2 and D).

(A color version of this figure is available in the online journal.)

As mentioned above, these three issues led us to consider a more quantitative evaluation of the Dunlop et al. (2012) procedure so that we could better understand what was happening with their measurement of β. This is discussed in more detail in the next section.

4.6. Can β be Measured in a Largely Bias-free Way for Low S/N Sources?

As discussed above, a key question that has arisen in recent papers is whether it is possible to determine the UV-continuum

slope β distribution to very low luminosities with small biases. Dunlop et al. (2012), in particular, have suggested that it is not possible and have supported this suggestion with a series of simulations where they add noise to model galaxies and reselect these galaxies with their photometric redshift code. Dunlop et al. (2012) argue that noise in the photometry combined with a preference for selecting sources with blue colors would result in highly biased estimates for the mean UV-continuum slope β. Dunlop et al. (2012) show that such a bias toward bluer UV-continuum slopes at faint magnitudes is present in their mock data sets. Dunlop et al. (2012) argue that similar biases are likely present in Lyman-break selections, without further substantiating this claim.

We agree that selection biases can affect the distribution of UV-continuum slopes β. However, the size of these selection biases is extremely dependent upon how one selects the galaxies and measures their UV-continuum slopes β. As we show in Figure 10, our Lyman-break selections yield much smaller selection biases overall. The reason we expect biases in our selections to be small is that we select galaxies using a different part of the rest-frame UV SED (the bluest two passbands redward of the break) than we use to measure UV-continuum slopes (the second bluest passband and redder). As a result, photometric scatter in the bands we use to measure the UV-continuum slope β is largely independent of similar scatter in the bands we use for selection. Therefore, we would not expect our β measurements to be significantly biased as a result of the object selection process.[11]

Achieving similarly small biases to faint magnitudes with a photometric redshift technique is also possible. However, one must again be careful to use different information to select sources from what one uses to measure the UV-continuum slope β. To illustrate this, we consider the situation at $z\sim7$ in the current *HST* ACS + WFC3/IR data set. We have run simulations where we attempt to measure the mean UV-continuum slope β for a set of $z\sim7$ galaxies selected using a photometric redshift procedure. Both the simulations and results are discussed in Appendix D. We consider (1) the case where five *HST* bands are used to select sources and determine redshifts (this excludes those bands used to measure β), (2) the case where six bands are used (and so now including one of the two bands used to measure β), and (3) the case where all seven *HST* bands are used for selection and redshift determination (and so both bands used to measure β are also included to measure redshifts and select the sources). This latter approach is basically what Dunlop et al. (2012) do.

The results are shown in Figure 26 of Appendix D. While β measurements show substantial biases when all seven bands are used for the photometric redshift estimates (similar to the procedure of Dunlop et al. 2012) β measurements made using five or six bands show much smaller biases. This demonstrates that the UV-continuum slope β can be measured with very small biases to faint magnitudes.

4.7. Comparison with Finkelstein et al. 2012 ($z\sim4$–7)

In an independent analysis, Finkelstein et al. (2012) also use the recent WFC3/IR observations over the HUDF and CDF-South GOODS field to quantify the UV-continuum slope distribution for star-forming galaxies at $z\sim4$–8. Finkelstein et al. (2012) split sources into five different redshift samples using a photometric redshift procedure and then estimate β by finding the model SED which best fits the photometry of a source and deriving β from this model. Finkelstein et al. (2012) find that β shows a clear dependence on redshift, but report only a limited dependence on the UV luminosity.

β versus luminosity trends. While the redshift dependence Finkelstein et al. (2012) find for β is in excellent agreement with what we find (compare the solid black squares and large blue circles in the lower panel of Figure 8), the luminosity dependence Finkelstein et al. (2012) observe would appear to be considerably weaker. After all, Finkelstein et al. (2012) report no significant correlation of β with UV luminosity in their baseline analyses of their five redshift samples—seemingly very different than the clear correlation of β with luminosity we report.

Despite these apparent differences, the overall results from our two studies are actually in fairly good agreement. For example, with regard to the $z\sim6$ and $z\sim7$ samples, the best-fit $d\beta/dM_{\rm UV}$ values Finkelstein et al. (2012) find, i.e., -0.10 ± 0.07 and -0.20 ± 0.11, respectively, are strikingly similar to the values we find, i.e., -0.15 ± 0.04 and -0.21 ± 0.07, respectively.

For the $z\sim4$ and $z\sim5$ samples, Finkelstein et al. (2012) do not report a significant correlation between β and UV luminosity in what they identify as their baseline analysis (finding $d\beta/dM_{\rm UV}$ values of 0.01 ± 0.03 and 0.00 ± 0.06, respectively). However, in this analysis, Finkelstein et al. (2012) only make use of a 2 mag baseline in luminosity (due to their binning scheme), with their low luminosity anchor point largely coming from the relatively shallow ~1.6 orbit CANDELS data (with only a small contribution from the HUDF data). The CANDELS observations are clearly poorly suited to determine the trend in β to very low luminosities, given the very low S/N's and potentially large biases expected for the faintest sources in the CANDELS fields. However, the situation changes if we take advantage of the additional leverage in luminosity provided by the β measurements they provide for faint sources in the ultra-deep HUDF observations.

We can check this by extracting the HUDF measurements from Figure 5 of their paper. By comparing their median β measurements for brighter galaxies with their median β measurements for fainter galaxies in the HUDF, we find evidence for a significant correlation with luminosity. We find $d\beta/dM_{\rm UV}$ trends of -0.06 ± 0.02 and -0.13 ± 0.04, respectively. In the final version of their paper, Finkelstein et al. (2012) also note a similar correlation with luminosity making use of the faintest HUDF sources, finding $d\beta/dM_{\rm UV}$ trends of -0.07 ± 0.01 and -0.09 ± 0.03, respectively. While not in exact agreement with the trends we derive based on our own β measurements, i.e., -0.11 ± 0.01 and -0.16 ± 0.03, respectively, the agreement is much better. Use of the faint sources in the HUDF is important to take full advantage of the available leverage in luminosity to quantify the β versus $M_{\rm UV}$ trend.

In Figure 11, we show the β versus $M_{\rm UV}$ trend that Finkelstein et al. (2012) find in their baseline $z\sim4$ and $z\sim5$ analyses (magenta lines) and the trend we find from their measurements making exclusive use of sources from the HUDF to constrain β to fainter magnitudes (dashed red lines). In addition, we show the median β's Finkelstein et al. (2012) find for two fainter $z\sim4$ and $z\sim5$ subsamples within the HUDF (large solid red circles: we can extract β measurements for individual sources within the HUDF from their Figure 5) and the bootstrap uncertainties on these medians. In both samples there is a clear trend in the

[11] This issue is of course in addition to the normal selection biases that Lyman-break samples show against sources with red UV-continuum slopes β, but as we show in Appendix B.1.1 these biases are small for all but the reddest β's.

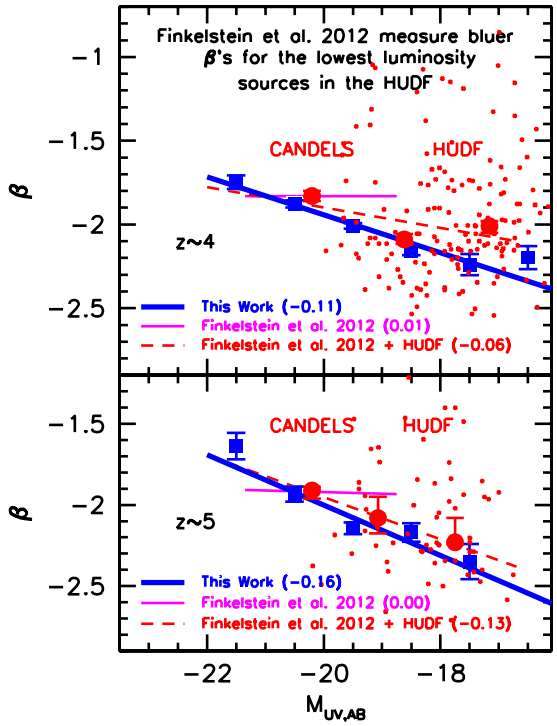

Figure 11. Upper panel: the approximate median UV-continuum slopes β (large red circles) derived by Finkelstein et al. (2012) for their sample as a whole (based primarily on the CANDELS+ERS programs) and two fainter subsamples from the HUDF ($-20 < M_{\rm UV} < -18$ and $-18 < M_{\rm UV} < -16$). The median β's we calculate for these two fainter subsamples and the bootstrap uncertainties on these medians, i.e., $-2.09^{+0.03}_{-0.03}$ and $-2.01^{+0.04}_{-0.03}$, respectively, are based on the β measurements plotted in Figure 5 of their paper (replicated here as the small red points). The solid magenta line shows the trend in β Finkelstein et al. (2012) derive in their baseline analysis. The dashed red line shows the trend we find comparing the median β's Finkelstein et al. (2012) measure for their sample as a whole (large red circle at ~ -20 mag) with the median β's we calculate for *their* two fainter subsamples in the HUDF (large red circles at ~ -19 mag and ~ -17 mag). The solid blue squares and lines are our own β determinations and are as shown in Figure 6. While Finkelstein et al. (2012) find no correlation between β and luminosity in their baseline analysis (magenta line), we observe quite a strong correlation with luminosity, making exclusive use of *their* fainter sources in the HUDF to define the trend to lower luminosities (red line). The trend $d\beta/dM_{\rm UV}$ we find making exclusive use of their β measurements for the fainter HUDF sources, i.e., -0.06 ± 0.02, is in much better agreement with what we find, i.e., -0.11 ± 0.01 than it is in their baseline analysis. The median β's Finkelstein et al. (2012) measure for sources in the two fainter-magnitude HUDF subsamples shown here (two large red circles) are also in very good agreement with our own measurements (blue squares), particularly at ~ -19 mag. Lower panel: similar to the upper panel, but comparing results from the $z \sim 5$ sample of Finkelstein et al. (2012) with our own results (see Section 4.7). The two fainter subsamples of $z \sim 5$ galaxies from the HUDF are over the magnitude ranges $-20.3 < M_{\rm UV} < -18.3$ and $-18.3 < M_{\rm UV} < -16.3$. As in the upper panel, we note better agreement with the Finkelstein et al. (2012) β measurements, if we restrict our comparison to their β measurements from the HUDF.

(A color version of this figure is available in the online journal.)

median β's toward bluer values at the lowest luminosities. It is striking how well the median β's Finkelstein et al. (2012) derive from the HUDF agree with our own β measurements, particularly in the luminosity interval [−20 mag, −18 mag]. While it is true that the median β's Finkelstein et al. (2012) derive for their entire ERS+CANDELS+HUDF09 sample are redder in general than what we find at these luminosities, these median β's receive their largest weight from the shallower ERS+CANDELS samples and therefore may be subject to substantial selection, measurement, or contamination biases (see the discussion at the end of this section).

Expected trend in luminosity. Finkelstein et al. (2012) defend the weak correlation of β they report versus luminosity (particularly as derived in their baseline analysis), arguing that β should show a stronger correlation with stellar mass than UV luminosity. We do not dispute this assertion; however, it would be most surprising if a correlation of β with stellar mass did not also appear as a correlation with UV luminosity. Given the correlation found between SFR and stellar mass in high-redshift galaxies (e.g., Stark et al. 2009; González et al. 2011; McLure et al. 2011; Lee et al. 2012; Reddy et al. 2012b), we would expect the UV luminosity to be broadly correlated with stellar mass. A similar conclusion can be drawn from high-redshift angular correlation function results. Higher luminosity galaxies are consistently found to be more clustered than lower luminosity galaxies (e.g., Ouchi et al. 2004b; Lee et al. 2006). Such would not be the case if UV luminosity was not correlated with mass (in this case halo mass). Independent of these considerations, we remark that β also shows a clear correlation with UV luminosity in various cosmological hydrodynamical simulations (e.g., Finlator et al. 2011; Dayal & Ferrara 2012), and the predicted trends (e.g., $d\beta/dM_{\rm UV} \sim -0.10$ is expected in the Finlator et al. 2011 simulations) are comparable to what we find (Figure 7).

Possible biases in the Finkelstein et al. measurements. Finkelstein et al. (2012) have suggested that the β–$M_{\rm UV}$ trends we find may be stronger than what they find due to the fact that we measure the UV luminosity at a different rest-frame wavelength than they do, and β versus $M_{\rm UV}$ trends may depend on this rest-frame wavelength. For our $z \sim 4$ samples, for example, we measure the rest-frame UV luminosity at 2041 Å (see Table 3) while Finkelstein et al. (2012) measure it at 1500 Å. We are in full agreement that $d\beta/dM_{\rm UV}$ will depend on the rest-frame wavelength. However, the results from Figure 3 in Labbé et al. (2007) suggest that one would find an even stronger $d\beta/dM_{\rm UV}$ trend at bluer wavelengths than one would find at redder wavelengths, which is different from what Finkelstein et al. (2012) find. It is therefore not clear if this explains the differences.

Instead, one might be concerned that the β versus $dM_{\rm UV}$ trend Finkelstein et al. (2012) find may be biased as a result of the rest-frame wavelength Finkelstein et al. (2012) use to measure the $M_{\rm UV}$ luminosity.[12] By determining luminosity at the blue end (at 1500 Å) of the wavelength baseline they use to derive β, Finkelstein et al. (2012) effectively introduce a coupling between the errors that affect both their β measurements and their determinations of the UV luminosity $M_{\rm UV}$. This could be problematic since any errors in the flux measurements of sources would cause sources to be either fainter and redder or brighter and bluer, causing the $d\beta/dM_{\rm UV}$ trend derived by Finkelstein et al. (2012) to be biased toward too high of values. Repeating the determination of $d\beta/dM_{\rm UV}$ at $z \sim 4$–5 based on our own flux measurements but basing $M_{\rm UV}$ on the flux measurement at the blue end of the wavelength baseline to derive β and using only the wide-area CANDELS+ERS sources, we estimate that this could bias the derived $d\beta/dM_{\rm UV}$ trend too high by $\Delta(d\beta/dM_{\rm UV}) \sim 0.05$. This bias would be analogous to the photometric error coupling bias we discuss in Appendix D. However, instead of the coupling being between source selection and the β measurements, it would be between the measurement

[12] Finkelstein et al. (2012) also discuss this issue at some length in their paper (as a source of differences between the β vs. $M_{\rm UV}$ trends we find) and would appear to find a similar effect, but given its importance for understanding differences between our results, we feel this discussion is worth repeating.

of β and the measurement of the UV luminosity $M_{\rm UV}$.[13] Contamination in the shallower CANDELS+ERS samples (from lower redshift galaxies) could also be an issue for Finkelstein et al. (2012) in deriving the trend in β to lower luminosities $M_{\rm UV}$.

Given the much smaller flux uncertainties for sources in the HUDF (and smaller contamination rates), we would expect the β's Finkelstein et al. (2012) measure there to show significantly smaller biases than β's measured for sources in ERS+CANDELS fields at the same luminosities. Encouragingly enough, the median β's Finkelstein et al. (2012) derive from the HUDF are in good agreement with our own, particularly in the luminosity interval [−20 mag, −18 mag] (compare the blue squares and large red circles in both the upper and lower panels of Figure 11).

Finally, we remark Finkelstein et al. (2012) use the same photometry both to select sources and measure β. Given the argumentation in the previous section and Appendix D (see also Dunlop et al. 2012), we might expect the bias in the derived β's to be non-zero. However, in practice, given the large number of passbands used to select sources and measure their redshifts, the bias is likely to be quite small except at $z\sim7$ (similar to our study: but see Section 4.8). Finkelstein et al. (2012) are aware of this issue and explicitly discuss it in their paper.

4.8. How Blue are Lower Luminosity Galaxies at $z\sim7$?

Galaxies with the most extreme UV properties are expected to lie at very high redshift and have low luminosities—given the early cosmic times in which they are observed and likely low masses. It has therefore been of considerable interest to establish the UV-continuum slopes β for the faintest observable $z\sim7$–8 galaxies. Early observations of such galaxies in the HUDF gave tantalizingly steep values of the UV-continuum slope β, i.e., $\beta\sim-3$.

In the present study, we find a mean UV-continuum slope β of -2.7 ± 0.2 for faint $z\sim7$ galaxies. This is slightly redder than the mean UV-continuum slope β (-3.0 ± 0.24) found in our earlier study of β for $z\sim7$ galaxies in the HUDF. It is also slightly redder than that (-3.0 ± 0.5) found by Finkelstein et al. (2010) using the same data.[14] Dunlop et al. (2012) have argued that it is not possible to estimate the UV-continuum slope β at such low luminosities, but as we discuss in Section 4.6, such measurements are possible if care is taken to minimize biases by ensuring the information used for selection is independent of that used to measure β.

How robust are our measurements of the mean UV-continuum slope β for faint $z\sim7$ galaxies? While our simulations suggest that the biases are not large, it is useful to check this result by obtaining an independent estimate of the mean β. For this estimate, we use two completely independent data sets to select sources and to measure β. Source selection is done using the first-year WFC3/IR observations over the HUDF (18 orbits Y_{105}, 16 orbits J_{125}, 28 orbits H_{160}) from the HUDF09 program while the measurement of β is done using the second-year WFC3/IR observations over the HUDF (18-orbit J_{125}, 25-orbit H_{160} data). Since the second-year data were not used to select the sample, we can make an unbiased measurement of the UV-continuum slope β for this sample using the new observations.[15] For comparison with the Bouwens et al. (2010a) study on β, we use the same $z\sim7$ sample. The biweight mean β we derive for our lowest luminosity ($M_{\rm UV,AB}\sim-18.5$) subsample is -2.8 ± 0.2. While this is slightly redder than the $\beta=-3.0\pm0.2$ we find from the first-year observations (Bouwens et al. 2010a), this completely independent and unbiased estimate does suggest that the UV-continuum slopes β for lower luminosity galaxies at $z\sim7$ are very blue.

As one final check on the mean β for faint $z\sim7$ galaxies, we considered one variation on the previous test. We divided the J_{125}-band data for each HUDF09 field (HUDF09, HUDF09-1, HUDF09-2) into two disjoint subsets and produced separate J_{125}-band reductions from each. The Y_{105}-band data and first third of the J_{125}-band data were used for the selection of $z\sim7$ sources, and the H_{160}-band data and final two-thirds of the J_{125}-band data were used to measure the UV-continuum slopes β. As in the previous test, this is to ensure that the information used for source selection is completely independent of that used for the β measurements, and therefore the photometric error coupling bias (discussed in Section 4.6 and Appendix B.1.2) must be zero. The biweight mean β we derive for the faintest $z\sim7$ sample ($M_{\rm UV,AB}\sim-18.3$) based on the three HUDF09 fields (HUDF09, HUDF09-1, and HUDF09-2) is -2.7 ± 0.2, again consistent with our other estimates.

This new determination of the mean UV-continuum slope β for very low luminosity $z\sim7$ galaxies is very blue (i.e., $\beta\sim-2.7\pm0.2$). However, this does not appear to be especially anomalous. In fact, it appears to be consistent with what one might expect extrapolating the $z\sim4$–6 UV-continuum slope β relationship to $z\sim7$ (see, e.g., dashed line in the $z\sim7$ panel to Figure 6). The observed correlations of β with both redshift and luminosity are such that one would expect faint $z\sim7$ sources to be very blue. This blue β is also not inconsistent with what one can achieve with standard stellar population modeling (where the UV-continuum slope β can become as steep as ~-2.7; Schaerer 2003; Bouwens et al. 2010a; Robertson et al. 2010). The observed UV-continuum slopes β at $z\sim7$ therefore seem to provide no particularly compelling evidence for exotic stellar populations, i.e., very low metallicity stellar populations or a high escape fraction (see also Finkelstein et al. 2012). Bouwens et al. (2010a) briefly speculated as to what such blue β's might imply, if future observations confirmed that β was really as blue as -3 with small uncertainties.

5. DISCUSSION

5.1. Sequence in SF Galaxies at High Redshift

In the previous section, we presented evidence that the UV-continuum slopes β of star-forming galaxies at high redshift were distributed along a well-defined sequence in UV luminosity. The intrinsic scatter in β along the sequence is small ($\sigma_\beta\sim0.34$), and the dependence of β is such that galaxies become bluer toward lower luminosities. Such a sequence is particularly prominent in our $z\sim4$ sample, but all of our higher

[13] Note that this same issue does not substantially bias the β versus $M_{\rm UV}$ trends we find because we take the UV luminosity to be the geometric mean of the luminosity measurements that contribute to our β measurements (Section 3.4). Flux measurements on either end of the baseline used to derive β bias the β versus $M_{\rm UV}$ trend in opposite directions and should largely cancel.

[14] Despite an apparent difference in the quoted uncertainties on the mean β, the Bouwens et al. (2010a) and Finkelstein et al. (2010) error estimates are actually quite similar, if considered over the same magnitude interval and using similarly sized samples. Finkelstein et al. (2010) consider a sample that is half as small and 0.25 mag fainter—which, not surprisingly, results in a larger quoted uncertainty for β.

[15] We note that this measurement could still be affected (at the level of $\Delta\beta\sim0.1$) by the selection volume bias (Appendix B.1.1) even though the photometric error coupling bias (Appendix B.1.2) will be zero.

redshift selections ($z\sim4$, $z\sim5$, $z\sim6$, $z\sim7$) show strong evidence for such a sequence as well (Figure 6).

The fact that we observe the same dependence of β on UV luminosity in each of four Lyman-break selections suggests the trend we are recovering from the observations is real. Such a color–magnitude relationship was already evident in many studies of galaxies over the redshift range $z\sim2$–5, though the clearest evidence was presented by Bouwens et al. (2009) for $z\sim2.5$ and $z\sim4$ samples and Labbé et al. (2007) for $z\sim1.05$, $z\sim1.8$, and $z\sim2.7$ samples (see Section 4.4). The present work confirms these trends and extends them to $z\sim5$, $z\sim6$, and $z\sim7$.

Consistent with these trends, the UV-continuum slopes β we measure for the most luminous (and presumably most massive) galaxies have similarly red values for β of -1.6 to -1.9 in all four redshift samples examined here (Table 4; similar values were also found by Lee et al. 2011 and Willott et al. 2012) while the lowest luminosity galaxies probed have relatively similar blue values for β of -2.2 to -2.7 for all four samples.

The existence of well-defined sequences for both star-forming and evolved galaxies at lower redshift is now very well established. In the local universe ($z\sim0.1$), for example, Salim et al. (2007) find that galaxies fall along a well-defined sequence in SFR versus stellar mass. Similar star-forming sequences were found by Noeske et al. (2007) and Martin et al. (2007) at somewhat higher redshifts, from $z\sim0.2$ to $z\sim1$ (0.3 dex scatter in the SFRs). find evidence for such a sequence in star-forming galaxies at $z\sim2$, and Elbaz et al. (2011) show that such a sequence exists for even more luminous systems from recent *Herschel* observations. While the present color–magnitude sequence we observe is not an SFR versus stellar mass sequence, the existence of such a sequence suggests that galaxies build up in a relatively well-defined way versus cosmic time.

Theoretically, we would expect such a sequence due to the build up in metals and dust anticipated to occur as galaxies grow in luminosity and mass. One useful illustration of this can be seen in some recent work by Davé et al. (2006) and Finlator et al. (2011) who use smooth particle hydrodynamics to model the evolution of galaxies to $z\sim6$. In Figure 6 of Davé et al. (2006), for example, we see a clear mass dependence in the metallicity of galaxies, with ∼0.3 dex change in metallicity per ∼1 dex change in mass.

Figure 7 of Finlator et al. (2011) shows the expected trends in UV-continuum slopes β as a function of luminosity, including the effects of starlight, dust, and emission lines. Finlator et al. (2011) predict mean UV-continuum slopes of ~-2.02 for luminous ($M_{\rm UV,AB}\sim-20.5$) $z\sim7$ galaxies and ~-2.28 for lower luminosity ($M_{\rm UV,AB}\sim-18.5$) $z\sim7$ galaxies—equivalent to an approximate slope to the β–$M_{\rm UV}$ relationship of just ~-0.13. A fit to the β versus $M_{\rm UV}$ relationship for all the $z\sim4$, $z\sim5$, $z\sim6$, and $z\sim7$ sources in the Finlator et al. (2011) simulations yields $d\beta/dM_{\rm UV}$ slopes of ~-0.10, ~-0.08, ~-0.13, and ~-0.09, respectively (K. Finlator 2011, private communication). The mean slope to this relationship $d\beta/dM_{\rm UV}$ of ~-0.10 is in excellent agreement with what is observed (Figure 7 and Table 4). To better illustrate this, we include a comparison of the UV-continuum slopes β observed with that predicted from the Finlator et al. (2011) simulations (Figure 12).

Rest-frame optical studies of $z\sim4$–6 galaxies with *Spitzer* IRAC have provided evidence for a similar sequence at $z\geqslant4$ for star-forming galaxies (Stark et al. 2009; Labbé et al. 2010b; González et al. 2011). Typical star-forming galaxies at $z\sim5$ have rest-frame UV–optical colors of ∼0.6 mag, with a scatter

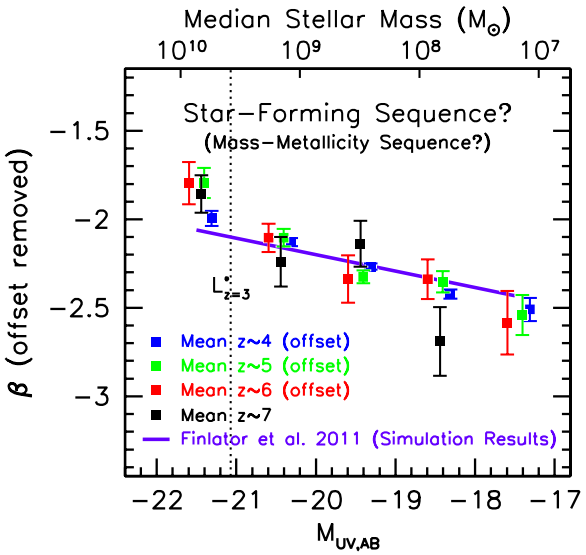

Figure 12. Biweight mean UV-continuum slope β vs. the absolute magnitude in the rest-frame UV. The mean UV-continuum slope results at $z\sim4$ (blue), $z\sim5$ (green), $z\sim6$ (red), and $z\sim7$ (black) from Figure 6 are summarized here and compared with the UV-continuum slopes β expected by the Finlator et al. (2011) cosmological hydrodynamical simulations at $z\sim6$–7 (solid purple line). The top axis gives the median stellar mass González et al. (2011) found for galaxies at a given rest-frame UV luminosity. Outside of the range $-21<M_{\rm UV,AB}<-18.5$, these stellar masses are an extrapolation of the trends found by González et al. (2011). The mean slopes β found at $z\sim4$, $z\sim5$, and $z\sim6$ are offset to bluer values by a uniform $\Delta\beta\sim0.1$–0.3 offset to show how similar the dependence of β on luminosity is at redshifts $z\sim4$, $z\sim5$, and $z\sim6$ where the UV-continuum slopes are the most well defined. The existence of some change (or offset) in β vs. redshift is plausible—as both the age and dust properties of galaxies could easily be a function of cosmic time. The dependence of β on luminosity at $z\sim7$ appears to be stronger, but is consistent with the other redshifts at 1σ. The Finlator et al. (2011) results are shifted $\Delta\beta\sim0.10$ bluer to better illustrate their similarity with the observed trends. Table 5 and Figure 7 provide our best-fit determinations of how the UV-continuum slope β depends on luminosity at $z\sim4$–7. The similar luminosity dependencies strongly argue that the observed luminosity dependence is real and indicative of a sequence in star-forming galaxies at $z\sim4$–7 (Section 5.1).

(A color version of this figure is available in the online journal.)

of 0.5 dex (González et al. 2011, 2012). These UV–optical colors appear to show a slight dependence on luminosity, in the sense that brighter galaxies are redder and fainter galaxies are bluer (González et al. 2012). So far there is no evidence for evolution in the UV–optical colors over the redshift range $4<z<6$ (Stark et al. 2009; Labbé et al. 2010b; González et al. 2011). Both trends in the UV–optical colors parallel those found in the UV-continuum slopes. Together these findings suggest that the evolution of galaxies at high redshift may be self-similar (see also González et al. 2012).

5.2. Sequence in SF Galaxies: Interpreting β versus Luminosity Trends

In the previous section, we briefly discussed the well-defined sequence in β's we observed versus luminosity in our $z\sim4$–7 samples as another instance of a "star-forming" sequence for galaxies. How shall we interpret the changes we observe in the mean UV-continuum slope β of galaxies on this sequence versus their UV luminosity?

Given the approximate correlation of galaxy mass with UV luminosity (e.g., Ouchi et al. 2004b; Lee et al. 2006, 2009; Stark et al. 2009) and gradual build up of galaxies in mass, we would expect the mean properties of galaxies to change gradually as a function of their UV luminosity. While we can

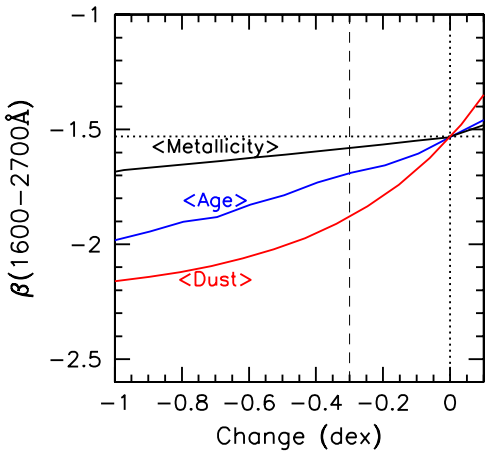

Figure 13. Sensitivity of the UV-continuum slope β (wavelength baseline 1600 Å to 2700 Å) to changes in the mean metallicity, age, or dust extinction of a galaxy population. For our fiducial model (where $\beta \sim -1.5$), we assume $t = 70$ Myr, $\tau = 10$ Myr, $[Z/Z_{\odot}] = -0.7$, $E(B-V) = 0.15$, and a Salpeter IMF (where the star formation history is parameterized as $e^{-t/\tau}$) from the Papovich et al. (2001) fits to $z \sim 2.5$ U-dropouts from the WFPC2 HDF North. In modifying our fiducial model to have younger ages, we make changes to both t and τ. Factor of two (0.3 dex) changes in the mean metallicity, age, or dust content of galaxies result in 0.07, 0.15, 0.35 changes in the UV-continuum slope β. Similar to Figure 7 from Bouwens et al. (2009), but for UV-continuum slopes derived over a wider wavelength baseline. This wavelength baseline is appropriate given our procedure for determining β using flux information over a wide wavelength baseline (Section 3.3; Figure 4; Table 3). It seems clear that changes in the mean dust content of galaxies at high redshift likely have the biggest effect on the UV-continuum slope β and setting up trends with luminosity and possibly redshift (Section 5.2).

(A color version of this figure is available in the online journal.)

imagine many properties of galaxies driving changes in the UV-continuum slope β as a function of UV luminosity, i.e., dust, age, metallicity, AGN content, changes in the dust content of galaxies would likely have the largest effect. Figure 13 provides a simple illustration of this. 0.3 dex changes in the dust content have a much larger effect on the UV-continuum slope β than similarly sized changes in the age, metallicity, or the stellar IMF.

Moreover, given the mass–metallicity relationship observed at $z \sim 0$–4 (e.g., Tremonti et al. 2004; Erb et al. 2006a; Maiolino et al. 2008), we would expect galaxy metallicity—and hence dust content—to show a strong correlation with mass (and luminosity). Higher luminosity galaxies would largely be redder because of their greater dust content while lower luminosity galaxies would be bluer due to a scarcity of dust. Such a correlation of dust content with mass has been explicitly shown (e.g., Figure 18 from Reddy et al. 2010 and Figure 5 from Pannella et al. 2009). We would, of course, also expect changes in the metallicity and age of star-forming galaxies to contribute to the observed trends in β; however, their effect on the UV-continuum slope would likely be much smaller in general (see also Bouwens et al. 2009, Section 4.4); and Labbé et al. 2007).

5.3. Sequence in SF Galaxies: Dust Extinction

Based upon the above tests and discussion, we will assume that dust extinction is the dominant variable in setting up these observed trends. We therefore use our results on the UV-continuum slope β distribution to estimate a mean dust extinction for high-redshift galaxies. We will make use of well-known infrared excess (IRX)–β relationships known to work well at $z \sim 0$ (e.g., Meurer et al. 1999; Burgarella et al. 2005; Overzier et al. 2011) and $z \sim 2$ (e.g., Reddy & Steidel 2004; Reddy et al. 2006b, 2010, 2012a; Daddi et al. 2007). The canonical $z = 0$ IRX–β relationship (Meurer et al. 1999) is

$$A_{1600} = 4.43 + 1.99\beta, \quad (2)$$

where A_{1600} is the dust extinction at 1600 Å. The Meurer et al. (1999) approach is functionally equivalent to correcting for dust extinction based upon the Calzetti et al. (2000) dust curve.

Of course, use of the Meurer et al. (1999) IRX–β relation at $z \geqslant 3$ has not been without controversy, and there has been suggestions that the dust extinction in high-redshift galaxies may be either higher or lower than that implied by the Meurer et al. (1999) relationship. Certainly we might expect some change given that it is likely that AGB stars—thought to be the principal sites for the formation of dust—will not be present in the universe until the universe is at least 1 Gyr old, and therefore the dust that existed in the first 1 Gyr of the universe must have formed in another way, e.g., in the winds of SNe (e.g., Maiolino 2006; Maiolino et al. 2008). The attenuation curve for dust from AGB stars may be very different from dust of other origin (e.g., from SNe).

Dust obscuration would be higher in the high-redshift universe if the attention curve were flatter than Calzetti et al. (2000) while the obscuration would be lower if the attenuation curve were steeper than Calzetti et al. (2000), i.e., much more like that from the Small Magellanic Cloud. A flatter (steeper) attenuation curve implies a higher (lower) dust extinction for a given UV slope. Arguments for its being flatter come from efforts to derive the dust properties of QSOs (Gallerani et al. 2010) while arguments for its being steeper follow from studies of very young galaxies at $z \sim 2$–3. Both Reddy et al. (2006b) and Siana et al. (2008, 2009) find that dust corrections implied by the UV-continuum slopes β of young galaxies are much too large for the Meurer et al. (1999) IRX–β relation to apply. Chary & Pope (2011) argue for low dust extinction in high-redshift galaxies based upon extragalactic background light stacking results. It also been argued that the Carilli et al. (2008) stacking results of the radio emission in $z \sim 3$ galaxies from COSMOS also suggest lower values for the dust extinction, but Reddy et al. (2012a) dispute this, arguing that the Carilli et al. (2008) results are consistent with previous results (which support the Meurer et al. 1999 IRX–β relationship in the mean).

The above arguments aside, there is circumstantial evidence that dust obscuration in high-redshift galaxies is likely at least as large as implied by the Meurer et al. (1999) relationship (see also discussion in Section 6.3). Perhaps the strongest piece of evidence for substantial dust extinction is provided by the large number of high mass ($\sim$1–3$\times 10^{10}$ $M_{\odot}$) galaxies found at $z \sim 5$–6 in the GOODS fields (Eyles et al. 2005; Yan et al. 2005, 2006).[16] Building up these stellar masses by $z \sim 6$ requires SFRs of $\sim$20–30 $M_{\odot}$ yr^{-1}, even assuming constant SFRs for 1 Gyr. Without dust extinction, the progenitors to these massive galaxies would need to be very luminous indeed, i.e., -22 AB mag (Yan et al. 2006). However, such galaxies are not observed at $z \gtrsim 7$ in the requisite numbers (e.g., Bouwens et al. 2011b), arguing that the progenitors must be moderately dust obscured or have existed in a smaller form (i.e., having subsequently merged).

One other possible uncertainty in the dust corrections regards the possible impact of scatter in the IRX–β relationship. Smit

[16] Nonetheless, it is worth noting that early estimates of the stellar masses may have been somewhat too high as a result of the effect of rest-frame optical emission lines on the observed IRAC fluxes not being corrected for.

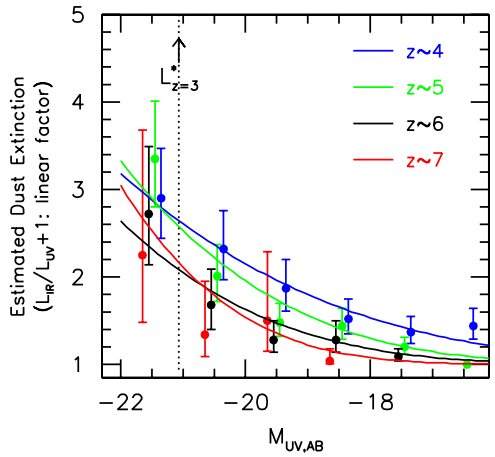

Figure 14. Estimated dust extinction ($L_{\rm IR}/L_{\rm UV}$ + 1) vs. UV luminosity at redshifts $z\sim4$ (blue), $z\sim5$ (green), $z\sim6$ (black), and $z\sim7$ (red; see Section 5.3). The dust extinction is estimated based on the measured UV-continuum slopes (Table 4 and Figure 6) and adopting the Meurer et al. (1999) IRX–β relationship. The solid circles and lines correspond to the results using the biweight mean UV-continuum slopes and linear fits to the biweight means (Figure 6). A slightly lower but similar dust extinction would be derived based on the $z\sim0$ Overzier et al. (2011) Lyman-break analog sample. The uncertainties we estimate for the dust extinction almost exclusively derive from the assumed systematic errors in β, i.e., $\Delta\beta\sim0.10$–0.28. The typical dust extinction inferred for luminous galaxies is much larger than it is for lower luminosity galaxies. The dependence of the dust extinction on redshift is not as large as it is on UV luminosity, but the dust extinction for higher redshift galaxies is lower than it is for lower redshift galaxies at the same luminosity.

(A color version of this figure is available in the online journal.)

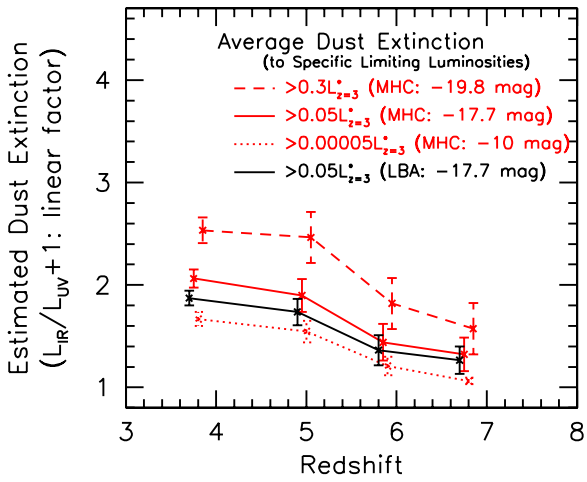

Figure 15. Dust extinction ($L_{\rm IR}/L_{\rm UV}$+1) vs. redshift (Section 5.3). These factors are calculated from the UV-continuum slope β distribution using two different IRX–β relationships: the Meurer et al. (1999) relationship (red lines) and the one derived from Lyman-break analogs (Overzier et al. 2011; black line). The total correction factors for the luminosity density are integrated down to three different limits for the Meurer et al. (1999) IRX–β relationship corresponding to 0.3 $L^*_{z=3}$ (the approximate limiting luminosity for searches over the GOODS fields), 0.05 $L^*_{z=3}$ (the approximate limiting luminosity for searches over the HUDF09 data), and 0.00005 $L^*_{z=3}$ (the approximate lowest luminosity we might expect galaxies to form, e.g., Read et al. 2006; Dijkstra et al. 2004); these are shown with the dashed, solid, and dotted lines, respectively. The corrections are weighted according to luminosity based on the $z\sim4$, $z\sim5$, $z\sim6$, and $z\sim7$ LFs from Bouwens et al. (2007, 2011b). The dust correction factors are also presented in Table 6. This figure is similar to Figure 4 of Overzier et al. (2011) but updated to include our latest results on the UV-continuum slope β distribution at $z\gtrsim4$. Our estimated uncertainties on the dust extinction almost exclusively derive from the assumed systematic errors on β, i.e., $\Delta\beta\sim0.10$–0.28. The correction factors we find show a slight dependence on redshift, but not nearly as strong as what Bouwens et al. (2009) inferred using the ACS+NICMOS observations (Figure 8 of Bouwens et al. 2009).

(A color version of this figure is available in the online journal.)

et al. (2012) found that scatter in this relationship could potentially have a modest effect, i.e., ∼0.09 dex, on the estimated dust extinction, but it depended in detail on cross correlations between dust extinction, β, UV luminosity, and the SFR. Since the effect of scatter in the IRX–β relation on the mean dust extinction is not at all clear (and plausibly consistent with no net change), we will not consider a correction at this time.

Utilizing Equation (2) and the observed distribution of UV-continuum slopes (Table 4), we can estimate the mean extinction corrections ($L_{\rm IR}/L_{\rm UV}$ + 1) as a function of UV luminosity. We have plotted the results in Figure 14 for the four different redshift intervals considered here. As in other work (Bouwens et al. 2009; Reddy & Steidel 2009; Sawicki 2012), we find that the typical dust extinction in galaxies increases systematically as a function of the UV luminosity. Note that in calculating these mean extinction factors we integrate over the full UV-continuum slope distribution. This distribution is approximated as a normal distribution with the biweight means given in Table 4 and 1σ scatter of 0.34 (the median scatter presented in Table 4). We take $A_{1600}=0$ when $A_{1600}<0$ in Equation (2) above.

To determine the actual extinction corrections that are appropriate for real samples, we must weight these extinction corrections according to the UV LFs determined at $z\sim4$, $z\sim5$, $z\sim6$, and $z\sim7$ integrated to specific limiting luminosities. We will make use of the $z\sim4$, $z\sim5$, $z\sim6$, and $z\sim7$ LFs of Bouwens et al. (2007) and Bouwens et al. (2011b). The results are presented in Table 6 and Figure 15. We also include the dust extinction we would derive using an alternate IRX–β relationship $A_{1600}=4.01+1.81\beta$ derived by Overzier et al. (2011). Overzier et al. (2011) derive this relationship based upon a small sample of $z\sim0$ galaxies with similar properties to $z\sim2$–3 LBGs.

Table 6
The Effective Dust Extinction (at ∼1600 Å) Estimated for the LBG Population Integrated Down to Various UV Luminosities

Sample	Effective Extinction		
	$>0.3L^*_{z=3}$ (<-19.8 mag)	$>0.05L^*_{z=3}$ (<-17.7 mag)	$>0.00005L^*_{z=3}$ (<-10 mag)
	Using Meurer et al. (1999) Relationship[a,b]		
$z\sim4$	$2.5^{+0.1+0.4}_{-0.1-0.4}$	$2.1^{+0.1+0.3}_{-0.1-0.3}$	$1.7^{+0.1+0.2}_{-0.1-0.2}$
$z\sim5$	$2.5^{+0.3+0.4}_{-0.2-0.4}$	$1.9^{+0.2+0.3}_{-0.2-0.3}$	$1.5^{+0.1+0.2}_{-0.1-0.2}$
$z\sim6$	$1.8^{+0.2+0.4}_{-0.2-0.3}$	$1.4^{+0.2+0.2}_{-0.2-0.2}$	$1.2^{+0.1+0.1}_{-0.1-0.1}$
$z\sim7$	$1.6^{+0.3+0.6}_{-0.2-0.4}$	$1.3^{+0.2+0.4}_{-0.1-0.3}$	$1.1^{+0.0+0.1}_{-0.0-0.1}$
$z\sim3$	$4.8^{+1.0+1.7}_{-0.8-1.3}$	$3.5^{+0.7+1.3}_{-0.6-0.9}$	$2.4^{+0.4+0.9}_{-0.3-0.6}$

Notes. Section 5.3; see also Figure 15.

[a] The effective dust extinctions given here are the multiplicative factors, i.e., $L_{\rm IR}/L_{\rm UV}$+1, needed to correct the observed UV luminosity densities at ∼1600 Å to their intrinsic values, after integrating to specific limiting luminosities (specified at the top of each column). These extinctions are estimated using Meurer et al. (1999) IRX–β relationship and integrating over the distribution of UV-continuum slopes observed (Table 4). Note that the dust extinctions are much lower when integrated to very low luminosities (see also Reddy & Steidel 2009; Bouwens et al. 2009).

[b] Both random and systematic errors are quoted (presented first and second, respectively).

The extinction corrections given in Table 6 and Figure 15 are an update to the estimates we previously provided in Bouwens et al. (2009) based upon the best UV-continuum slope β estimates available at that time. Relative to the Bouwens et al. (2009) extinction estimates, the most significant change is in the extinction estimates we find at $z \sim 4$ which are now $\sim$1.5–2$\times$ lower (see also Castellano et al. 2012). This is the direct result of the somewhat bluer UV-continuum slopes β we find using the present ACS+WFC3/IR photometry. Such photometry extends over a wider wavelength baseline than is available using ACS alone (as employed by Bouwens et al. 2009) and therefore allows for much more accurate estimates of β.

5.4. Sequence in SF Galaxies: Interpreting β versus Redshift Trends

The above discussion highlights several clear trends that are present in the properties of star-forming galaxies at $z \sim 4$–7 as a function of their UV luminosity and presumably as a function of their stellar mass. The focus of this discussion was the UV-continuum slopes β of galaxies—and by inference—their overall dust extinction.

However, we also noted that the observed β's in the apparent SF sequence showed a modest dependence on the redshift of the sources. At face value, this suggests that the dust extinction in galaxies must increase, from high redshift to low redshift (as per the discussion in Sections 5.2– 5.3). We might expect such an evolution based on the gradual build up of both metals and mass in star-forming galaxies with cosmic time, as seen in the evolution of the mass–metallicity relationship (e.g., Tremonti et al. 2004; Erb et al. 2006a; Maiolino et al. 2008; Mannucci et al. 2009; Laskar et al. 2011), or based on the evolution in the observed correlation between dust extinction and bolometric luminosity from $z \sim 2$ to $z \sim 0$ (e.g., Reddy et al. 2006b, 2010; Buat et al. 2007). Such a change in the mean dust content of galaxies is also supported by the simulations of Finlator et al. (2011) who predict essentially the same evolution in mean β with redshift (Figure 7), and almost all of the change in β ($\gtrsim$75%) comes from a change in the dust content (K. Finlator 2011, private communication).

Of course, it is always possible that the observed evolution in the UV-continuum slopes β might be due to a change in the overall dust composition or extinction curve with cosmic time, as might occur if the dust composition depended on the age of the stellar population in a galaxy. Indeed, we might expect some change in the dust composition of galaxies as a result of the fact that dust from SNe would be expected to form much earlier in the lifetime of a galaxy than dust from AGB stars (e.g., Maiolino et al. 2004; Maiolino 2006; Reddy et al. 2006b; Gallerani et al. 2010; Finkelstein et al. 2012). While it seems clear that such changes may affect the colors of very young star-forming galaxies, it is not clear how important they are in driving the trends we observe with cosmic time. After all, even without considering such changes in dust composition, the detailed cosmological hydrodynamical simulations of Finlator et al. (2011) are successful in reproducing the approximate evolution in β we observe.

5.5. Sequence in SF Galaxies: SFR–Stellar-mass Relationship

In the previous sections, we saw that the overall shape of the SED for star-forming galaxies—both in the UV-continuum slope and the UV–optical colors (González et al. 2012)—exhibits a very similar dependence on luminosity at all redshifts that we examined $z \sim 4$, 5, 6, and 7, suggesting there is a standard star formation sequence for galaxies at high redshift.

In this section, we derive an approximate relationship between the SFR and stellar mass of galaxies that reside on the "star-forming sequence." To do this, we utilize the observed UV luminosities, UV-continuum slopes, and M/L ratios inferred from the observations. We transform the UV luminosities into SFRs by using the canonical Kennicutt (1998) and Madau et al. (1998) UV luminosity-to-SFR conversion factor. A dust correction is made at different UV luminosities using the Meurer et al. (1999) IRX–β relationship and the UV-continuum slope β distribution determined in this paper. As we have seen, these dust corrections are quite significant ($\sim$3$\times$) at higher luminosities around $L^*_{z=3}$, but are essentially zero at lower luminosities ($\lesssim 0.1 L^*_{z=3}$: $\gtrsim -18.5$ AB mag).

Stellar masses can be calculated using the luminosity-dependent M/L ratios derived by González et al. (2011). González et al. (2011) derived these M/L ratios utilizing the *HST* optical + *HST* near-IR + *Spitzer* IRAC photometry for a large sample of $z \sim 4$ galaxies within the CDF-South ERS field (including those sources that are not individually detected in the IRAC observations). González et al. (2011) find that the M/L ratios scale as $(M/L_{\rm UV}) \propto L_{\rm UV}^{0.7}$. González et al. (2011) find a steeper dependence on luminosity than found by Stark et al. (2009), where the M/L ratio scale as $(M/L_{\rm UV}) \propto L_{\rm UV}^{0.175}$. The $z \sim 4$ results should be fairly indicative of the results at higher redshift given the lack of clear evolution in the M/L ratio from $z \sim 7$ to $z \sim 4$ for galaxies at a fixed UV luminosity ($M_{\rm UV} \sim -22$ to -18 mag; Stark et al. 2009; Labbé et al. 2010a, 2010b; González et al. 2011).

The resulting SFRs and stellar masses for galaxies in various UV luminosity bins are shown in the top panel of Figure 16. Fitting a line to these points in log–log space, we find that the SFR varies as $(13^{+7}_{-5}\, M_\odot\, {\rm yr}^{-1})(M_*/10^9\, M_\odot)^{0.73\pm0.32}$. Without any dust correction, we find that the SFR varies as $(6^{+3}_{-2}\, M_\odot\, {\rm yr}^{-1})(M_*/10^9 M_\odot)^{0.59\pm0.32}$. The equivalent results for the specific star formation rate (SSFR) and dust extinction are shown in the lower two panels of Figure 16 (see also Section 5.6).

Interestingly, the SFR versus stellar mass relationship we derive including the effects of dust extinction is much more linear than we would derive without it. Without any dust correction, the results of Stark et al. (2009) and González et al. (2011) imply that SFR $\propto M^{0.85}$ and SFR $\propto M^{0.59}$, respectively. However, correcting for dust extinction, these relationships become a much more linear SFR $\propto M^{1.05}$ and SFR $\propto M^{0.73}$, respectively. An approximately linear proportionality, i.e., SFR vs. M_*, is exactly what is expected from cosmological hydrodynamical simulations (e.g., Davé et al. 2006; Finlator et al. 2011; Dayal & Ferrara 2012). Indeed, it points to a scenario where galaxies build up exponentially with time along a well-defined star-forming sequence (e.g., Stark et al. 2009; Papovich et al. 2011; Lee et al. 2011).

We emphasize that the SFRs and stellar masses shown in Figure 16 (and also quoted for the "star-forming sequence") are representative values for a luminosity-selected sample. They were derived using the median M/L ratios found in specific bins of UV luminosity (González et al. 2011). In general, one would expect different results for the M/L ratios using mass rather than luminosity-selected samples. Different results are also expected using mean rather than median M/L ratios. In particular, a mass selection would yield higher values for the M/L ratios (though the size of the effect will depend substantially on the scatter in the M/L ratios). Also use of mean rather than median M/L

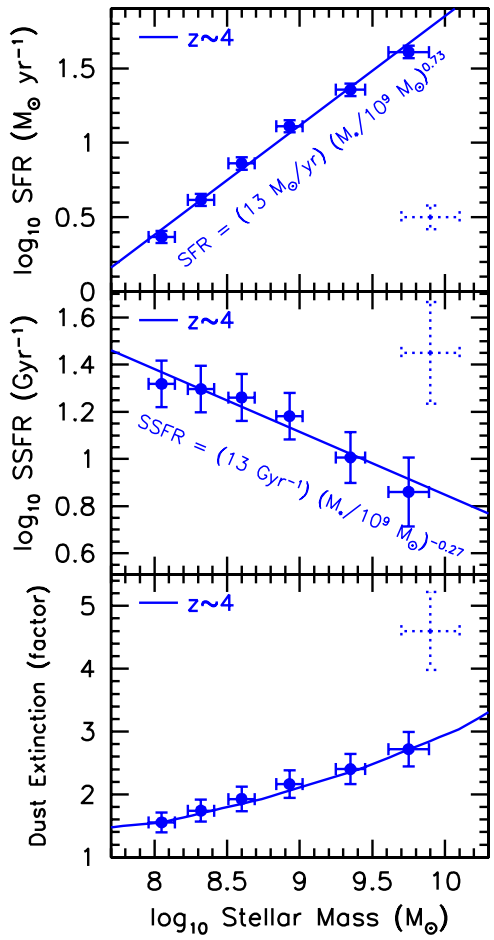

Figure 16. Upper panel: the relationship between the star formation rate and stellar mass of galaxies at $z \sim 4$ (Section 5.5). The points correspond to the mean SFRs and median stellar masses for galaxies with absolute UV magnitudes ranging from -21.0 mag and -18.5 mag, in 0.5 mag intervals. The stellar masses are from González et al. (2011) and the SFRs are derived from UV luminosities adopting the dust corrections tabulated in Table 6. The error bars shown are random errors. The dotted error bar included to the lower right on the plot is representative of the typical systematic error that likely applies to the SFR and stellar mass estimates. The blue line is a linear fit to the points, with SFR $\sim (13^{+7}_{-5}\ M_\odot\ \mathrm{yr}^{-1})(M_*/10^9\ M_\odot)^{0.73\pm0.32}$. The relationship between SFR and stellar mass shown here is expected to be representative for galaxies that are luminosity selected. The stellar masses may be up to a factor of two higher using M/L ratios from a mass-based selection (but the exact correction depends upon uncertain details of the SF histories: see discussion in Section 5.5). Middle panel: the relationship between the specific star formation rate and the stellar mass. The best-fit SFR–stellar-mass relationship from the top panel is presented here in terms of the SSFR (black line: SSFR $\sim (13^{+7}_{-5}\mathrm{Gyr}^{-1})(M_*/10^9\ M_\odot)^{-0.27\pm0.32}$). The error bars are as in the top panel. The SSFRs may be up to a factor of two lower using M/L ratios from a mass-based selection (see discussion in Section 5.5). Lower panel: extinction correction ($L_{\mathrm{IR}}/L_{\mathrm{UV}} + 1$) we apply as a function of stellar mass. The extinction correction is based on the UV-continuum slope β distribution observed and the Meurer et al. (1999) IRX–β relationship. The solid line is derived using the best-fit β and M/L ratio vs. luminosity relationship at $z \sim 4$ (González et al. 2011). The error bars are as in the top panel.

(A color version of this figure is available in the online journal.)

ratios for these calculations would increase the quoted masses. The reason is that medians will not account for the large amounts of mass in the tail of the distribution that extends to high masses. Both effects work in the same sense and would tend to increase the masses of galaxies at each point on the sequence. Overall, by correcting for these effects, we would expect somewhat higher stellar masses for galaxies on the sequence and somewhat lower values of the SSFRs. The precise corrections depend, of course, upon the duty cycle for star formation and scatter in the M/L ratios, but factor of $\sim$2 corrections would not be surprising. Reddy et al. (2012b) include an extended discussion of the effect of source selection on observed SFR vs. stellar mass relations in their Appendix B and Figure 26.

5.6. Sequence in SF Galaxies: Evolution in the SSFR

The results of the previous section allow us to update previous estimates of the SSFR at high redshift to include a correction for the dust extinction. The SSFR, the SFR divided by the stellar mass, has been of considerable interest recently due to the evidence that the SSFR may not evolve very rapidly at high redshift (Stark et al. 2009; González et al. 2010), in significant contrast to that expected from theory (e.g., Bouché et al. 2010; Davé 2010; Dutton et al. 2010; Weinmann et al. 2011; but, see Krumholz & Dekel 2012).

One shortcoming of these early SSFR determinations at high redshift (Stark et al. 2009; González et al. 2010) was that no dust correction was applied (González et al. 2010). Such an approach seemed appropriate at the time, given the very blue UV-continuum slopes β observed for galaxies in the redshift range $z \gtrsim 5$ (Bouwens et al. 2009) and large uncertainties on those UV-continuum slopes (e.g., Bouwens et al. 2009). However, now that sufficiently deep, wide-area near-IR data are available we can establish the UV-continuum slopes β and approximate dust corrections more accurately.

Our new estimates of the dust extinction at $z \sim 4$–7 allow us to correct previous SSFR estimates at $z \sim 4$–7. The results are presented in Figure 17. Typical corrections result in a factor of $\sim$2–3 increase in the SSFR.

We emphasize that the above corrections to the SSFR at $z \gtrsim 4$ are very schematic in nature. A proper determination of the SSFR in this regime requires a fairly extensive, self-consistent analysis of the observations. In addition to the issue of dust extinction, other issues that need to be considered are (1) the selection of the samples by mass in contrast to selection by luminosity and (2) emission-line contamination of our broadband flux measurements (e.g., Schaerer & de Barros 2010).

Already there are many theoretical predictions about how the SSFR should evolve with cosmic time (e.g., Bouché et al. 2010; Weinmann et al. 2011; Krumholz & Dekel 2012). How well do these expectations agree with our corrected SSFRs? The evolution of the SSFR in many models follows the specific accretion rate $\dot{M}/M$, which scales as $(1+z)^{2.5}$ (dotted line in Figure 17; Neistein & Dekel 2008; Weinmann et al. 2011). This implies a factor of $\sim$10 decrease in the SSFR from $z \sim 7$ to $z \sim 2$. By comparison, our revised estimates of the dust extinction at $z \sim 4$–6 imply an SSFR that decreases by a factor of $\sim$3 to $z \sim 2$. While this still does not match the evolution predicted by standard models, the agreement is better. Are there additional ingredients that might lead to further changes? One possibility that has been discussed includes accounting for metallicity dependencies in one's SFR prescription (e.g., Krumholz & Dekel 2012) or changes to the stellar IMF (Davé 2010; Schaye et al. 2010).

5.7. Sequence in SF Galaxies: Small Scatter in the β Distribution

The distribution of UV-continuum slopes β shows a remarkably small intrinsic scatter σ_β for a fixed UV luminosity. The typical scatter σ_β observed is just $\sim$0.34 (Table 4). A similar

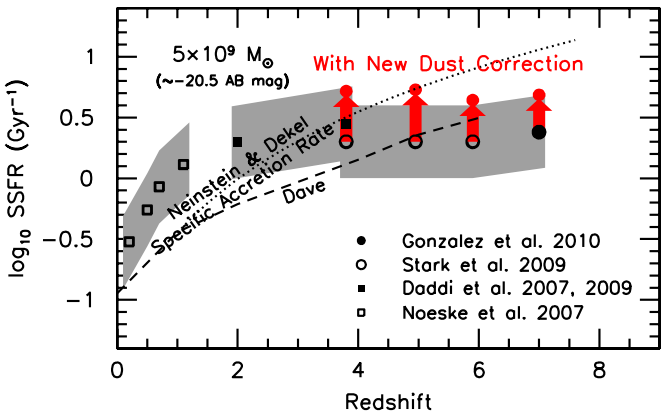

Figure 17. Specific star formation rate (SFR/M_*) for luminous, intermediate mass ($\sim 5 \times 10^9\ M_\odot$) galaxies vs. redshift (solid blue circles; Section 5.6). The star formation rates are estimated using the canonical UV luminosity-to-SFR conversion factors (Madau et al. 1998; Kennicutt 1998) and the extinction factors given in Figure 16. Previous estimates of the specific star formation rate from Noeske et al. (2007; open black squares), from Daddi et al. (2009, 2011; solid black squares), from Stark et al. (2009; open black circles), and González et al. (2010; solid black circle) are also shown. The gray-shaded regions provide an illustration of the rough systemic uncertainties in the SSFRs quoted in the literature. The red arrows show the changes in the SSFRs we would derive including the current estimates of the dust extinction at $z \sim 4$–7. Earlier measurements of the UV-continuum slopes β at $z \sim 5$–7 (Bouwens et al. 2009; Stanway et al. 2005) were sufficiently blue that no dust corrections were previously applied in estimating the SSFRs at high redshift. The SSFRs at $z \sim 4$–7 may be up to a factor of two lower using M/L ratios from a mass-based selection (but the exact correction depends upon uncertain details of the SF histories: see also the discussion in Section 5.5 and Appendix B of Reddy et al. 2012b). The SSFR seems to evolve much more gradually with cosmic time in the observations than in many theoretical models, e.g., Neistein & Dekel (2008; dotted line) and Davé (2008; dashed line), but see however Krumholz & Dekel (2012). The approximate SSFR scaling in typical models scales as the specific accretion rate of gas (proportional to $(1+z)^{2.5}$; Neistein & Dekel 2008).

(A color version of this figure is available in the online journal.)

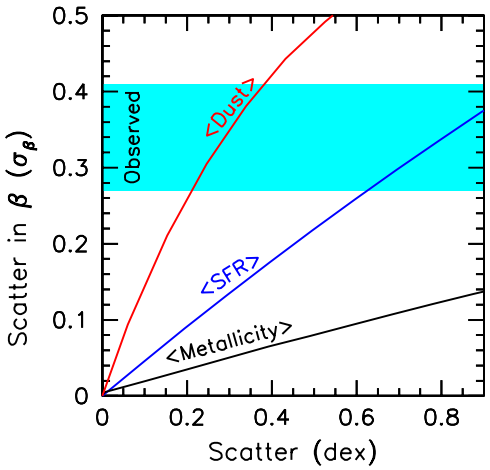

Figure 18. Scatter in the UV-continuum slope β distribution σ_β resulting from scatter in the dust extinction, metallicity, or instantaneous SFRs (see Section 5.7). The typical scatter in the intrinsic β distribution (after subtracting the contribution due to photometric uncertainties) is $\sim$0.34, as indicated by the cyan-shaded region (see Table 4). In estimating the approximate scatter in β that would result from variations in the dust, metallicity, or star formation rate, we adopt a base stellar population model an $E(B-V)$ of $\sim$0.15, a $[Z/Z_\odot]$ of -0.7, a Salpeter IMF, and a constant star formation history. In considering variations in SF history (or instantaneous SFRs of galaxies), we break up the star formation history of each galaxy in ten 50 Myr segments, treat each 50 Myr segment in the SF history as independent, and randomly choose an SFR for each segment from a log-normal distribution. It is evident from this figure that one can approximately match the observed scatter in the UV-continuum slope distribution, by allowing for $\sim$0.3 dex variations in the dust content or $\sim$0.9 dex in the instantaneous SFR. Substantially larger variations in dust content or instantaneous SFRs would introduce a larger scatter in the UV-continuum slope β distribution, which is inconsistent with the observations.

(A color version of this figure is available in the online journal.)

scatter was found by Labbé et al. (2007) and Bouwens et al. (2009) for galaxy samples at $z \sim 1$–2.7 and $z \sim 4$, respectively. Such a small scatter allows us to set upper limits on variations in the star formation histories and dust content of galaxies (assuming that changes in one variable do not offset changes in other variables).

Figure 18 illustrates the impact of scatter in dust, age, or metallicity would have on scatter in the β distribution. For the typical galaxy, we assume an $E(B-V)$ of $\sim$0.15, a metallicity $[Z/Z_\odot]$ of -0.7, a Salpeter IMF, and an approximately constant star formation history with some scatter in the SFR. These parameters are fairly representative for what has been found in stellar population models of luminous $z \sim 2$–4 galaxies (e.g., Papovich et al. 2001; Shapley et al. 2001, 2005; Erb et al. 2006b; Reddy et al. 2006a).

We begin by using the observed scatter in the UV-continuum slope β distribution to set constraints on scatter in the ages (or star formation history) of star-forming galaxies at high redshift. One potentially promising approach is to consider star formation history for galaxies with stochastic variations in the SFR over 50 Myr intervals (a typical timescale over which one might imagine the SFR in a galaxy might be correlated). Assuming similar variations in the SFRs of $z > 4$ galaxies to that observed at $z \sim 0$–1 (where a scatter of $\sim$0.3 dex in observed the SFR–stellar-mass relationship; Noeske et al. 2007) results in just a 0.14 scatter in β. We computed this scatter by (1) running a simulation with 1000 input galaxies, (2) dividing up the star formation history for each galaxy into ten 50 Myr segments, (3) randomly selecting an SFR for each 50 Myr segment from a log-normal distribution with 0.3 dex scatter, (4) computing the resultant β's for each galaxy based on its star formation history, and (5) calculating the scatter in the derived β distribution for the simulated galaxies. For simplicity, each galaxy in the simulation is taken to have an age of 500 Myr.

The predicted scatter in β, i.e., 0.14, is considerably less than we observe. We can, of course, increase the predicted scatter in β by considering star formation histories with larger variations in the SFRs. For example, a 0.9 dex scatter in the SFRs translates into a 0.34 dex scatter in β, which is a good match to intrinsic scatter in β (σ_β). This is similar to the scatter found by González et al. (2011) in modeling the distribution of M/L ratios for $z \sim 4$ star-forming galaxies. In the above modeling, no account is made for changes to the total luminosity of galaxies, as a result of a stochastic star formation history.

Scatter in the dust content can add significantly to the scatter in the UV-continuum slope β, but the magnitude of the scatter will depend directly on how dusty galaxies are in the luminosity range one is considering. If the dust extinction is low, for example, dust has very little impact on the β observed, and therefore small multiplicative changes to the dust extinction factor would have similarly little impact. On the other hand, if the dust extinction is non-negligible, multiplicative changes to the total dust extinction factor would have a big impact on the value of β one observes. For the fiducial luminous galaxy at $z \sim 2.5$, with an $E(B-V) \sim 0.15$ and a Calzetti et al. (2000) dust law, a $\sim$0.3 dex scatter in the dust extinction would result in an observed scatter σ_β of $\sim$0.34 (Figure 18).

Scatter in the metallicity adds very little to scatter in the UV-continuum slopes (Figure 18), and therefore one cannot use the observed scatter in the UV-continuum slope β distribution to set strong limits on scatter in galaxy metallicity.

In summary, the observed scatter in the UV-continuum slopes β distribution allows us to set upper limits on variations in dust content and instantaneous SFR of galaxies (assuming that changes in one variable do not offset changes in other variables). Scatter in the dust extinction of galaxies appear to be $\lesssim$0.3 dex and scatter in the instantaneous SFR is $\lesssim$0.9 dex.

6. STAR FORMATION RATE DENSITY AT HIGH REDSHIFT

The availability of WFC3/IR data over both the ultra-deep HUDF09 fields and wide-area fields has allowed us to establish the UV-continuum slopes to great accuracy over a wide range in redshift and luminosity. In the previous section, we used these UV-continuum slope distributions to estimate the mean dust extinction in star-forming galaxies at high redshift.

Here, we utilize these new estimates of the dust extinction to revisit our determinations of the SFR density at high redshift. In Section 6.1, we begin by first determining the SFR density from those galaxies that make up our high-redshift LBG selections. In Section 6.2, we include the contribution from ultraluminous ($L_{\rm bol} > 10^{12}\ L_\odot$) IR-bright galaxies (Section 6.2). We include this contribution explicitly since dust corrections tend to underestimate the SFRs for the most luminous, IR-bright galaxies (e.g., Reddy & Steidel 2009) and since such galaxies are not typically well represented in rest-frame UV, LBG-type selections. Finally, in Section 6.3, we compare our total SFR density estimates with what we would infer from current measures of the stellar mass density.

6.1. SFR Density at High Redshift

In this subsection, we determine the SFR density using our current estimates of the dust extinction. As in previous work (Bouwens et al. 2009, 2011b), we base our SFR density determinations on our most recent LF determinations at $z \sim 4$–8 (Bouwens et al. 2007, 2011b) and search results at $z \sim 10$ (Bouwens et al. 2011a; Oesch et al. 2012a). Luminosity densities are derived by integrating these LFs down to -17.7 AB mag ($0.05\ L^*_{z=3}$) which is the limit to which we probe the LFs at both $z \sim 7$ and $z \sim 8$. These luminosity densities are then converted into SFR densities using the canonical Madau et al. (1998) and Kennicutt (1998) relation:

$$L_{\rm UV} = \left(\frac{\rm SFR}{M_\odot\ {\rm yr}^{-1}}\right) 8.0 \times 10^{27} {\rm erg\ s^{-1}\ Hz^{-1}}, \quad (3)$$

where a 0.1–125 $M_\odot$ Salpeter IMF and a constant star formation rate of $\gtrsim$100 Myr are assumed. Finally, for our dust extinction estimates, we will use those from Table 6 calculated using the Meurer et al. (1999) IRX–β relationship.

Our latest UV luminosity density and SFR density estimates are summarized in Table 7 and presented in Figure 19. The new estimates are in broad agreement with previous estimates (Bouwens et al. 2009), but we find a lower SFR density at $z \sim 4$, as expected, given the lower dust extinction we infer at these redshifts. The change is significant, with the SFR density decreasing by a factor of $\sim$1.5–2 at this redshift (see also Castellano et al. 2012).

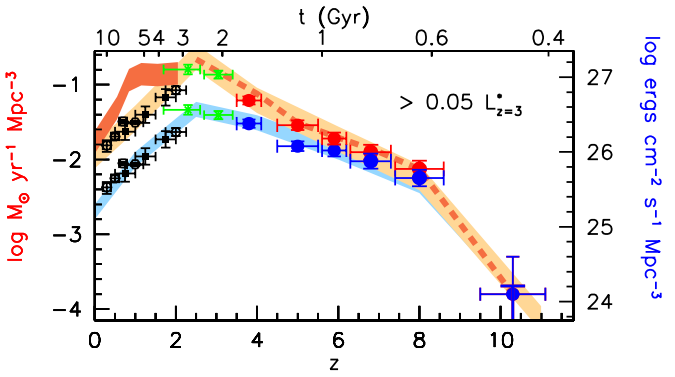

Figure 19. Star formation rate density as a function of redshift (Sections 6.1–6.2; see also Table 7). The lower set of blue points and blue-shaded region gives the UV luminosity density (right axis) and hence the SFR density before correction for dust extinction. The upper set of red points and red-shaded region gives the SFR density (left axis), after applying our estimated dust corrections (see Table 6). The UV luminosity density determinations are integrated down to -17.7 AB mag ($0.05\ L^*_{z=3}$) and taken from Schiminovich et al. (2005; open black squares) at $z \leqslant 1$, Oesch et al. (2010b; solid black squares; see also Hathi et al. 2010) at $z \sim 1$–2.5, Reddy & Steidel (2009; green crosses) at $z \sim 2$–3, Bouwens et al. (2007, 2011b) at $z \geqslant 4$, and Oesch et al. (2012a) at $z \sim 10$. The dark red shaded region and dark dashed line include the contribution from IR bright sources (Magnelli et al. 2009, 2011; Daddi et al. 2009). The contribution from the IR bright population needs to be explicitly included in the SFR density estimates since dust corrections do not typically recover the total SFRs for especially luminous $>10^{12}\ L_\odot$ galaxies (e.g., Reddy et al. 2008). The IR bright population contributes very little to the SFR density at $z \gtrsim 4$ (e.g., Bouwens et al. 2009). Conversion to a Chabrier (2003) IMF would result in a factor of $\sim$1.8 (0.25 dex) decrease in the SFR density estimates given here.

(A color version of this figure is available in the online journal.)

6.2. SFR Density Estimates Including IR Luminous Galaxies

Dusty, infrared-luminous galaxies also potentially contribute quite meaningfully to the SFR density at high redshift. However, it can be quite challenging to account for this contribution on the basis of optical/near-IR surveys with the *Hubble Space Telescope*. Not only can it be difficult to identify such sources in these surveys (due to their faintness in the UV or red colors which cause them to be excluded from LBG selections), but it is now well established that the dust extinction for the most dusty, infrared luminous ($>10^{12}\ L_\odot$) galaxies at $z \sim 1$–3 cannot be accurately estimated using the observed UV-continuum slopes β and IRX–β relationship (e.g., Reddy et al. 2006b; Elbaz et al. 2007).

To accurately account for the SFR density in this population, a better approach is to include that population explicitly by utilizing a LF in the mid-IR/far-IR and integrating down to $10^{12}\ L_\odot$ (e.g., Reddy et al. 2008; Reddy & Steidel 2009; Bouwens et al. 2009). We replicate that approach here integrating published mid-IR LFs to $10^{12}\ L_\odot$, converting the total IR luminosity to SFR using the canonical relation in Kennicutt (1998), and then adding the inferred SFR densities to the dust-corrected UV SFR densities. The IR LFs we utilize are Magnelli et al. (2009, 2011) to $z \sim 2$ and Daddi et al. (2009) at $z \sim 4$. Magnelli et al. (2011) utilize the full set of deep 24 μm and 70 μm observations over the two GOODS fields from the FIDEL program. Since the 70 μm and 24 μm data that Magnelli et al. (2011) utilize are significantly deeper than that used by Caputi et al. (2007) and allow for a self-consistent correction to the total bolometric luminosity, the Magnelli et al. (2011) SFR density estimate represents a noteworthy improvement on the Caputi et al. (2007) estimates we previously utilized at $z \sim 2$ (Bouwens et al. 2009).

Table 7
UV Luminosity Densities and Star Formation Rate Densities to −17.7 AB mag (0.05 $L^*_{z=3}$)[a]

Dropout Sample	$\langle z \rangle$	$\log_{10}\mathcal{L}$ (erg s^{-1} Hz^{-1} Mpc^{-3})	$\log_{10}$ SFR Density ($M_\odot$ Mpc^{-3} yr^{-1}) Uncorrected	Corrected	Incl. ULIRG[b]
B	3.8	26.38 ± 0.05	-1.52 ± 0.05	-1.21 ± 0.05	-1.12 ± 0.05
V	5.0	26.08 ± 0.06	-1.82 ± 0.06	-1.54 ± 0.06	-1.51 ± 0.06
i	5.9	26.02 ± 0.08	-1.88 ± 0.08	-1.72 ± 0.08	-1.71 ± 0.08
z	6.8	25.88 ± 0.10	-2.02 ± 0.10	-1.90 ± 0.10	-1.90 ± 0.10
Y	8.0	25.65 ± 0.11	-2.25 ± 0.11	-2.13 ± 0.11	-2.13 ± 0.11
J[c]	10.3	$24.1^{+0.5}_{-0.7}$	$-3.8^{+0.5}_{-0.7}$	$-3.8^{+0.5}_{-0.7}$	$-3.8^{+0.5}_{-0.7}$
J[c]	10.3	<24.2[d]	<-3.7[d]	<-3.7[d]	<-3.7[d]

Notes. See Sections 6.1–6.2.
[a] Integrated down to 0.05 $L^*_{z=3}$. Based upon LF parameters in Table 2 of Bouwens et al. (2011b; see also Bouwens et al. 2007; see Section 6.1). The SFR density estimates assume $\gtrsim$100 Myr constant SFR and a Salpeter IMF (e.g., Madau et al. 1998). Conversion to a Chabrier (2003) IMF would result in a factor of ∼1.8 (0.25 dex) decrease in the SFR density estimates given here.
[b] See Section 6.2.
[c] $z \sim 10$ determinations and limits are from Oesch et al. (2012a; see also Bouwens et al. 2011a) and assume 0.8 $z \sim 10$ candidates in the first case and no $z \sim 10$ candidates (i.e., an upper limit) in the second case.
[d] Upper limits here are 1σ (68% confidence).

Including the contribution from IR bright galaxies, we present our total SFR density estimates in Table 7 and Figure 19. Interestingly, but not surprising, this correction makes very little difference to the SFR density derived at very high redshifts $z > 4$, but adds modestly to the SFR density at late cosmic times ($z \leqslant 3$). A small contribution of ULIRGs to the SFR density at high redshifts is expected given their position at the very end of the extended buildup process whereby galaxies gradually acquire higher and higher masses in gas, dust, and stars (e.g., Bouwens et al. 2009).

6.3. SFR Densities Implied by Stellar Mass Density Measurements

As in our previous work (Bouwens et al. 2011b), we can compare our SFR density estimates with that implied by recent stellar mass density determinations (e.g., Stark et al. 2009; González et al. 2011; Labbé et al. 2010a, 2010b; González et al. 2011). In doing so, we consider the integrated SFR density and stellar mass density to the same luminosity limits 0.05 $L^*_{z=3}$ for self-consistency.[17]

We use the following formula to infer an approximate SFR density (SFRD) at $z \gtrsim 4$ from the observed stellar mass density (SMD):

$$\mathrm{SFRD}(z_i, z_j) = \frac{\mathrm{SMD}(z_i) - \mathrm{SMD}(z_j)}{\mathrm{time}(z_i) - \mathrm{time}(z_j)} (1-\epsilon)^{-1} f_{\mathrm{LE}}, \quad (4)$$

where $z_i < z_j$ are the redshifts of adjacent Lyman-break samples and ϵ is the gas recycling factor. The $1-\epsilon$ factor accounts for the recycling of gas mass from high-mass stars back into the interstellar medium through SN explosions. Recycling results in only a fraction of the stars formed being locked up in stellar mass, i.e., $dM_*/dt = (1-\epsilon)\mathrm{SFR}$ where $\epsilon = 0.3$ appropriate for a Salpeter IMF (e.g., Bruzual & Charlot 2003). The f_{LE} factor in the above equation accounts for the fact that new galaxies enter our magnitude-limited samples at all redshifts simply as a result of galaxy growth. Since these galaxies (and their stellar mass) would not have been included in the magnitude-limited sample just above them in redshift, these sources would cause us to overestimate the SFR density (see Section 7.4 of Bouwens et al. 2011b). Accounting for this latter effect reduces the inferred SFR density by a factor of 1.3; therefore, we take f_{LE} to be 1/1.3.

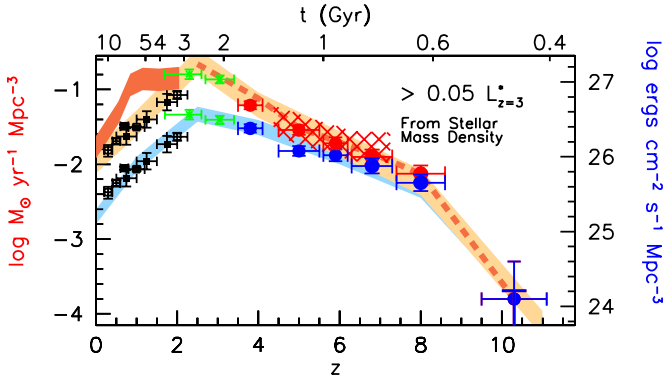

Figure 20. Comparison of the derived SFR density with that implied by stellar mass density determinations in the literature (hatched red region; Labbé et al. 2010b; González et al. 2011; Section 6.3). Published estimates of the stellar mass density at $z \sim 8$ (Labbé et al. 2010b) are very uncertain at present and therefore not used to infer an SFR density at $z > 8$. The SFR density determinations are as in Figure 19 and Table 7. Conversion to a Chabrier (2003) IMF would result in a factor of ∼1.8 (0.25 dex) decrease in the SFR density estimates given here. Good agreement is observed between the SFR density and that implied by the stellar mass density. The agreement is much better than in Bouwens et al. (2011b), as expected given the improvements in the UV-continuum slope β determinations at $z \gtrsim 4$ (and therefore likely dust corrections). Note that we actually require a dust correction to obtain good agreement between the SFR density and that implied by the stellar mass density.
(A color version of this figure is available in the online journal.)

The SFR densities implied by several recent stellar mass density determinations (e.g., Stark et al. 2009; González et al. 2010; Labbé et al. 2010a, 2010b; González et al. 2011) are presented in Figure 20, and there is remarkably good agreement over the redshift range $z \sim 4$–6. This is a useful consistency check and suggests that the dust extinctions we are inferring at $z \sim 4$–7 are reasonable and fit into a consistent picture. The

[17] The importance of using a consistent limit for this comparison was made by Reddy & Steidel (2009) in regards to claims that SFR density determinations at $z \sim 2$–4 might not be consistent with stellar mass determinations in the same redshift range.

general agreement we observe also points toward no clear evolution in the stellar IMF to high redshift ($z \geqslant 4$; see also Bouwens et al. 2011b; Papovich et al. 2011) since any changes in the IMF would have an effect on the SFR density or stellar mass densities we compute from the observed light and likely result in a mismatch.

The observed agreement also suggests that biases in our stellar mass density estimates at high redshift, e.g., due to the contamination of the rest-frame optical light probed by IRAC with strong emission lines (Schaerer & de Barros 2010), are not huge. Of course, we cannot totally rule out modest levels of contamination by emission lines, particularly to the SEDs of $z \sim 6$–7 galaxies, and in fact there may be some evidence in the stacked SEDs of $z \sim 5$–7 galaxies that emission lines do have some effect on the IRAC fluxes (González et al. 2012).

7. SUMMARY

The recent availability of ultra-deep WFC3/IR observations over the HUDF, CDF-South GOODS, and the two HUDF05 fields has allowed us to measure UV-continuum slopes for large samples of star-forming galaxies at $z \sim 4$–7. Such measurements can be made both for samples of $z \sim 4$–7 galaxies to very faint levels (i.e., −17 AB mag) and also for much brighter samples (i.e., −21 AB mag). Use of the Lyman-break selection technique allows us to divide these sources by redshift into four distinct redshift samples ($z \sim 4$, $z \sim 5$, $z \sim 6$, and $z \sim 7$) and thus to quantify the changes in the UV-continuum slope β with cosmic time from ∼0.7 Gyr to 1.8 Gyr after the Big Bang.

This is the first time the UV-continuum slope β distribution can be derived with such small uncertainties for a large sample of $z \sim 4$–7 galaxies (∼2500 galaxies). Full use of the flux information in the UV-continuum is made in determining the UV-continuum slope β for individual sources (Section 3.3), except, of course, those bands contaminated by emission from Lyα or affected by the position of Lyman or Balmer breaks (at ∼1216 Å or ∼3600 Å, respectively). This resulted in >1.5× smaller uncertainties in our measurements of β than obtained using other techniques (see Appendix B.3). It is essential to keep the uncertainties in our β measurements to a minimum if we are to accurately characterize the scatter in the β distribution.

Care was taken to minimize the effect of source selection and photometric scatter on our results (Appendix B). Such effects can significantly bias determinations of the UV-continuum slope distribution (see, e.g., Dunlop et al. 2012), so it is crucial to utilize techniques that minimize the bias. We estimate the bias using extensive Monte Carlo simulations where we added artificial sources to the observations and then select and measure their properties in the same way as the real observations. We demonstrate that we can recover the distribution of UV-continuum slopes β to very faint magnitudes with very small biases ($\lesssim$0.1; see Figures 5 and 24). The very small biases found here appear to be in significant contrast to the large biases found by techniques that use similar information both to select sources and measure their UV-continuum slopes β (see Figures 10 and 26). In particular, as we demonstrate through extensive simulations (Appendix D), a coupling between source selection and β measurement seems to have produced the large biases reported by Dunlop et al. (2012; Section 4.6) toward measuring blue slopes (since sources with blue slopes show a greater likelihood to be at $z \gtrsim 5$). In addition, we find that we can select galaxies with UV-continuum slopes as red as 0.5 (Figures 2 and 21), so the UV-continuum slope distributions we derive should be valid over a wide range in UV-continuum slope β (i.e., −3.5 to 0.5). Small corrections were made based on the selection biases found in our simulations.

Using the above procedure, we accurately establish the distribution of UV-continuum slopes β over a wide range in both redshift and luminosity. This is the first time this has been possible to do so with such precision, and we use these UV-continuum slope β distributions to make inferences about how the dust properties of galaxies likely vary with both luminosity and redshift. We then use these results to derive an SFR versus stellar mass sequence for galaxies at $z \sim 4$, to interpret the evolution of SSFR with cosmic time, and to compare the SFR density results at $z \sim 4$–8 with that inferred from the stellar mass density.

Here are our primary findings.

1. Galaxies at high redshift lie along a well-defined ($\sigma_\beta \sim 0.34$) UV color versus magnitude sequence at all redshifts under study ($z \sim 4$–7). Previously, Labbé et al. (2007) and Bouwens et al. (2009) presented evidence for similar sequences at $z \sim 1$–3 and $z \sim 2.5$–4.
2. The biweight mean UV-continuum slope β shows an approximately linear relationship with UV luminosity in all four redshift intervals we examine, i.e., $z \sim 4$, $z \sim 5$, $z \sim 6$, and $z \sim 7$. The mean β of higher luminosity galaxies is redder than that found for lower luminosity galaxies in all four samples. We demonstrate that this trend is not an artifact of source selection in our analysis, contrary to the suggestion by Dunlop et al. (2012; see Section 4.6 and Appendix B). Similar trends were found by Labbé et al. (2007), Overzier et al. (2008), Bouwens et al. (2009, 2010a), Finkelstein et al. (2010), Lee et al. (2011), and Wilkins et al. (2011; Section 4.4).
3. No statistically significant evolution in the slope of UV-continuum slope β–luminosity sequence is found over the entire redshift range $z \sim 4$–7 (see Figure 7). Particularly striking are the slopes of the β–luminosity relationship at $z \sim 4$, $z \sim 5$, and $z \sim 6$, where the slopes are -0.11 ± 0.01, -0.16 ± 0.03, and -0.15 ± 0.04, respectively. The slope of this relationship at $z \sim 7$, i.e., -0.21 ± 0.07, is consistent with that at lower redshift (later times). The derived slopes to the β–luminosity relationship are in good agreement with previous results at $z \sim 3$–5 (e.g., Bouwens et al. 2009; Overzier et al. 2008; Wilkins et al. 2011).
4. We observe an evolution in the intercept to the UV-slope β versus luminosity relationship with cosmic time, in the sense that higher redshift galaxies of a given UV luminosity are bluer than lower redshift galaxies of the same UV luminosity (see Figure 7). While such an evolution in colors had already been found over the redshift range $z \sim 5$–6 to $z \sim 3$–4 (Lehnert & Bremer 2003; Stanway et al. 2005; Bouwens et al. 2006, 2009, 2010a), this confirms this result at much higher confidence. We remark that this evolution in the colors might have been expected based on the evolution seen in the dust extinction versus bolometric luminosity relationship from $z \sim 2$ to $z \sim 0$ (e.g., Reddy et al. 2006b, 2010; Buat et al. 2007) and also the evolution seen in the mass–metallicity relationship from $z \sim 3.5$ to $z \sim 0$ (e.g., Tremonti et al. 2004; Erb et al. 2006a; Maiolino et al. 2008; Mannucci et al. 2009; Laskar et al. 2011; see Section 5.4).
5. We observe similarly red UV-continuum slopes β, i.e., −1.6 to −1.9, for the most luminous galaxies (and presumably most massive) in all four redshift samples examined here (similar red values were also found by Lee et al.

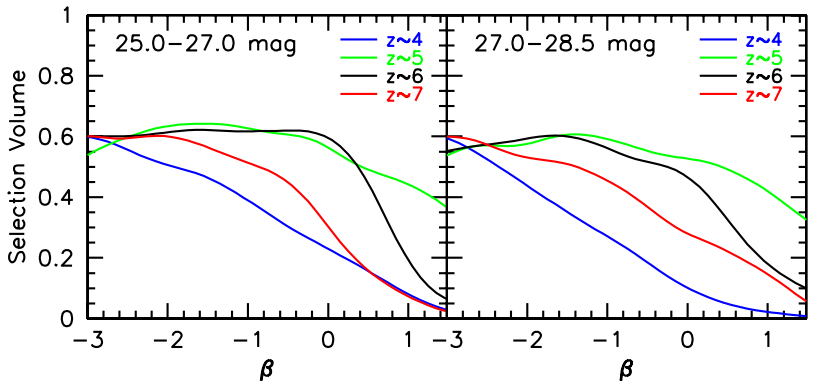

Figure 21. Relative volumes available for selecting $z\sim4$, $z\sim5$, $z\sim6$, and $z\sim7$ galaxies vs. UV-continuum slope β, given our Lyman-break selection criteria (Figure 2). This selection volume is calculated for the HUDF09 fields over the magnitude ranges 25.0–27.0 mag (left panel) and 27.0–28.5 mag (right panel). While our selections are more efficient at selecting galaxies with bluer UV-continuum slopes β, these selections are also effective in identifying galaxies to quite red UV-continuum slopes β.

(A color version of this figure is available in the online journal.)

2011 and Willott et al. 2012). The similarity of the observed β's for the most luminous galaxies (and presumably the most massive) underscores the potential importance of mass in setting the properties of individual galaxies (see also Finkelstein et al. 2012).

6. We find further evidence that the mean UV-continuum slope β of faint $z\sim6$–7 galaxies is very blue, i.e., $\langle\beta\rangle \lesssim -2.5$ (Section 4.8). After correcting for the relevant biases (Appendix B), the biweight mean UV-continuum slope β we measure for ~-18 AB mag sources is -2.5 ± 0.2 and -2.7 ± 0.2 at $z\sim6$ and $z\sim7$, respectively. While very blue overall (relative to the typical galaxy at low redshift), these β's are not inconsistent with what one can achieve with conventional stellar population modeling and therefore do not require exotic stellar populations to explain. Instead, the blue β's appear to be as expected given the observed trends in β versus both redshift and luminosity. Our measured β's confirm earlier results by Bouwens et al. (2010a, 2010b), Oesch et al. (2010c), Bunker et al. (2010), and Finkelstein et al. (2010).
7. We can use the intrinsic scatter in the UV-continuum slope β distribution (Table 4) to set limits on variations in the dust extinction or instantaneous SFR of galaxies on the "star-forming" sequence (Section 5.7). The inferred scatter of $\sigma_\beta \sim 0.34$ in the UV-continuum slope β distribution corresponds to a maximum scatter of 0.3 dex in the dust extinction of galaxies and 0.9 dex in the instantaneous SFRs.
8. We argue that changes in UV-continuum slope β as a function of redshift and luminosity are primarily driven by changes in the mean dust extinction of galaxies (Sections 5.2 and 5.4; see, e.g., Section 4.5 of Bouwens et al. 2009). Using the current determinations of the UV-continuum slope distribution at $z\sim4$–7 and the IRX–β relationship at $z\sim0$ (Meurer et al. 1999; Overzier et al. 2011), we estimate the approximate dust extinction of galaxies as a function of luminosity at $z\sim4$, 5, 6, and 7 (see Figure 14; see Section 5.3). We find that the dust extinction for galaxies at lower luminosities and high redshift is essentially zero (Figure 14 and Section 5.3, e.g., see also Bouwens et al. 2009).
9. We find good agreement between the SFR density inferred from stellar mass density estimates and that inferred from the dust-corrected UV observations over the redshift range $z\sim4$–7 (Figure 20; Section 6.3). The agreement is better than that found using the Bouwens et al. (2011b) estimates of the dust correction.
10. We have used our new estimates of the dust extinction and mass-to-light estimates from the literature (e.g., Stark et al. 2009; González et al. 2011) to reexamine the relationship between the SFR and stellar mass M_* of galaxies (Section 5.5). We find that the SFR is proportional to $M_*^{0.73\pm0.32}$ (Figure 16; see also Labbé et al. 2010a). The exponent to this relationship is much closer to 1.0 including a correction for dust extinction than not including it. This relationship is therefore plausibly close to the simple proportionality, i.e., SFR $\propto M_*$, expected in many cosmological hydrodynamical simulations (e.g., Finlator et al. 2011).
11. Our new estimates of the dust extinction imply higher values of the SSFR at $z\sim4$–7 for the intermediate mass ($\sim5\times10^9\,M_\odot$) galaxies where this dependence was quantified (Section 5.6). The implied change in the SSFRs at $z\gtrsim4$ is approximately a factor of $\sim$2–3 higher than before. With the implied changes to the SSFR, the SSFR at $z\sim5$–7 is therefore plausibly higher than that at $z\lesssim2$ (Figure 17) and hence plausibly evolves from $z\sim4$–7 to $z\sim2$. The observed evolution is therefore in a similar sense to what is expected in many theoretical models (e.g., Bouché et al. 2010; Davé 2010; Dutton et al. 2010; Weinmann et al. 2011; Krumholz & Dekel 2012).

The star-forming (or mass–metallicity) sequence identified here from the well-defined, redshift-independent β versus luminosity relation can provide us with powerful constraints on the buildup and evolution of galaxies at early times. The modest scatter and uniform slope for this sequence suggest a scenario in which galaxies build up and evolve in a uniform manner for most of early cosmic time. Luminous galaxies on this sequence are redder than lower luminosity galaxies, due to their larger dust extinction. Lower redshift galaxies are also redder, at all luminosities again most likely due to their higher dust content.

Given the limited size and S/N of $z\sim7$ samples, the UV-continuum slope distribution at $z\sim7$ is more poorly defined than at $z\leqslant6$ and would benefit from even deeper observations than are currently available. Such observations would be valuable not only for reducing the size of current photometric errors, but also for extending our samples to fainter magnitudes at high S/N.

In addition, we look forward to more WFC3/IR observations over the ∼800 arcmin^2 CANDELS fields (Grogin et al. 2011; Koekemoer et al. 2011). These wide-area observations will allow us to accurately establish the UV-continuum slope distribution to high luminosities where the rarity of sources has made such determinations difficult in the past.

We are happy to thank Romeel Davé, Pratika Dayal, Harry Ferguson, Kristian Finlator, Steve Finkelstein, Mauro Giavalisco, Roderik Overzier, Casey Papovich, Naveen Reddy, Daniel Schaerer, Daniel Stark, and Simone Weinmann for useful discussions. We are greatly appreciative to Kristian Finlator for analyzing the UV-continuum slope distribution in his cosmological hydrodynamical simulations and providing us with the quantitative results. Massimo Stiavelli and Kristian Finlator provided us with helpful feedback on our manuscript. We acknowledge our referee Naveen Reddy for his extensive feedback on our initial submission, which was very useful to us in improving the overall clarity and rigor of this manuscript. We are grateful to all those at NASA, STScI, and throughout the community who have worked so diligently to make Hubble the remarkable observatory that it is today. We acknowledge the support of the NASA grant NAG5-7697, the NASA grant HST-GO-11563, and the ERC grant HIGHZ 227749; P.O. acknowledges support from NASA through a Hubble Fellowship grant 51278.01 awarded by the Space Telescope Science Institute.

APPENDIX A

COMPARISONS WITH UV-CONTINUUM SLOPE MEASUREMENTS BASED ON A SINGLE UV COLOR

In the present study, we determine UV-continuum slopes β from a fit to all available flux observations in the rest-frame UV. Only passbands sufficiently redward of the Lyman break are included to avoid contamination from Lyα emission or IGM absorption (below ∼1216 Å). The goal is to use all available flux information to constrain the UV-continuum slope and to adopt the most extended possible wavelength baseline. This allows us to minimize the errors on our UV-continuum slope measurements.

One potential difficulty with this approach is that the wavelength baseline used to estimate the UV-continuum slope varies somewhat depending on the sample. The wavelength baseline adopted for $z\sim4$ galaxies, for example, is different from the wavelength baseline used for $z\sim6$ galaxies (e.g., see Figure 4) and similarly for galaxies at $z\sim5$ and $z\sim7$ (see also Table 3). Because of these different wavelength baselines, we could potentially measure different UV-continuum slopes for galaxies at different redshifts even if there is no intrinsic evolution in the underlying galaxy populations themselves.

To determine the extent to which our varying wavelength baseline biases our UV-continuum slope measurements, we also estimated UV-continuum slopes β for sources in our samples using the wavelength baseline 1600 Å to 2200 Å. All galaxies in our $z\sim4$–7 samples have coverage at these wavelengths and so the UV-continuum slope measurements can be made in a consistent way across all four samples. Because of the very limited wavelength ranges involved here, we derive the UV-continuum slopes from 2 to 3 rest-frame UV bands. We have derived the following formulae to convert the observed colors to the equivalent UV-continuum slope β. The formulae are as follows:

$$\beta = 2.94(i_{775} - Y_{105}) - 2.00\,(z\sim3.8) \quad \text{(A1)}$$

$$\beta = 2.53(i_{775} - (2Y_{098} + J_{125})/3) - 2.00\,(z\sim3.8) \quad \text{(A2)}$$

$$\beta = 2.93(z_{850} - J_{125}) - 2.00\,(z\sim5) \quad \text{(A3)}$$

$$\beta = 3.09((Y_{105} + J_{125})/2 - H_{160}) - 2.00\,(z\sim6) \quad \text{(A4)}$$

$$\beta = 2.79((Y_{098} + J_{125})/2 - H_{160}) - 2.00\,(z\sim6) \quad \text{(A5)}$$

$$\beta = 4.29(J_{125} - H_{160}) - 2.00\,(z\sim7). \quad \text{(A6)}$$

These formulae are similar to those already presented in Bouwens et al. (2010a), Dunlop et al. (2012), and Wilkins et al. (2011).

To quantify possible systematics, we compared the UV-continuum slopes β derived using our fiducial approach (using the full flux information from the UV continuum) and that estimated from our Lyman-break samples using the above formulae. We found that the median UV-continuum slope β using our fiducial approach is offset by just 0.03, −0.15, 0.06, and 0.0 relative to that determined by Equations (A1)–(A6) for our $z\sim4$, $z\sim5$, $z\sim6$, and $z\sim7$ samples, respectively. These offsets are comparable in size than the $\Delta\beta\sim0.10$–0.28 uncertainties we estimate to be present in the derived UV-continuum slopes β based upon potential systematics in the photometry. We would therefore expect no large biases in our UV-continuum slope measurements as a result of our use of a variable wavelength baseline. Our measurements of the UV-continuum slope β should thus be both reliable and have smaller uncertainties.

APPENDIX B

CORRECTIONS TO THE UV-CONTINUUM SLOPE DISTRIBUTION

Our measurements of the UV-continuum slopes β are, of course, subject to a variety of selection and measurement biases (e.g., Bouwens et al. 2009; Dunlop et al. 2012). These biases include a preferential selection for sources with very blue UV-continuum slopes β and the effect of noise in artificially increasing the scatter in the measured UV-continuum slopes. Since these effects can have a significant effect on the derived β distribution, we cannot draw scientifically useful conclusions unless we determine the magnitude of these biases on the UV-continuum slope β distribution and apply a correction.

In this appendix, we quantify the approximate effect that source selection and photometric error coupling bias have on the UV-continuum slope distribution (Appendix B.1) and then derive a correction for these biases (Appendix B.2). In Appendix B.3, we quantify the effect of photometric errors in increasing the overall scatter in the UV-continuum slope distribution. Finally, in Appendix B.4, we compare the UV-continuum slopes β distribution we derive from ultra-deep and wide-area data sets to ensure that our results show a basic self-consistency. This is important for verifying that all the relevant biases are understood and correctly treated.

B.1. Potential Biases in the Mean β

We would expect small biases in the mean UV-continuum slope β we measure from our observed samples. These biases arise whenever galaxies with specific properties—intrinsic or observed—are easier to select than others. We discuss two such biases: (1) one based on the fact that galaxies with certain intrinsic colors are easier to select than others (Appendix B.1.1) and (2) one arising from the fact that the information used to measure β is not always independent from that used to select the sources (Appendix B.1.2).

The bias described in Appendix B.1.1 arises because not all values for β are selected with the same efficiency, and the bias described in Appendix B.1.2 arises because the average measured value for β does not always equal the intrinsic value.

The purpose of Appendix B.1 is to provide a description of the relevant biases and their approximate size for the most simplistic cases (i.e., if the β distribution is a delta function). In Appendix B.2, we calculate these biases assuming a more realistic input distribution for β.

B.1.1. "Selection Volume Bias": Biases Related to the Intrinsic Selectability of Sources

In general, we would expect our high-redshift selections to be more effective in identifying galaxies with certain UV-continuum slopes than others, resulting in small biases in the mean UV-continuum slope β derived from our samples. Since bluer galaxies are almost always easier to select than redder galaxies in LBG selections, this bias would be toward bluer colors. This effect is often referred to as "template bias" in the literature.

To quantify the extent to which object selection affects the distribution of UV-continuum slopes recovered from the observations, we run extensive Monte Carlo simulations. In these Monte Carlo simulations, we insert artificial galaxies into the real data with a wide variety of luminosities and colors and then reselect these galaxies using the same method as we used on the real sources. We then use these simulations to determine how the selection efficiency and hence selection volume depends upon the intrinsic UV-continuum slope β. A detailed description of these simulations is given in Appendix C.

Figure 21 provides an illustration of the basic results from these simulations in the magnitude ranges 25.0–27.0 mag and 27.0–28.5 mag. Indeed we find the expected trends in the simulations. The selection efficiency is largest for galaxies with the bluest UV-continuum slopes. As in other Lyman-break selections, the selection volumes show a sizeable decrease toward redder UV-continuum slopes, especially for $\beta \gtrsim 0.0$.

The effect of these biases on the mean UV-continuum slope β derived from the observations, however, is relatively modest for typical samples. For example, assuming the intrinsic distribution of UV-continuum slopes β has a mean β of -1.5 and 1σ scatter of 0.3 (see Table 4), the bias in the mean β is just $\Delta\beta \sim 0.1$ for a $\sim$28 mag galaxy in our $z \sim 4$ selection. We estimate the size of this bias by starting with an initial distribution of β's, weighting this distribution by the effective volume at each β (for a given magnitude), and then computing the shift in the biweight mean β.

Figure 22 shows the effect of these selection biases on the mean UV-continuum slope β found in our $z \sim 4$–7 selections. The biases shown in Figure 22 assume that the intrinsic β distribution has a mean value of -2.0 and 1σ scatter of 0.3. While we note a bias toward bluer UV-continuum slopes β, these biases are not extraordinarily large. Similarly small selection biases are found in our other data sets, i.e., the two other HUDF09 fields, the ERS field, and the CDF-South CANDELS field.

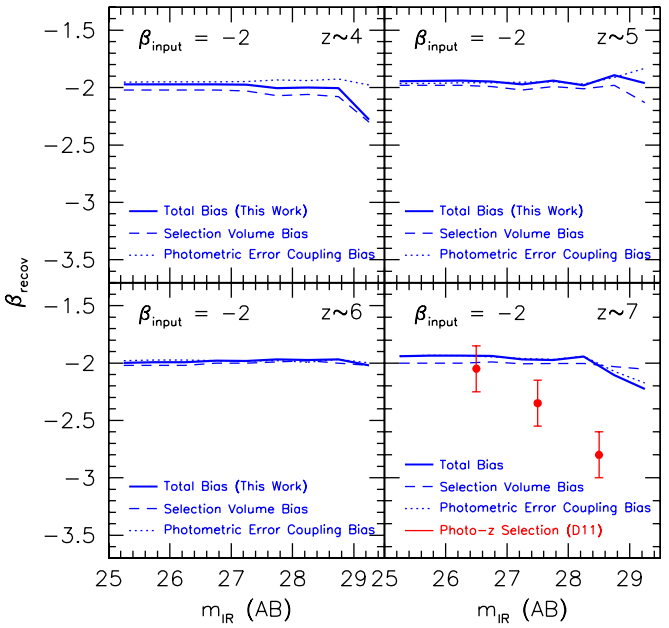

Figure 22. Biases in the mean UV-continuum slope β distribution expected to arise from β-dependent selection effects (dashed lines; Appendix B.1.1) and from any coupling of the photometric errors in the measurement process to source selection (dotted lines; Appendix B.1.2). The panels present the mean UV-continuum slope β we would expect to find from our observed Lyman-break samples given an input UV-continuum slope β distribution with a mean β of -2. The results are presented as a function of the rest-frame UV magnitudes of the sources. The biases expected using the "robust" photometric redshift selection of Dunlop et al. (2012; D11) are also included (red circles; from their Figure 8). It is remarkable how poorly the photometric redshift techniques of Dunlop et al. (2012) perform relative to the present approach. See Figure 10, Section 4.6, and Appendices B.1.2 and D for a brief explanation for the differences between the present approach and that employed by Dunlop et al. (2012). In general, we expect extremely small biases in the mean UV-continuum slopes β derived from our samples, i.e., $\Delta\beta \lesssim 0.1$, relative to the actual values. Of course, at very faint magnitudes, the biases are a little larger, but they are still much smaller than the biases suffered by photometric redshift techniques where source selection and β measurements are tightly coupled.

(A color version of this figure is available in the online journal.)

Comparing the number of sources observed with a given β with the computed selection volumes for this β gives us another means of assessing the importance of this bias. As can be seen in Figure 23 for our HUDF selections, we can select sources to much redder β's than generally observed in our selections. As in our direct estimates of the bias (Figure 22), this suggests that the selection effects are only having a modest effect on our derived β's.

We emphasize that the biases presented in this subsection and the next are simply intended to be illustrative; more realistic estimates of the bias (and those values of the bias we will use to correct the observations) are presented in Appendix B.2.

B.1.2. Photometric Error Coupling Bias

The intrinsic selectability of sources is not the only cause for biases in the mean UV-continuum slope measurements. For many samples, biases can arise as a result of the fact that source selection is done on the basis of the same photometric information as used for the UV-continuum slope β measurements. This can be mildly problematic, since the UV-continuum slope β

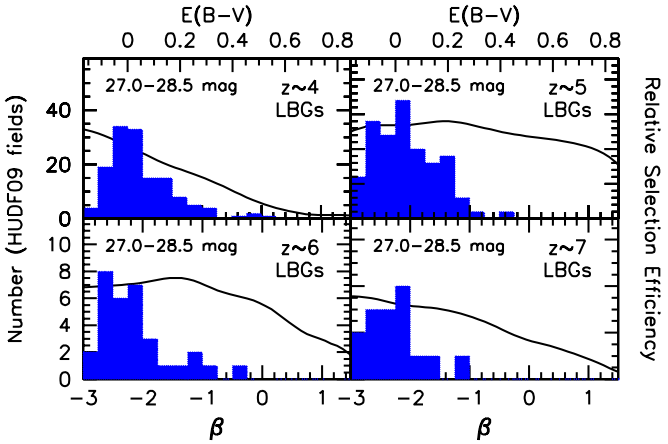

Figure 23. Distribution of UV-continuum slopes β for faint (27.0–28.5 mag) galaxies in the three HUDF09 fields (blue histogram). For comparison, the selection volume available to identify galaxies vs. UV-continuum slope is also included as the black lines (see also Figure 21). The selection volumes presented here are normalized to match the number of galaxies found near the peak of distribution. This figure is similar to Figure 5 of Bouwens et al. (2009). A clear deficit of star-forming galaxies with very red UV-continuum slopes is observed. This figure demonstrates that this deficit is almost certainly real and is not simply the result of selection biases.

(A color version of this figure is available in the online journal.)

measurements are then coupled to the selectability of a source. If errors in the photometry of a source make the source easier to select, any effect these same photometric errors have on the measured β results in biases. Dunlop et al. (2012) show how significant this effect can be using their own photometric redshift selection as a reference (Figure 10).

The size of this effect can be determined using the same simulations as described above. The measured values of β (after selection) are compared with the input values of β. Differences between the mean UV-continuum slope β measured for the selected galaxies and that input into the simulations are the bias. Throughout we will refer to this bias as the "photometric error coupling bias."

In Figure 22, we show the mean UV-continuum slopes β we recover for our $z \sim 4$–7 selections in the HUDF09 field assuming an input UV-continuum slope β of -2. Strikingly, the output distribution of UV-continuum slopes β we find is almost exactly the same as our input distribution, so it is immediately clear that biases resulting from noise are small. Nonetheless, we do note a small bias in the recovered UV-continuum slope distribution toward redder slopes.

The explanation for both of these effects is simple. The bias is small because we use a completely different region of the UV SED (including the two bluest rest-frame UV bands) for selecting galaxies than we use to measure the UV-continuum slope (the second bluest UV band and redder). The effect of photometric scatter on the selection of sources is therefore largely independent of the effects of this scatter on UV-continuum slope β estimates.

The bias toward redder UV-continuum slopes occurs as a result of the small overlap between the bands used for selection and those used for measurement of the UV-continuum slopes. Since this overlapping band is the long wavelength anchor for the selection, any scatter toward fainter values makes the source bluer in the UV continuum and therefore easier to select. However, since this overlapping band is also the short wavelength anchor for UV-continuum slope β estimates, this same scatter toward fainter values results in redder values for the UV-continuum slope β.

B.2. Corrections to the Observed UV*-continuum Slope Distribution*

In Appendix B.1, we estimated the approximate bias in the mean UV-continuum slope β we would determine from the observations. We began by estimating the bias that would result from the fact that galaxies with bluer UV-continuum slopes β are easier to select than galaxies with redder UV-continuum slopes (Appendix B.1.1). We then estimated the bias we would expect in the measured values for β as a result of the slight coupling that occurs between source selection and the measurement process (Appendix B.1.2). Of course, both biases affect the mean UV-continuum slope β, so we need to add the above biases together to obtain the total bias in the UV-continuum slope β. The results are presented in Figure 22 (solid lines).

Remarkably enough, the approximate bias in the mean UV-continuum slope β is almost zero. The bias toward bluer slopes (from the intrinsic selection biases; Appendix B.1.1) largely offsets the bias toward redder slopes (from the slight coupling between source selection and β measurements; Appendix B.1.2), resulting in a very small bias overall. Given the very small size of the biases expected here for our faint samples, it is certainly striking how large these same biases are for the "robust" photometric redshift selection of Dunlop et al. (2012). Figures 10 and 22 provide a rather dramatic illustration of the differences. The contrast in biases is especially noteworthy, especially given the large number of candidates in our faint samples.

While we can calculate the approximate effect of the aforementioned biases on β given some input distribution, for the simulations to be accurate we must use the true underlying β distribution for these inputs. Since we are not able to establish the underlying β distribution without first establishing the biases (so we can apply a correction to the observed distribution of β's), it was necessary to follow an iterative approach. The observed β served as a starting point for the computation of the biases. In each iteration, we used the previous best estimate of the UV-continuum slope β distribution to establish the relevant corrections until we obtained convergence.

Biases in the mean UV-continuum slope were estimated in a very similar way for each of our samples ($z \sim 4$, $z \sim 5$, $z \sim 6$, and $z \sim 7$).

B.3. Biases in the 1σ Scatter Measured for the β Distribution

Flux measurement errors act to significantly broaden the UV-continuum slope β distribution. The added scatter can be substantial, particularly near the selection limits for our samples. Typical uncertainties on individual UV-continuum slope β measurements range from 0.4 to 1.0, with the largest uncertainties being relevant for $z \sim 7$ galaxies where only two passbands (J_{125}, H_{160}) are available to make the measurement and the wavelength baseline is relatively short. An illustration of the extent to which these errors can increase the apparent scatter in the β distribution can be found in Bouwens et al. (2009; Figure 4).

To quantify the extent to which flux measurement error ("noise") increases the spread in the UV-continuum slope β distribution, we again rely on the simulations described in Appendix B.1 (see also Appendix C). For these simulations, we assume that all galaxies have exactly the same UV-continuum

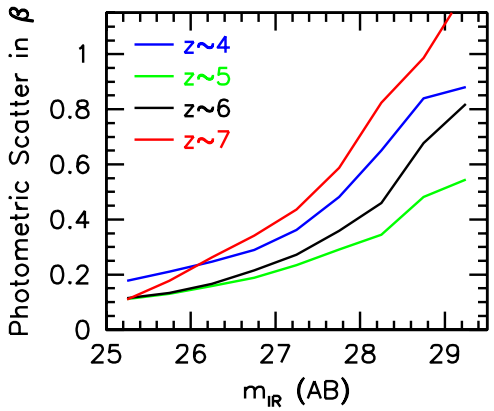

Figure 24. Scatter in the observed UV-continuum slope β distribution expected to originate from photometric errors ("noise"). The plotted results are for UV-continuum slope β determinations over the HUDF. The scatter is determined by adding artificial sources to the observations and then recovering these sources and measuring their UV-continuum slopes. Differences between the input UV-continuum slopes β and that recovered from the observations are used to quantify the approximate scatter in the UV-continuum slope distribution introduced by noise. The scatter we find in β is much lower for lower redshift samples than for our highest redshift sample. We have the longer wavelength baseline and larger number of broadband filters available to establish the UV-continuum slope β at lower redshift. The scatter in our UV-continuum slope β measurements for our $z\sim4$–5 samples is $\sim$1.5$\times$ smaller using the full flux information in the rest-frame UV SED (i.e., $i_{775}z_{850}Y_{105}J_{125}$ for our $z\sim4$ sample and $z_{850}Y_{105}J_{125}H_{160}$ for our $z\sim5$ sample) than using information in a single UV color.

(A color version of this figure is available in the online journal.)

slope β, with no scatter, and then measure the scatter in the recovered distribution. The derived 1σ scatter is shown in Figure 24 for $z\sim4$–7 galaxies identified in the HUDF observations. Scatter is largest for faint sources in each of our $z\sim4$–7 samples and also in our $z\sim6$–7 samples. Scatter in our lower redshift samples is smaller because of the much larger number of passbands and longer wavelength baselines over which we use to measure the UV-continuum slopes β (Table 3 and Section 3.3).

Another benefit of having run these simulations is that they allow us to quantify the extent to which we can reduce the overall uncertainties in β using the full flux information in the UV continuum, rather than using just a single color (Section 3.3 and Appendix A). These gains are most dramatic for $z\sim4$ and $z\sim5$ galaxies in our fields where we use the information in four passbands (Table 3) rather than just two (Appendix A). In the $z\sim4$ or $z\sim5$ cases, for example, we find a factor of $\sim$1.5 reduction in the scatter.

B.4. Comparisons between the HUDF09 and ERS+CANDELS Determinations

In the previous sections, we outlined the procedure we use to determine the distribution of UV-continuum slopes β for high-redshift galaxy samples, after correcting for various selection and measurement biases.

An important check on these results is to compare the distributions we derive at different depths. How well does the distribution of UV-continuum slopes β obtained from the ultra-deep HUDF09 data set agree with that obtained from the wide-area ERS+CANDELS observations? The results are shown in Figure 25 for all four of our Lyman-break selections. While the agreement is excellent overall, this should perhaps not come as a great surprise given the very small corrections that need to be made to each of our selections (Figure 22).

APPENDIX C

SIMULATION PROCEDURE USED TO ASSESS BIASES

The UV-continuum slope β distributions we find are sensitive to a wide variety of object selection and measurement issues. To determine the approximate size of these effects, we ran an extensive set of Monte Carlo simulations where we inserted artificial galaxies into the real data, reselected them, and measured their properties, all in the same way as done for our real samples (Section 3). Galaxies are randomly included in the simulated images over the full redshift window where we might conceivably select them, i.e., $z\sim2.9$–5.0 for our $z\sim4$ samples, $z\sim4.0$–6.0 for our $z\sim5$ samples, $z\sim5.0$–7.0 for our $z\sim6$ samples, and $z\sim6.0$–8.0 for our $z\sim7$ samples. For these simulations, we start with real pixel-by-pixel images of similar luminosity galaxies from the $z\sim4$ HUDF sample of Bouwens et al. (2007). The $z\sim4$ HUDF sample of Bouwens et al. (2007) implicitly defines the size and morphology distribution used in our simulations for $z\sim4$ galaxies, both in terms of the absolute sizes, the size–luminosity relation, and also the width of the size distribution. Sizes of the sources are scaled as $(1+z)^{-1}$ to match the observed size-redshift trends (e.g., Bouwens et al. 2004; Ferguson et al. 2004; Buitrago et al. 2008). Such a size scaling results in a close reproduction of the actual size distribution of galaxies in the $z\sim7$–8 observations (Oesch et al. 2010a; Appendix A of Bouwens et al. 2011b). We have utilized such techniques extensively in the last decade to establish the reliability of our selections, to quantify biases in measured magnitudes and colors, and to establish the needed corrections (e.g., Bouwens et al. 2003, 2004, 2006, 2007, 2008, 2009, 2011b).

APPENDIX D

BIASES IN MEASURING β USING A PHOTOMETRIC REDSHIFT PROCEDURE?

While we offer one approach to establishing the UV-continuum slope β distribution, a complementary approach was put forward by Dunlop et al. (2012). In this approach, high-redshift sources are selected using a photometric redshift procedure and their UV-continuum slopes β are estimated directly from their observed colors. Using this methodology, Dunlop et al. (2012) found no dependence of β on luminosity or redshift, which is in contrast to the present results and most results in the literature (Sections 4.3–4.4).

One of the most interesting claims Dunlop et al. (2012) made using their approach was that measurements of the UV-continuum slope β at faint magnitudes were likely unreliable, and hence it was not possible to determine the mean UV-continuum slope β to very faint magnitudes. Dunlop et al. (2012) demonstrated these significant biases by inserting high-redshift sources into their catalogs with specific UV-continuum slopes β, adding noise to the photometry, and then deriving the mean UV-continuum slope β for the selected sources. Dunlop et al. (2012) found that galaxies at fainter magnitude levels, particularly $>$28 mag, were biased to much bluer UV-continuum slopes β than the sources they put into their simulations. These biases resulted from the effect of noise in perturbing the colors of sources in their catalogs and these same colors being used for both source selection and β measurements. This is the same photometric error coupling bias we discussed in Appendix B.1.2.

Are such biases really as unavoidable as Dunlop et al. (2012) suggest? To investigate this, we wrote software to approximately

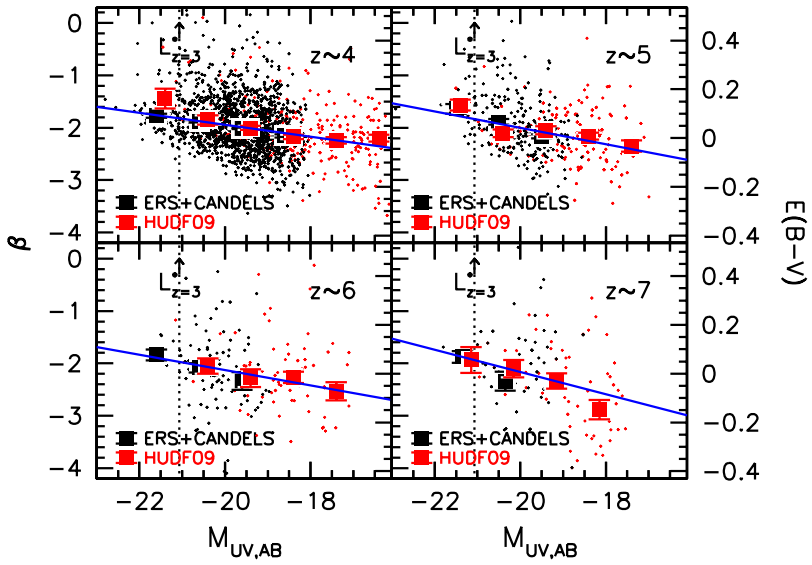

Figure 25. UV-continuum slope β vs. UV luminosity for our $z\sim4$, $z\sim5$, $z\sim6$, and $z\sim7$ samples. The red points are sources from our HUDF09 samples and the black points are from our ERS+CANDELS samples. The large solid squares show the biweight mean UV-continuum slope measured in 1.0 mag intervals. The error bars give the 1σ uncertainties on the biweight mean. The red and black squares are horizontally offset for clarity (to avoid direct overlap with each other). The blue lines show the best-fit relationship between UV-continuum slope β and luminosity presented (Section 3.6). Excellent agreement is observed between the mean β determinations in our ultra-deep HUDF09 and those in our wide-area ERS+CANDELS selections in the luminosity range where the determinations overlap. This suggests that the β distribution we derive from our shallower data sets is fair and any possible residual biases (not accounted for in our calculated corrections; Appendices B.1–B.3) are small.

(A color version of this figure is available in the online journal.)

replicate the procedure by Dunlop et al. (2012). We then ran Monte Carlo simulations involving more than 6×10^4 sources. Each source was assigned a random H_{160}-band magnitude between 25 AB mag and 30 AB mag, keeping the intrinsic β fixed for all sources in a simulation run. Fluxes for individual sources were computed based on the input β's assuming power-law SEDs. Noise was added to the fluxes of sources in the simulations assuming HUDF09-depth data. Finally, sources were selected using a similar photometric redshift procedure to that employed in Dunlop et al. (2012) and McLure et al. (2011). This involved comparing the measured fluxes for each source with the fluxes from various template SEDs to determine the minimum χ^2 at each redshift and then calculating the redshift likelihood function $P(z)$.

For SED templates, we used the four templates from Coleman et al. (1980) and the two bluest starburst templates from Kinney et al. (1996), linearly interpolating between adjacent templates. While this provides us with slightly less freedom in fitting arbitrary SEDs than is available to Dunlop et al. (2012), who utilizing the Bruzual & Charlot (2003) spectral synthesis code consider a wide range of ages, metallicities, and dust extinctions, the SED template set we consider covers a sufficient range to illustrate the relevant biases in β. No prior was assumed. Sources were selected if (1) the primary redshift solution is preferred at >95% confidence over the secondary redshift solution (i.e., χ^2 (best-fit, high-z) $<$ χ^2 (best-fit, low-z) + 4, (2) >50% of the integrated redshift likelihood $\int P(z)$ is at $z > 6$, and (3) the best-fit χ^2 is statistically acceptable (typically $\chi^2 < 10$ given the number of flux constraints and free parameters in the SED modeling). Following Dunlop et al. (2012), we estimate the UV-continuum slope β for sources in the simulations from the observed $J_{125}-H_{160}$ colors, using the expression $\beta = 4.43(J_{125}-H_{160})-2.00$.

The results of our simulations are shown in Figure 26 for initial β values of -2.0 and -2.5. Not surprisingly, we obtain similar results with our simulations (red line) as what Dunlop et al. (2012) obtained (solid red circles). The simulations indicate a strong bias in the recovered UV-continuum slopes (β) at faint magnitudes toward bluer slopes. This is particularly true at >28 mag where the recovered β is $\delta\beta \simeq 0.8$ bluer than the intrinsic value. As we show below, these biases depend critically on the passbands used to select sources. This bias likely originates from a close coupling of the information used to select sources and that used to measure β (Appendix B.1.2). This coupling is problematic because any effect that noise has in making the apparent UV slopes bluer would also cause objects to be more amenable to selection via the Dunlop et al. (2012) procedure.

Is it possible for us to recover the UV-continuum slope β in a less biased fashion? The answer is yes, but it requires that we use independent information to select the sources from what we use to measure the UV-continuum slopes thereby decoupling the effect of noise on the two processes. We can do this by repeating the above photometric redshift selection, but only using the flux information in the five passbands that do not contribute to our UV-continuum slope estimates, i.e., the B_{435}, V_{606}, i_{775}, z_{850}, and Y_{105} bands. We also consider a selection using the five passbands that do not contribute plus the bluest remaining band, i.e., the B_{435}, V_{606}, i_{775}, z_{850}, Y_{105}, and J_{125} bands. The results are shown in Figure 26, and it is clear that the mean UV-continuum slope β we measure is less biased, especially in the five passband case. Indeed, the mean UV-continuum slope β can be successfully recovered to ~29 AB mag, even in the six-passband case. This provides a clear demonstration that it is possible to measure the mean UV-continuum slope β to very faint flux levels, given the appropriate technique.

We minimize the biases by excluding those passbands used for the β measurements from the selection process (i.e., excluding the reddest one or two passbands from the photometric redshift determinations). Are there any disadvantages to this

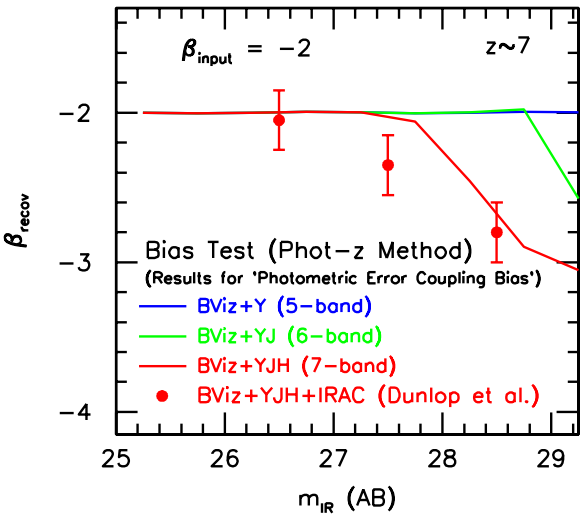

Figure 26. Mean UV-continuum slope β we recover vs. IR magnitude at $z\sim7$ using a photometric redshift selection procedure and input UV-continuum slopes β of -2 (see Appendix D). The procedure we use to select galaxies and measure their UV-continuum slopes β here is designed to be similar to that used by Dunlop et al. (2012). Shown are the results selecting sources using the five-band $BVizY$ photometry (blue), six-band $BVizYJ$ photometry (green), and the full seven-band $BVizYJH$ photometry (red). Our results for the full seven-band photometry seem very similar to that obtained by Dunlop et al. (2012; solid red circles). The mean UV-continuum slope β we recover using five- or six-band photometry is much less biased than what we recover using the full seven-band photometry. The reason a seven-band selection results in biased measures of the UV-continuum slope β is that similar information (i.e., the J- and H-band fluxes) is used (1) to measure their UV-continuum slopes β and (2) to select the sources. Because of this coupling, the seven-band photometric redshift selection excludes as unreliable precisely those sources which are reddest in their observed UV slopes, thus biasing the slope results. This is the same as the "photometric error coupling bias" discussed in Appendix B.1.2, and it becomes very large at low S/N. Significantly less biased measures of the mean UV-continuum slope β can be obtained using five- or six-band photometric redshift selections (due to the independence of the information being used for source selection and the measurement of β). These simulations effectively show that UV-continuum slopes β can be recovered accurately to very faint flux levels, given the appropriate technique.

(A color version of this figure is available in the online journal.)

approach? While one might argue that this results in some loss of ability to control for contamination, such losses are small, as one can see from the following considerations: (1) the only secure characteristic we know about high-redshift star-forming galaxies is that they disappear at wavelengths bluer than $\sim$1216 Å and are detected blueward of that in the rest-frame UV. Use of five- or six-band photometry to compute photometric redshifts allows us to verify that sources have this characteristic. (2) Selection of high-redshift sources can be improved by excluding those sources with the reddest colors redward of the break. Only one color is necessary for this task. For a $z\sim7$ selection, this means a six-band $BVizYJ$ photometric redshift selection (the same bands are used for our $z\sim7$ Lyman-break selection). Adding a seventh band to the photometric redshift selection might appear to help, but actually does not, as this results in significantly biased UV slope β measurements (see Figure 26). (3) Even if a small number of contaminants make it into one's samples one can mitigate the effect they have on the mean UV-continuum slope β through the use of robust statistics like the biweight mean (see Section 3.5). Thus, there appears to be few disadvantages to using an approach that minimizes the biases. The gains in measurement reliability greatly offset any potential concerns.

Table 8
A Complete List of the UV-continuum Slopes β We Measure for Sources in Our $z\sim4$, $z\sim5$, $z\sim6$, and $z\sim7$ Samples from the HUDF09+ERS+CANDELS Data Sets

R.A.	Decl.	$M_{UV,AB}$	β	$\langle z\rangle$	Data Set[a]
03:32:38.49	−27:48:21.41	−17.82	-1.92 ± 0.24	4	1
03:32:38.42	−27:48:18.68	−16.46	-1.61 ± 0.57	4	1
03:32:37.67	−27:48:16.87	−17.49	-2.19 ± 0.37	4	1
03:32:37.31	−27:48:13.74	−18.41	-2.42 ± 0.19	4	1
03:32:38.14	−27:48:12.75	−17.82	-1.35 ± 0.34	4	1

Notes.
[a] The data set from which the source was selected and in which its UV-continuum slope beta derived (1 = HUDF09, 2 = HUDF09-1, 3 = HUDF09-2, 4 = CANDELS/ERS).

(This table is available in its entirety in a machine-readable form in the online journal. A portion is shown here for guidance regarding its form and content.)

APPENDIX E

UV-CONTINUUM SLOPE β MEASUREMENTS FOR INDIVIDUAL SOURCES

In the interests of transparency and to facilitate comparisons with other high-redshift studies, we include a complete list of the UV-continuum slopes β that we derive for all 2518 individual sources in our $z\sim4$, $z\sim5$, $z\sim6$, and $z\sim7$ samples in Table 8.

We note that a small fraction ($\lesssim$1%) of the sources in our samples have very red UV-continuum slopes β, i.e., $>$0.5, and therefore may not be at high redshifts (since this would imply that the apparent break at $\sim$1 micron in their SEDs may not be due to absorption by neutral hydrogen, but due to their overall spectral shape). We should emphasize, however, that these sources have essentially no effect, i.e., $d\beta\lesssim0.01$, on the biweight-mean β's we report.

REFERENCES

Adelberger, K. L., & Steidel, C. C. 2000, ApJ, 544, 218
Anderson, J., & Bedin, L. R. 2010, PASP, 122, 1035
Beckwith, S. V. W., Stiavelli, M., Koekemoer, A. M., et al. 2006, AJ, 132, 1729
Beers, T. C., Flynn, K., & Gebhardt, K. 1990, AJ, 100, 32
Bertin, E., & Arnouts, S. 1996, A&AS, 117, 39
Blakeslee, J. P., Anderson, K. R., Meurer, G. R., Benítez, N., & Magee, D. 2003, in ASP Conf. Ser. 295, Astronomical Data Analysis Software and Systems XII, ed. H. E. Payne, R. I. Jedrzejewski, & R. N. Hook (San Francisco, CA: ASP), 257
Bouché, N., Dekel, A., Genzel, R., et al. 2010, ApJ, 718, 1001
Bouwens, R., Broadhurst, T., & Illingworth, G. 2003, ApJ, 593, 640
Bouwens, R. J., Illingworth, G. D., Blakeslee, J. P., Broadhurst, T. J., & Franx, M. 2004, ApJ, 611, L1
Bouwens, R.J., Illingworth, G.D., Blakeslee, J.P., & Franx, M. 2006, ApJ, 653, 53
Bouwens, R. J., Illingworth, G. D., Franx, M., & Ford, H. 2007, ApJ, 670, 928
Bouwens, R. J., Illingworth, G. D., Franx, M., & Ford, H. 2008, ApJ, 686, 230
Bouwens, R. J., Illingworth, G. D., Franx, M., et al. 2009, ApJ, 705, 936
Bouwens, R. J., Illingworth, G. D., Labbe, I., et al. 2011a, Nature, 469, 504
Bouwens, R. J., Illingworth, G. D., Oesch, P. A., et al. 2010a, ApJ, 708, L69
Bouwens, R. J., Illingworth, G. D., Oesch, P. A., et al. 2010b, ApJ, 709, L133
Bouwens, R. J., Illingworth, G. D., Oesch, P. A., et al. 2011b, ApJ, 737, 90
Bruzual, G., & Charlot, S. 2003, MNRAS, 344, 1000
Buat, V., Marcillac, D., Burgarella, D., et al. 2007, A&A, 469, 19
Buitrago, F., Trujillo, I., Conselice, C. J., et al. 2008, ApJ, 687, L61
Bunker, A. J., Stanway, E. R., Ellis, R. S., McMahon, R. G., & McCarthy, P. J. 2003, MNRAS, 342, L47
Bunker, A. J., Wilkins, S., Ellis, R. S., et al. 2010, MNRAS, 409, 855
Burgarella, D., Buat, V., & Iglesias-Páramo, J. 2005, MNRAS, 360, 1413
Calzetti, D., Armus, L., Bohlin, R. C., et al. 2000, ApJ, 533, 682
Caputi, K. I., Lagache, G., Yan, L., et al. 2007, ApJ, 660, 97
Carilli, C. L., Lee, N., Capak, P., et al. 2008, ApJ, 689, 883

Castellano, M., Fontana, A., Grazian, A., et al. 2012, A&A, 540, A39
Chabrier, G. 2003, PASP, 115, 763
Chary, R.-R., & Pope, A. 2011, ApJ, submitted (arXiv:1003.1731)
Coleman, G. D., Wu, C.-C., & Weedman, D. W. 1980, ApJS, 43, 393
Daddi, E., Dannerbauer, H., Stern, D., et al. 2009, ApJ, 694, 1517
Daddi, E., Dickinson, M., Morrison, G., et al. 2007, ApJ, 670, 156
Davé, R. 2008, MNRAS, 385, 147
Davé, R. 2010, arXiv:1008.5283
Davé, R., Finlator, K., & Oppenheimer, B. D. 2006, MNRAS, 370, 273
Dayal, P., & Ferrara, A. 2012, MNRAS, 421, 2568
Dijkstra, M., Haiman, Z., Rees, M. J., & Weinberg, D. H. 2004, ApJ, 601, 666
Dow-Hygelund, C. C., Holden, B. P., Bouwens, R. J., et al. 2007, ApJ, 660, 47
Dunlop, J. S., McLure, R. J., Robertson, B. E., et al. 2012, MNRAS, 420, 901
Dutton, A. A., van den Bosch, F. C., & Dekel, A. 2010, MNRAS, 405, 1690
Elbaz, D., Daddi, E., Le Borgne, D., et al. 2007, A&A, 468, 33
Elbaz, D., Dickinson, M., Hwang, H. S., et al. 2011, A&A, 533, A119
Erb, D. K., Shapley, A. E., Pettini, M., et al. 2006a, ApJ, 644, 813
Erb, D. K., Steidel, C. C., Shapley, A. E., et al. 2006b, ApJ, 646, 107
Eyles, L. P., Bunker, A. J., Stanway, E. R., et al. 2005, MNRAS, 364, 443
Ferguson, H. C., Dickinson, M., Giavalisco, M., et al. 2004, ApJ, 600, L107
Finkelstein, S. L., Papovich, C., Giavalisco, M., et al. 2010, ApJ, 719, 1250
Finkelstein, S. L., Papovich, C., Salmon, B., et al. 2012, ApJ, submitted (arXiv:1110.3785)
Finlator, K., Oppenheimer, B. D., & Davé, R. 2011, MNRAS, 410, 1703
Gallerani, S., Maiolino, R., Juarez, Y., et al. 2010, A&A, 523, A85
Giavalisco, M., Ferguson, H. C., Koekemoer, A. M., et al. 2004, ApJ, 600, L93
González, V., Bouwens, R., Labbé, I., et al. 2012, ApJ, submitted (arXiv:1110.6441)
González, V., Labbé, I., Bouwens, R. J., et al. 2010, ApJ, 713, 115
González, V., Labbé, I., Bouwens, R. J., et al. 2011, ApJ, 735, L34
Grogin, N. A., Kocevski, D. D., Faber, S. M., et al. 2011, ApJS, 197, 35
Hathi, N. P., Malhotra, S., & Rhoads, J. E. 2008, ApJ, 673, 686
Hathi, N. P., Ryan, R. E., Jr., Cohen, S. H., et al. 2010, ApJ, 720, 1708
Kennicutt, R. C., Jr. 1998, ARA&A, 36, 189
Kinney, A. L., Calzetti, D., Bohlin, R. C., et al. 1996, ApJ, 467, 38
Koekemoer, A. M., Faber, S. M., Ferguson, H. C., et al. 2011, ApJS, 197, 36
Kron, R. G. 1980, ApJS, 43, 305
Krumholz, M. R., & Dekel, A. 2012, ApJ, 753, 16
Labbé, I., Franx, M., Rudnick, G., et al. 2007, ApJ, 665, 944
Labbé, I., Gonzlez, V., Bouwens, R. J., et al. 2010a, ApJ, 708, L26
Labbé, I., Gonzlez, V., Bouwens, R. J., et al. 2010b, ApJ, 716, L103
Laskar, T., Berger, E., & Chary, R.-R. 2011, ApJ, 739, 1
Lee, K.-S., Dey, A., Reddy, N., et al. 2011, ApJ, 733, 99
Lee, K.-S., Ferguson, H. C., Wiklind, T., et al. 2012, ApJ, 752, 66
Lee, K.-S., Giavalisco, M., Conroy, C., et al. 2009, ApJ, 695, 368
Lee, K.-S., Giavalisco, M., Gnedin, O. Y., et al. 2006, ApJ, 642, 63
Lehnert, M. D., & Bremer, M. 2003, ApJ, 593, 630
Madau, P., Pozzetti, L., & Dickinson, M. 1998, ApJ, 498, 106
Magnelli, B., Elbaz, D., Chary, R. R., et al. 2009, A&A, 496, 57
Magnelli, B., Elbaz, D., Chary, R. R., et al. 2011, A&A, 528, A35
Maiolino, R. 2006, in Proc. of the 26th Meeting of the IAU, The Universe at $z > 6$, ed. D. Schaere, A. Ferrara, & K. A. van der Hucnt (Cambridge: Cambridge Univ. Press), 7
Maiolino, R., Nagao, T., Grazian, A., et al. 2008, A&A, 488, 463
Maiolino, R., Schneider, R., Oliva, E., et al. 2004, Nature, 431, 533
Mannucci, F., Cresci, G., Maiolino, R., et al. 2009, MNRAS, 398, 1915
Martin, D. C., Small, T., Schiminovich, D., et al. 2007, ApJS, 173, 415
McLure, R. J., Dunlop, J. S., Cirasuolo, M., et al. 2010, MNRAS, 403, 960
McLure, R. J., Dunlop, J. S., de Ravel, L., et al. 2011, MNRAS, 418, 2074
Meurer, G. R., Heckman, T. M., & Calzetti, D. 1999, ApJ, 521, 64
Neistein, E., & Dekel, A. 2008, MNRAS, 383, 615
Noeske, K. G., Weiner, B. J., Faber, S. M., et al. 2007, ApJ, 660, L43
Oesch, P. A., Bouwens, R. J., Carollo, C. M., et al. 2010a, ApJ, 709, L21
Oesch, P. A., Bouwens, R. J., Carollo, C. M., et al. 2010b, ApJ, 725, L150
Oesch, P. A., Bouwens, R. J., Illingworth, G. D., et al. 2010c, ApJ, 709, L16
Oesch, P. A., Bouwens, R. J., Illingworth, G. D., et al. 2012a, ApJ, 745, 110
Oesch, P. A., Bouwens, R. J., Illingworth, G. D., et al. 2012b, ApJ, in press (arXiv:1201.0755)
Oesch, P. A., Stiavelli, M., Carollo, C. M., et al. 2007, ApJ, 671, 1212
Oke, J. B., & Gunn, J. E. 1983, ApJ, 266, 713
Ouchi, M., Shimasaku, K., Okamura, S., et al. 2004a, ApJ, 611, 660
Ouchi, M., Shimasaku, K., Okamura, S., et al. 2004b, ApJ, 611, 685
Overzier, R. A., Bouwens, R. J., Cross, N. J. G., et al. 2008, ApJ, 673, 143
Overzier, R. A., Heckman, T. M., Wang, J., et al. 2011, ApJ, 726, L7
Pannella, M., Carilli, C. L., Daddi, E., et al. 2009, ApJ, 698, L116
Papovich, C., Dickinson, M., & Ferguson, H. C. 2001, ApJ, 559, 620
Papovich, C., Dickinson, M., Ferguson, H. C., et al. 2004, ApJ, 600, L111
Papovich, C., Finkelstein, S. L., Ferguson, H. C., Lotz, J. M., & Giavalisco, M. 2011, MNRAS, 412, 1123
Popesso, P., Dickinson, M., Nonino, M., et al. 2009, A&A, 494, 443
Read, J. I., Pontzen, A. P., & Viel, M. 2006, MNRAS, 371, 885
Reddy, N., Dickinson, M., Elbaz, D., et al. 2012a, ApJ, 744, 154
Reddy, N. A., Erb, D. K., Pettini, M., Steidel, C. C., & Shapley, A. E. 2010, ApJ, 712, 1070
Reddy, N. A., Pettini, M., Steidel, C. C., et al. 2012b, ApJ, in press (arXiv:1205.0555)
Reddy, N. A., & Steidel, C. C. 2004, ApJ, 603, L13
Reddy, N. A., & Steidel, C. C. 2009, ApJ, 692, 778
Reddy, N. A., Steidel, C. C., Erb, D. K., Shapley, A. E., & Pettini, M. 2006a, ApJ, 653, 1004
Reddy, N. A., Steidel, C. C., Fadda, D., et al. 2006b, ApJ, 644, 792
Reddy, N. A., Steidel, C. C., Pettini, M., et al. 2008, ApJS, 175, 48
Riess, A. G., Strolger, L.-G., Casertano, S., et al. 2007, ApJ, 659, 98
Robertson, B. E., Ellis, R. S., Dunlop, J. S., McLure, R. J., & Stark, D. P. 2010, Nature, 468, 49
Salim, S., Rich, R. M., Charlot, S., et al. 2007, ApJS, 173, 267
Salpeter, E. E. 1955, ApJ, 121, 161
Sawicki, M. 2012, MNRAS, 421, 2187
Schaerer, D. 2003, A&A, 397, 527
Schaerer, D., & de Barros, S. 2010, A&A, 515, A73
Schaye, J., Dalla Vecchia, C., Booth, C. M., et al. 2010, MNRAS, 402, 1536
Schiminovich, D., Ilbert, O., Arnouts, S., et al. 2005, ApJ, 619, L47
Schlegel, D. J., Finkbeiner, D. P., & Davis, M. 1998, ApJ, 500, 525
Shapley, A. E., Steidel, C. C., Adelberger, K. L., et al. 2001, ApJ, 562, 95
Shapley, A. E., Steidel, C. C., Erb, D. K., et al. 2005, ApJ, 626, 698
Siana, B., Smail, I., Swinbank, A. M., et al. 2009, ApJ, 698, 1273
Siana, B., Teplitz, H. I., Chary, R.-R., Colbert, J., & Frayer, D. T. 2008, ApJ, 689, 59
Smit, R., Bouwens, R. J., Franx, M., et al. 2012, ApJ, in press (arXiv:1204.3626)
Stanway, E. R., McMahon, R. G., & Bunker, A. J. 2005, MNRAS, 359, 1184
Stark, D. P., Ellis, R. S., Bunker, A., et al. 2009, ApJ, 697, 1493
Stark, D. P., Ellis, R. S., Chiu, K., Ouchi, M., & Bunker, A. 2010, MNRAS, 408, 1628
Stecher, T. P. 1965, ApJ, 142, 1683
Steidel, C. C., Adelberger, K. L., Giavalisco, M., Dickinson, M., & Pettini, M. 1999, ApJ, 519, 1
Steidel, C. C., Adelberger, K. L., Shapley, A. E., et al. 2003, ApJ, 592, 728
Steidel, C. C., Giavalisco, M., Pettini, M., Dickinson, M., & Adelberger, K. L. 1996, ApJ, 462, L17
Szalay, A. S., Connolly, A. J., & Szokoly, G. P. 1999, AJ, 117, 68
Taniguchi, Y., Shioya, Y., & Trump, J. R. 2010, ApJ, 724, 1480
Tremonti, C. A., Heckman, T. M., Kauffmann, G., et al. 2004, ApJ, 613, 898
Vanzella, E., Giavalisco, M., Dickinson, M., et al. 2009, ApJ, 695, 1163
Weinmann, S. M., Neistein, E., & Dekel, A. 2011, MNRAS, 417, 2737
Wilkins, S. M., Bunker, A. J., Stanway, E., Lorenzoni, S., & Caruana, J. 2011, MNRAS, 417, 717
Willott, C. J., McLure, R. J., Hibon, P., et al. 2012, AJ, submitted (arXiv:1202.5330)
Windhorst, R. A., Cohen, S. H., Hathi, N. P., et al. 2011, ApJS, 193, 27
Yan, H., Dickinson, M., Giavalisco, M., et al. 2006, ApJ, 651, 24
Yan, H., Dickinson, M., Stern, D., et al. 2005, ApJ, 634, 109
Yan, H.-J., Windhorst, R. A., Hathi, N. P., et al. 2010, Res. Astron. Astrophys., 10, 867